Metamaterials for Computational Imaging

by

John D. Hunt

Department of Electrical & Computer Engineering
Duke University

Date: _____

Approved:

_____
David R. Smith, Supervisor

_____
David Brady

_____
Matt Reynolds

_____
Nan Jokerst

_____
Nathan Kundtz

_____
Henry Everitt

Dissertation submitted in partial fulfillment of the requirements for the degree of
Doctor of Philosophy in the Department of Electrical & Computer Engineering
in the Graduate School of Duke University
2013

Abstract

Metamaterials for Computational Imaging

by

John D. Hunt

Department of Electrical & Computer Engineering
Duke University

Date: _____

Approved:

_____
David R. Smith, Supervisor

_____
David Brady

_____
Matt Reynolds

_____
Nan Jokerst

_____
Nathan Kundtz

_____
Henry Everitt

An abstract of a dissertation submitted in partial fulfillment of the requirements for the degree of Doctor of Philosophy in the Department of Electrical & Computer Engineering
in the Graduate School of Duke University
2013

Copyright © 2013 by John D. Hunt
All rights reserved except the rights granted by the
Creative Commons Attribution-Noncommercial Licence

Abstract

Metamaterials extend the design space, flexibility, and control of optical material systems and so yield fundamentally new computational imaging systems. A computational imaging system relies heavily on the design of measurement modes. Metamaterials provide a great deal of control over the generation of the measurement modes of an aperture. On the other side of the coin, computational imaging uses the data that that can be measured by an imaging system, which may limited, in an optimal way thereby producing the best possible image within the physical constraints of a system. The synergy of these two technologies - metamaterials and computational imaging - allows for entirely novel imaging systems.

These contributions are realized in the concept of a frequency-diverse metamaterial imaging system that will be presented in this thesis. This 'metaimager' uses the same electromagnetic flexibility that metamaterials have shown in many other contexts to construct an imaging aperture suitable for single-pixel operation that can measure arbitrary measurement modes, constrained only by the size of the aperture and resonant elements. It has no lenses, no moving parts, a small form-factor, and is low-cost.

In this thesis we present an overview of work done by the author in the area of metamaterial imaging systems. We first discuss novel transformation-optical lenses enabled by metamaterials which demonstrate the electromagnetic flexibility of metamaterials. We then introduce the theory of computational and compressed imaging

using the language of fourier optics, and derive the forward model needed to apply computational imaging to the metaimager system. We describe the details of the metamaterials used to construct the metaimager and their application to metamaterial antennas. The experimental tools needed to characterize the metaimager, including far-field and near-field antenna characterization, are described. We then describe the design, operation, and characterization of a one-dimensional metaimager capable of collecting two-dimensional images, and then a two-dimensional metaimager capable of collecting two-dimensional images. The imaging results for the one-dimensional metaimager are presented including two-dimensional (azimuth and range) images of point scatters, and video-rate imaging. The imaging results for the two-dimensional metaimager are presented including analysis of the system's resolution, signal-to-noise sensitivity, acquisition rate, human targets, and integration of optical and structured-light sensors. Finally, we discuss explorations into methods of tuning metamaterial radiators which could be employed to significantly increase the capabilities of such a metaimaging system, and describe several systems that have been designed for the integration of tuning into metamaterial imaging systems.

Contents

Abstract **iv**

List of Tables **ix**

List of Figures **x**

Acknowledgements **xiii**

1 Introduction **1**

2 Metamaterial Lenses **10**

2.1 Gradient index metamaterial lens with holey-dielectrics 11

2.2 Transformation-optical lenses 15

2.3 Microwave transformation-optical Luneburg lens 18

2.4 Infrared transformation-optical Luneburg lens 24

2.5 Microwave transformation-optical Maxwell Lens 30

2.6 Microwave transformation-optical Rotman lens 37

2.7 Negative index of refraction lens: the superlens 47

2.8 Conclusions 48

3 Theory of Metamaterial Imaging Apertures **49**

3.1 Computational imaging 50

3.1.1 Discretization of the imaging equation 51

3.1.2 Image reconstruction 56

3.1.3 Compressed sensing 59

3.2 Measurement mode design 64
3.2.1 Principal component mode design 65
3.2.2 Linear discriminant mode design 67
3.3 Metamaterial imaging forward model 71
3.4 Fourier optics overview 75
3.5 Conclusions 81
4 Complementary Metamaterials and Metamaterial Antennas 82
4.1 Complementary metamaterials 84
4.2 Metamaterial antenna radiation 95
4.3 Conclusions 101
5 Experimental Tools 103
5.1 Far-field antenna characterization 103
5.2 Near-field antenna characterization 105
5.3 Conclusions 109
6 Frequency-Diverse Metamaterial Imager 110
6.1 One-dimensional aperture 112
6.2 Two-dimensional aperture 117
6.2.1 Aperture design 118
6.2.2 Forward model characterization 121
6.2.3 Resolution 124
6.2.4 Scene measurement and estimation 124
6.2.5 Scene constraint using structured-light sensors 126
6.2.6 Imaging performance 130
6.3 Conclusions 132

7 Tuning Metamaterial Apertures **134**

7.1 Schottky junction tuning 136

7.2 MOSFET tuning 140

7.3 Conclusions 144

8 Conclusion **146**

8.1 Areas for future research 147

A A method of generating distributions of uniformly sized holes for GRIN metamaterials **150**

Bibliography **155**

Biography **165**

List of Tables

2.1 Transformation-optical Rotman lens performance 46

7.1 Drude model parameters for a MOSFET channel under different gate biases 143

List of Figures

1.1 Comparison of conventional and computational imaging schemes . . . 7

2.1 Permittivity map for a 2D TE gradient-index lens 12

2.2 metamaterial gradient index lens 13

2.3 Comparison of simulated and experimental gradient-index metamaterial lens performance 14

2.4 Design of a transformation-optical flattened Luneburg lens 19

2.5 Comparison of simulated and experimental transformation-optical RF Luneburg lens performance 22

2.6 Raytraces through IR Luneburg index distributions 25

2.7 Effective index dispersion of IR slab waveguide 26

2.8 Fabricated IR TO Luneburg lens 28

2.9 Experimental characterization of IR TO Luneburg 29

2.10 Ray trace through a perfect metamaterial relay lens 31

2.11 The permittivity distribution of the transformed Maxwell lens 32

2.12 The two types of metamaterial unit cells used to implement the Maxwell relay lens 33

2.13 Fabricated Maxwell relay lens 34

2.14 Comparison of simulated and experimental transformation-optical relay lens 36

2.15 Design of a transformation-optical Rotman lens 42

2.16 The complementary metamaterial unitcell used to implement a transformation-optical Rotman lens 43

2.17 A fabricated metamaterial transformation-optical Rotman lens 44
2.18 Experimental performance of a metamaterial transformation-optical Rotman lens 45
3.1 Schematic representation of a general imaging system 50
3.2 Geometrical representation of scene measurement. 54
3.3 Single pixel imaging with a focal-plane mask 56
3.4 Geometrical representation of compressed imaging. 60
3.5 Compressed sensing example 63
3.6 Mode design with PCA 65
3.7 PCA example 67
3.8 Mode design with LDA 69
3.9 Holographic generation of LDA modes 70
4.1 The basic types of metamaterials 83
4.2 Radiation of a cELC 84
4.3 Radiation of a cELC versus geometry 85
4.4 Complementary metamaterial simulation boundary conditions 86
4.5 Complementary metamaterial simulation boundary conditions 87
4.6 Complementary metamaterial retrieved constitutive parameters . . . 88
4.7 Radiative loss versus slot depth of a complementary metamaterial . . 89
4.8 Resonant frequency versus slot depth of a complementary metamaterial 90
4.9 Resonance quality-factor versus slot depth of a complementary metamaterial 91
4.10 Complementary metamaterial oscillator strength versus transmission line thickness 93
4.11 Optimized cELC design 94
4.12 Complementary metamaterial leakywave radiation 96
4.13 Leakywave antenna radiation 98

5.1 Far-field antenna characterization setup 105
5.2 Near-field antenna characterization setup 106
6.1 The fabricated 1D metaimager 112
6.2 Farfields radiated by a 1D metamaterial antenna 114
6.3 Radiation pattern versus frequency for a random 1D metamaterial antenna 115
6.4 Reconstructions of four different static scenes imaged with a 1D metamaterial antenna 116
6.5 Reconstructions of four different static scenes imaged with a 1D metamaterial antenna 117
6.6 A 2D metamaterial aperture 118
6.7 2D metamaterial aperture schematic 119
6.8 2D metamaterial aperture configuration 120
6.9 2D metamaterial aperture signal analysis 122
6.10 Near-field and radiation from a 2D metamaterial aperture 123
6.11 2D metaimager far-fields 123
6.12 2D metamaterial aperture configuration 125
6.13 Structured-light constrained 3D images of a person 127
6.14 RF 3D images of people 129
6.15 A 3D images versus SNR 131
6.16 Mean Squared Error of reconstructed RF image 132
7.1 Design of a Schottky-diode-tuned cELC device 137
7.2 Simulation of a Schottky-diode-tuned cELC device 139
7.3 Design of a MOSFET-tuned cELC device 142
7.4 Simulation of a MOSFET-tuned cELC device 143
7.5 MOSFET channel resistivity 144

Acknowledgements

I'd like to thank the Air Force Office of Scientific Research and the Department of Homeland Security (Grant No. FA9550-09-1-0539) who supported parts of this work. I'd also like to thank the Army Research Office who sponsored a Multidisciplinary University Research Initiative (Contract No. W911NF-09-1-0539) which also supported parts of this work.

1

Introduction

Since the earliest cameras, imaging systems have been an integral part of human life. Today imaging systems are used in virtually every field, from art and entertainment to industry and military, from medicine and science to safety and security. The earliest cameras aimed to directly reproduce an image of the world onto a detector, such as a wall or a piece of film. This is because in early imaging systems, it was necessary that the measurements made could be directly viewed as the final image. Thus it has been generally desired that the image produced by a camera be as representative of the scene in the real word as possible. Camera systems have been designed for centuries to minimize abberations, producing images with a direct one-to-one relationship to the scene being imaged, and this is still how many people view the process of imaging.

With the advent of modern digital computers in the 1940s and '50s, new imaging systems began appearing that removed the requirement that the measurements made by an imaging system look just like the scene being imaged. Instead, the measurements made by these new imaging systems are fed into computers which process them to produce images. This opened up a huge number of previously impossible imaging

applications. Some of the first of these computation-based imaging systems were developed in the early 1970s for medical imaging. These include computational tomography (CT) systems[1] and magnetic resonance imaging (MRI) systems[2]. Such imaging systems rely heavily on methods of solving large numbers of linear equations and it no coincidence that both CT and MRI imaging systems were developed only a few years after an efficient iterative solution called Algebraic Reconstruction Technique (ART) was (re)discovered in 1970 [3, 4].

The development of radar imaging techniques followed a similar path from direct to computational image production. The first radar systems, developed in the 1920s and '30s directed a beam of light in a single direction and measured the time it took an echoed signal to return.[5, 6] These measurements of direction and range were plotted directly on a display to produce an image. Then in 1951 the theory of synthetic aperture radar (SAR) imaging was developed [7]. In SAR imaging, the measured signal return from a transceiver placed at many locations in space is processed by a computer (the first systems used optical processing techniques) to produce an high-resolution three-dimensional image. This technology has been advanced to the point that it is now possible to use SAR imaging systems to do fast, safe, low-power millimeter-wave imaging for security applications [8], something anyone who has been through an airport in recent years has experienced. These mechanically-scanned SAR imaging systems effectively replace metal detectors, but with the additional functionalities that they can detect non-metallic materials and form an image so that objects can be readily identified and localized.

All of these different imaging techniques are united by the common requirement that the measurements made by the imaging system must be processed to produce a estimate, or *image*, of the scene being imaged. The scene that is being imaged is a spatially distributed object that scatters or emits light. If the physics of how the measured signal relates to the scene is understood, then an image can be recovered.

The field of *computational imaging* provides a general mathematical framework that describes this imaging process. In the terminology of computational imaging, the physics of how each measurement relates to the scene is called the *forward model*. Each measurement made by the imaging system measures only a portion of the scene. The portion of the scene that is interrogated by each measurement is one *measurement mode* of the imaging system. Each measurement is then the amplitude of the corresponding measurement mode that exists in the scene. The imaging process is to measure the amount of each measurement mode that is present in the scene using the imaging apparatus, and from these measurements, and knowledge of the forward model of the system, produce an image of the scene.

It is possible that no combination of the measurement modes that can be measured by the system can exactly represent the scene, (in fact this is always true due to diffraction resolution limitations). This may be because the measurement modes are redundant — they are not orthogonal and have a small inner product — or it may be because there are simply too few of them. The Shannon-Nyquist sampling theorem gives minimum requirements on the number of measurements needed to fully describe a scene. If the imaging system measures fewer than this number of modes, then no matter the type of modes measured, they will not fully describe the scene. In this situation the problem of estimating the scene from the measurements is underdetermined. However, perhaps surprisingly, using the techniques of *compressive imaging*, it is still possible to produce a unique and suitable image of the scene, even for very underdetermined measurement sets.

A computational imaging system relies heavily on the design of the measurement modes of the imaging system. This is where metamaterials enter the picture. A metamaterial is an artificial composite material that is designed to respond to light in engineered ways. Metamaterials are composed of individual subwavelength elements, such as loops of wire, small circuits, or dielectric blocks, which are arrayed in space

to create a bulk composite structure. Each of these elements has a controllable polarizability that may be designed to couple to either the electric or magnetic field of a light wave. The response of these elements to the different properties of an incident light wave may be engineered with exquisite control, in turn yielding exquisite control over how light scatters off the elements and propagates through the array. If these discrete metamaterial elements are substantially smaller than a wavelength (and several other conditions are met), then they may be homogenized such that the details of the individual elements may be disregarded in favor of equivalent bulk material properties. Hence, the composite material with all of its inhomogeneous engineered structure, and all of its control over light waves, may instead be thought of as a rather simpler homogeneous material — a metamaterial. Not only do metamaterials provide unprecedented control over the optical properties of the material, but properties not available in natural materials are also achievable.

Many types of optical devices with unprecedented capabilities have been developed using metamaterials. Perhaps most notable the are "invisibility cloaks" in which both the cloaking metamaterial structure and some internal cavity are rendered invisible.[9, 10, 11, 12, 13, 14, 15] Metamaterials have also been applied to the design of new types of lenses with novel performance. Gradient index lenses have been demonstrated from X-band [16] to W-band [17], where metamaterials allow the desired radially-varying index profile to be exactly realized. Entirely new types of abberation-free lenses requiring complexly varying index profiles [18] have been demonstrated in two- [19, 20, 21] and three-[22] dimensions. Some types of lenses that require material properties not found in nature, such as the negative index superlens [23] and the hyperlens[24] have been demonstrated using metamaterials.

The control over light provided by metamaterials makes them an ideal tool to craft the measurement modes of an imaging system. Conversely, computational imaging uses the information that that can be measured by an imaging system,

which may limited, in an optimal way, thereby producing the best possible image within the physical constraints of the system. The synergy of these two technologies, metamaterials and computational imaging, allows for entirely novel imaging systems.

The properties that make metamaterials particularly useful for computational imaging may be grouped into three categories:

1. Control of Mode Formation. A metamaterial aperture can be thought of as a hologram that transforms between detector mode(s) and sensing mode(s). Like computational holography, the modes you can make are limited by the holograms you can actually manufacture at a given frequency. For computational imaging we want to be able to generate carefully crafted and potentially unusual (from the perspective of a traditional optical or radar system) modes. The spatial and frequency control over material properties afforded by metamaterials yields unique control and flexibility of the hologram's properties and the modes it produces.

2. Mode Indexing and Multiplexing. The issue for any signal transmission system is how to maximize the information throughput given some physical constraints. For imaging, this means how do we measure as many useful measurement modes as possible given some allowable system size/bandwidth/number of detectors/type of detector. Because the responses of metamaterials to different properties of light can be extensively controlled, they yield many avenues for such mode multiplexing. Some possible schemes are:

    - Detector angle/position multiplexing. This is the approach used in traditional imaging but is usually limited to the generation of beam-type modes. With a complicated hologram, we can make a system that detects different arbitrary modes for different detector positions.

- Frequency/wavelength multiplexing. The frequency dispersion of resonant radiators can be leveraged to produce radiation modes that vary with frequency.
- Spatial/temporal waveform multiplexing. This is different from simply combining measurements obtained in methods a) and b) in that the relative phases of the modes produced by each source position/frequency change the overall mode sensed by the system.
- Polarization multiplexing. The anisotropy possible with metamaterials makes controlling the response to different polarizations possible.
- Amplitude multiplexing. A non-linear metamaterial hologram could make different modes for different signal intensities.

3. Mode Tunability. Making a reconfigurable aperture is key to creating imaging systems with extraordinary capabilities. Dynamically reconfiguring a metamaterial aperture would enable the generation of idealized measurement modes, which optimize the information collected with each measurement. In addition, the ability to tune the imaging aperture would allow the measurement modes to be dynamically adapted as we gain additional knowledge of the scene. A reconfigurable aperture also allows full images to be formed at every frequency of interest enabling hyperspectral imaging. Resonant metamaterials have high sensitivity to their geometry and environment which makes them highly tunable. Their resonance frequency, scattering strength, and polarization response can all be drastically changed. By modifying the behavior of individual metamaterial resonators, arbitrary holograms could be 'written' on the aperture. Thus apertures made of metamaterials may be highly tunable.

These contributions are realized in the concept of a frequency-diverse metamaterial imaging system that will be presented in this thesis. This *metaimager* uses

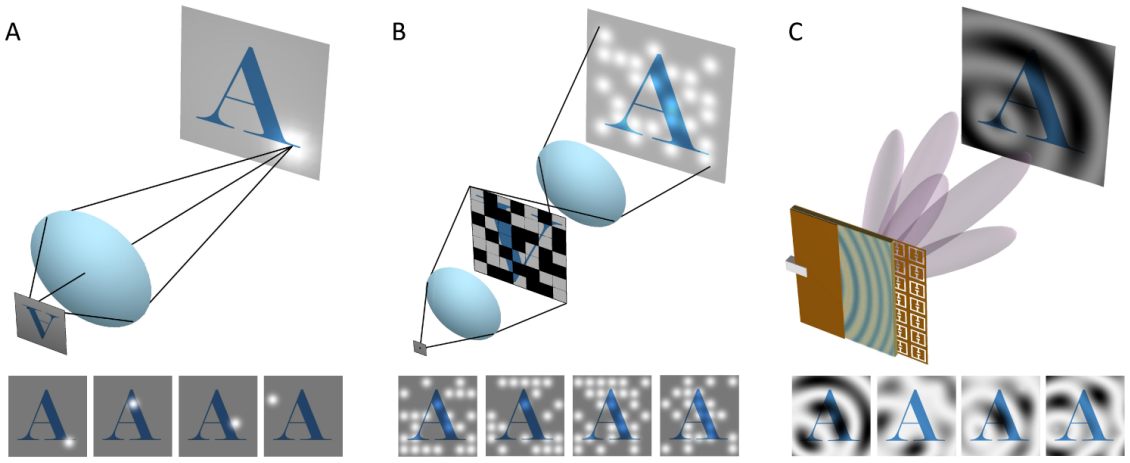

FIGURE 1.1: Comparison of (A) conventional and (B, C) computational imaging schemes. A conventional imager uses a lens to form measurement modes that effectively map all parts of an object to a detector/image plane. Each mode contributes highly specific and localized information, and all modes can be captured simultaneously using a pixel array or other detector. Within single pixel schemes, many types of modes can be used to form the image, with measurements being captured sequentially. In the example shown in (B), a reconfigurable random mask and two lenses are used to sequentially project intensity-only modes that sample the entire scene with only a single detector. A microwave metamaterial imager (C) makes use of a planar waveguide that feeds a holographic array of ELCs, removing the need for lenses. The waveguide acts as a coherent single pixel device, with the array of ELCs serving to produce the illuminating complex spatial modes.

the same electromagnetic flexibility that metamaterials have shown in many other contexts[25, 26, 27, 28, 29, 30] to construct an imaging aperture suitable for single-pixel operation that can measure arbitrary measurement modes, constrained only by the size of the aperture and resonant elements. It has no lenses, no moving parts, a small form-factor, and is low-cost.

Much of the previous work on compressive imaging systems has been based on digital micromirror devices (DMMs)[31, 32, 33, 34, 35, 36, 37], structured-illumination[38, 39], or variable transparency masks[40] to generate the imaging modes used to sense the scene. This form of mask-based compressive imaging, depicted in Fig. 1.1B, uses a traditional lens to form an image of the scene on a mask and then uses a second

lens to focus this masked image onto a single detector. By sequentially stepping through a series of masks, the modes needed to generate an image may be measured. In order to minimize the acquisition time, these systems often undersample the scene and employ compressive imaging techniques to reconstruct the image. The advantage of such an approach is that only a single detector (pixel) is needed - a tremendously valuable capability at frequencies where detectors are large and/or expensive. This form of single-pixel compressed imaging has been done at optical frequencies[41], and at terahertz using random static[40] and dynamic[42] masks. Some other work, particularly on compressive holography[43, 44], has abandoned these traditional lens-based imaging systems entirely, instead using the concepts of computational and compressive imaging to produce imaging systems with entirely new capabilities. Inspired by this previous work, the work presented here attempts to use the control provided by metamaterials to further extend the hardware implementations enabled by computational imaging, yielding imaging systems.

In chapter 2 we present an overview of work done by the author in the area of metamaterial lenses. We first introduce the concept of a metamaterial lens by demonstrating a simple gradient-index lens, then discuss more novel transformation-optical lenses enabled by metamaterials. In chapter 3 we unite these seemingly unrelated imaging systems under the umbrella of computational imaging. We introduce the theory of computational imaging, compressed sensing, and fourier optics, and derive the forward model needed to apply computational imaging to the metaimager system. In chapter 4 we describe the details of the metamaterials used to construct the first metaimager and their application to metamaterial antennas. In chapter 5 we describe the experimental tools needed to characterize the metaimager. In chapter 6 we describe the design, operation, and imaging results for a one-dimensional and a two-dimensional metaimager. Finally, in chapter 7 we describe the methods of tuning metamaterial radiators and describe several systems that have been designed

for the integration of tuning into metamaterial imaging systems.

2

Metamaterial Lenses

The flexibility of metamaterials makes them useful for making novel types of lenses. The natural starting point is for gradient-index (GRIN) lenses. The power of metamaterial design is not only in their ability to make materials with unusual properties (though these may enable interesting lenses as well), but also in the capability to fabricate metamaterials with optical properties that vary arbitrarily in space. While the lenses that most people are familiar with are made of a pieces of homogeneous material and obtain their focusing behavior from the shape of the lens's boundary, there exist many lens designs that obtain their focusing behavior not from the boundary shape but from index of refraction distributions that vary spatially within the lens. These GRIN lens designs may have performance that is superior in some respects to homogeneous lenses, but at the expense of being difficult or impossible to actually fabricate. Actual implementations of GRIN lenses are limited to the design space of what engineers know how to fabricate - a subspace of all possible GRIN lens designs. Metamaterials help to expand this design space by allowing lens designers to fabricate devices with almost any index distribution. Gradient index lenses have been demonstrated from X-band [16] to W-band [17], where metamaterials allow the

desired radially-varying index profile to be exactly realized.

2.1 Gradient index metamaterial lens with holey-dielectrics

To demonstrate the ability of metamaterials to make arbitrary GRIN lenses, we have designed and fabricated a 'holey' dielectric metamaterial GRIN lens. The goal of this lens was to demonstrate a design and fabrication technique that allows arbitrary index distributions to be created. As always with metamaterials, the unit-cell size must be much smaller than the wavelength of the light it is designed to interact with. This makes fabrication of metamaterial devices much more challenging at smaller wavelengths. This challenge was in mind in developing this holey dielectric technique as we wanted a methodology that could be scaled from RF down to optical devices. The work in this section was published by Hunt *et al.* in [45].

Gradient index (GRIN) metamaterials may be designed using spatially varying distributions of inclusions, usually holes or columns, in a dielectric matrix by employing an appropriate effective medium approximation. These distributions should be crystalline because the effective medium is then defined over the smallest possible length scale, one unit cell, and Rayleigh scattering is minimized as compared to an amorphous distribution.[46] In addition, these distributions should have hexagonal symmetry since this allows for the largest range of achievable indices and good isotropy.[47] This is a particularity useful method for fabricating devices operating at IR or visible wavelengths because uniformly sized holes or columns in a dielectric are easy to make with precise positioning. Hole/column distributions have been used to create IR carpet cloaks [12, 13] and microwave luneburg lenses[20] among other things. Photonic crystals (PCs) with spatially varying lattice constant[48, 49] and graded index[50] have also been studied. By spatially varying the lattice constant in a PC, the bandstructure can be spatially varied smoothly. These structures may have applications in waveguide couplers,[51] slow light optical buffers,[48] and high-Q

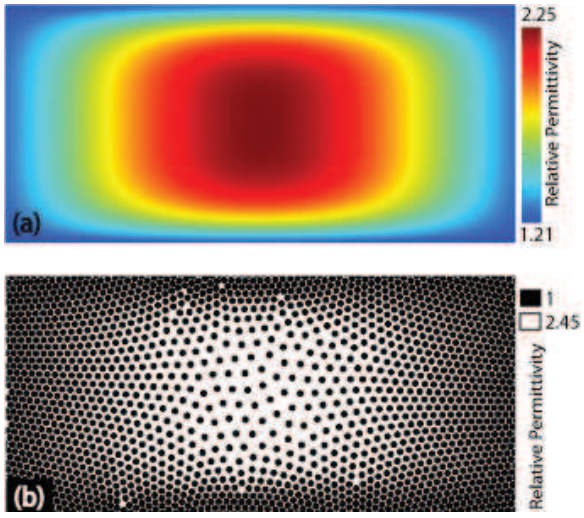

FIGURE 2.1: (a) The continuous permittivity map for the 2D TE GRIN lens. (b) The corresponding hole distribution.

lasers.[52]

For GRIN designs, it is possible to vary the size of inclusions at each grid point on a regular grid to achieve the desired index, [53] but for IR applications this significantly complicates processing and the range of realizable hole diameters may be limited, limiting the range of achievable indices. Here we propose a method to generate a hexagonal semi-crystalline distribution of uniformly sized inclusions with an arbitrarily varying lattice constant (Fig. 2.1).

In this method, the inclusions are treated as an analogous system of attractive particles of finite size, where the size, or interaction length, of each particle is dependent on its position. The system of particles is allowed to dynamically relax from some initial configuration according to interaction rules defined such that the equilibrium arrangement will have the desired lattice constant distribution. The desired lattice constant distribution is chosen such that the density of inclusions gives the desired refractive index when an appropriate homogenization is applied. The details of this design process are given in Appendix A.

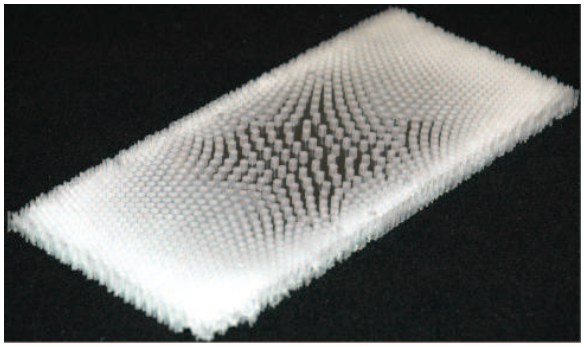

FIGURE 2.2: The fabricated polycarbonate lens. The lens size is 0.220m by 0.1016m by 0.01m and the hole diameter is 3mm.

We have applied this technique to design a two-dimensional microwave GRIN lens using air holes drilled in a polycarbonate slab (Fig. 2.2). In a simple quartic GRIN lens, the index is constant parallel to the optical axis so reflections occur at the interfaces. Our lens's index profile was designed by modifying a quartic GRIN lens to have an index variation along the optical axis so that the interfaces are nearly impedance matched to air, thus minimizing reflections. The index profile of the matched GRIN lens was determined by using Comsol Optimization Lab to maximize the far-field intensity of a plane wave produced by a point source located on the optical axis. A 2.1dB increase in the far-field intensity compared to the unmatched lens was obtained. The maximum achievable index was determined by Eq. A.8 and our minimum machinable hole size, while the minimum achievable index was limited by the percolation condition of Eq. A.7. The index profile has the form,

$$n_{min} + (n_{max} - n_{min})(1 + Ax^4 + Bx^2)(1 - 2\left(\frac{y}{h}\right)^4) \tag{2.1}$$

where n_{min} is the minimum achievable index, n_{max} is the maximum achievable index, h is the thickness of the lens, and A and B are constants determined by numerical optimization using Comsol Optimization Lab. The optical axis is coincident with the y-axis and the lens is centered at the origin.

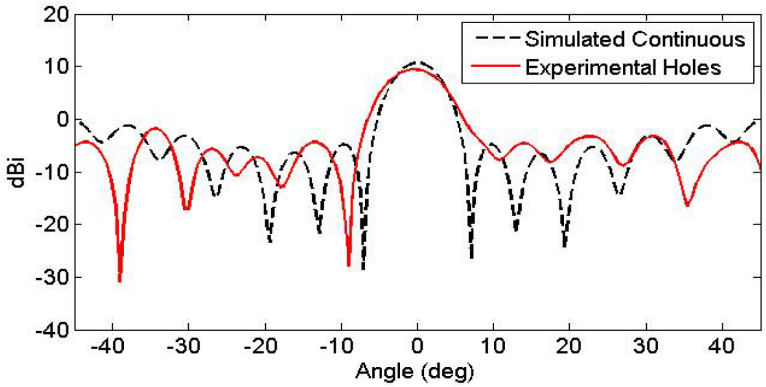

FIGURE 2.3: Far-field radiation patterns for the simulated continuous index lens and the experimental holes-only lens at 10GHz and 0° incidence.

Fig. 2.1 shows the relative permittivity profile for the matched lens, and the resulting hole distribution. The near-field distribution was measured using a 2D electric field mapper.[10] The performance of the lens was then quantified by calculating the far-field pattern of the lens using a 2D Kirchhoff integral and comparing it to the simulated continuous lens, as shown in Fig. 2.3. The experimental lens exhibits a gain of 9.4dBi and a beam full-width-at-half-max (FWHM) of 7.2°, while the simulated lens has a gain of 10.6dBi and a FWHM of 6.2°.

In this section, we have described a technique to generate semi-crystalline distributions of particles with arbitrary lattice constant distributions. This method has applications in GRIN devices and photonic crystals, and is particularly suited to the design of IR and visible wavelength devices. We have used this technique to design and implement a microwave GRIN metamaterial lens composed only of uniformly sized holes drilled in a dielectric slab. This binary metamaterial lens shows performance very close to that of the simulated continuous-index lens. It should be noted that, while we have described and demonstrated this technique for two dimensional systems, it is readily generalizable to three dimensions.

2.2 Transformation-optical lenses

We have shown how an arbitrary GRIN lens may be designed and fabricated with metamaterials, but this lens was designed in a rather uninformed manner. It was simply parabolic GRIN lens — which makes a paraxial, small-angle, approximation — to which some additional optimization was applied to reduce reflections from the lens input and output boundaries. An additional power of metamaterials s that when the designer is no longer constrained by fabrication, entirely new design methodologies may be developed and employed. An example of this is the the recently developed technique of transformation optics (TO) which establishes a connection between mathematical spatial transformations of light and physical material optical properties that implement these transformations. The connection with metamaterials is that the material properties specified by TO are often not found in natural materials and are spatially varying. This design methodology may be employed to make entirely novel types of lenses. In this section we discuss the design process of TO, and in the following sections we apply it to modify several different types of lenses. The discussion in this section comes from work published by Hunt *et al.* in [54].

Transformation optics (TO) is a design methodology in which coordinate transformations are applied as a conceptual means of controlling the trajectories of waves. If a coordinate transformation can be found that manipulates waves in a certain way, the form invariance of Maxwell's equations can then be exploited to find the exact specification for a medium that will produce the identical wave manipulation. Many unique devices can thus be conceived in a simple manner via the TO approach, perhaps most notably the "invisibility cloak," in which a finite volume of space is compressed to a singular point with negligible scattering.[9, 10, 11, 12, 13]

In general, the media specified by coordinate transformations are anisotropic and

possess both electric and magnetic response. Moreover, the constitutive parameters for such media tend to vary as a function of position in space, so that general TO media can be viewed as extremely complex forms of gradient index (GRIN) media. Though TO media are complex, the conceptual simplicity brought to the design process makes TO an intriguing starting point for introducing unique modifications to optical devices; further optimization can provide more practical and useful incarnations.

A potentially fruitful application of TO is the modification of a spherically symmetric GRIN lens. GRIN lenses such as the Luneburg, Eaton or Maxwell fisheye lenses are perfect imaging devices from a geometrical optics perspective, in that rays emanating from one point are perfectly focused to another point. The Luneburg, for example, is a wide field-of-view lens that perfectly focuses rays from a point at infinity onto a point on a spherical surface. The spherical image surface renders the Luneburg a poor match for planar detector arrays and limits its utility.[55] As another example, the Eaton lens can act as a retroreflector with perfect image fidelity, yet contains a singularity in its radial index profile, similarly making it unfeasible for practical implementation.[56]

TO has proved a compelling approach for the redesign of Luneburg-type lenses. Ma et al., for example, illustrated that the singularity associated with the Eaton lens could be transmuted into a topological defect through the use of a radial transformation. A metamaterial version of the TO-modified Eaton lens demonstrated its operation could, in fact, be achieved.[57] In a different context, a straightforward class of transformations was proposed in which a portion of a Luneburg lens could be flattened and thus made compatible with planar detector arrays.[18, 19] In these cases, the TO transformations are simple to visualize, yet the potential improvements to the devices are profound.

In the TO design process, a coordinate transformation is applied to a space which

may or may not contain an optical element. Solutions to Maxwell's equations in the original, "virtual", space and the transformed, "physical", space are the same when viewed in their respective coordinate systems. However, if the solution in the original space is viewed in the transformed space it will appear distorted. This transformation can be implemented in the physical space by varying the constitutive parameters, permittivity ($\boldsymbol{\epsilon}$) and permeability ($\boldsymbol{\mu}$), of the physical space in a manner according to the transformation, as given by

$$\boldsymbol{\epsilon}_{\boldsymbol{i'j'}} = \frac{\boldsymbol{A}_{\boldsymbol{i}}^{\boldsymbol{i'}} \boldsymbol{A}_{\boldsymbol{j}}^{\boldsymbol{j'}}}{Det(\boldsymbol{A})} \boldsymbol{\epsilon}_{\boldsymbol{ij}} \tag{2.2}$$

and,

$$\boldsymbol{\mu}_{\boldsymbol{i'j'}} = \frac{\boldsymbol{A}_{\boldsymbol{i}}^{\boldsymbol{i'}} \boldsymbol{A}_{\boldsymbol{j}}^{\boldsymbol{j'}}}{Det(\boldsymbol{A})} \boldsymbol{\mu}_{\boldsymbol{ij}} \tag{2.3}$$

where $A_i^j = dx_j/dx_i$ is the Jacobian of the coordinate transformation and the unprimed and primed indices indicate the spatial coordinates in the original and transformed spaces, respectively.[9] When light travels through the material embedded in the physical space, it behaves as though it is traveling through the virtual space.

While possible in theory, metamaterial elements that control more than just a few tensor components of $\boldsymbol{\epsilon}$ and $\boldsymbol{\mu}$ are exceedingly difficult to design. Designing materials with simultaneous control of $\boldsymbol{\epsilon}$ and $\boldsymbol{\mu}$ may be further complicated by magnetoelectric coupling between unit cells.[58, 59] Additionally, tensor elements with values less than one require either resonant elements which inherently increase absorption and reduce bandwidth, or diamagnetic elements which only provide permeability and only between zero and one.[60, 61] It is thus useful to perform an optimization step in which the complexity of the anticipated medium is reduced as much as

possible, while retaining as much of the performance as possible. For the TO lens considered in the following sections, only the boundaries of the transformed space are constrained, which is often all we want to modify. Thus, an infinite number of possible coordinate transformations are available that meet the boundary conditions while varying the space between boundaries arbitrarily. These transformations may vary distinctly in the complexity of the constitutive parameters prescribed by Eqns. 2.2 and 2.3, and carefully choosing from among them may allow for substantial simplifications of the material design. A particulary useful type of two-dimensional (2D) transformation, called a conformal transformation, results in $\boldsymbol{\epsilon}$ and $\boldsymbol{\mu}$ with zero-valued off-diagonal tensor components and in-plane diagonal components equal to one.[62, 63] If a conformal transformation can be found that meets the boundary conditions, then the complexity of the material needed to implement the transformation is significantly reduced. The existence of a conformal transformation is not guaranteed for any boundary transformation but can often be well approximated with a quasi-conformal transformation (QCTO) which minimizes the in-plane anisotropy of $\boldsymbol{\epsilon}$ and $\boldsymbol{\mu}$.[64] Such a transformation can be found numerically using previously reported techniques.[65, 66]

2.3 Microwave transformation-optical Luneburg lens

To demonstrate the power of transformation optics and metamaterials, we have applied the TO design methodology to modify a Luneburg lens to have a more desirable geometry. The Luneburg lens is a powerful type of GRIN imaging device. It exhibits aberration free focusing for parallel rays incident from any direction. However, its advantages are offset by a focal surface that is spherical and thus difficult to integrate with standard planar detector and emitter arrays. Using TO, it is possible to transform the curved focal surface to a flat plane while maintaining the perfect focusing behavior of the Luneburg over a wide field of view. Here we apply these techniques

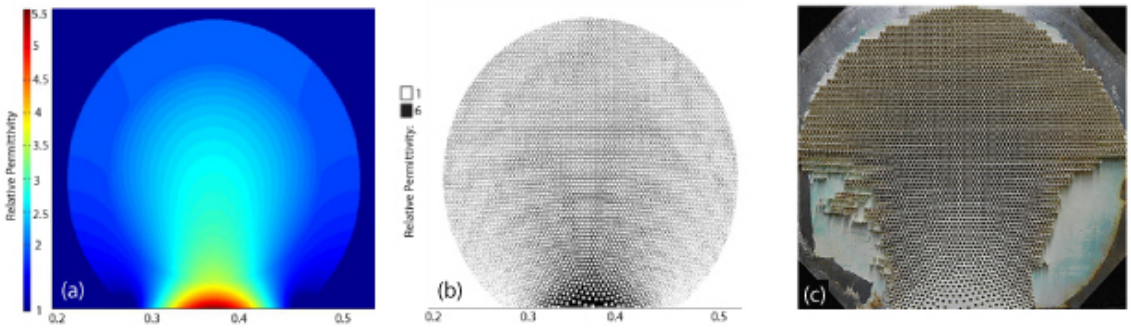

FIGURE 2.4: (a)The continuous permittivity map for the 2D TE compressed refractive luneburg lens (note the permittivity of two at the outer boundary), (b) a distribution of holes with the same effective permittivity and (c) the fabricated lens. The hole diameter is $1/8^{th}$ inch and the slab thickness is $1cm$. All distances are in meters.

to a lesser-known refractive Luneburg lens and implement the design with a metamaterial composed of a semi-crystalline distribution of holes drilled in a dielectric. In addition, we investigate the abberations introduced by various approximations made in the implementation of the lens. The resulting design has improved mechanical strength with small abberations and is ideally suited to implementation at infrared and visible wavelengths. The work in this section was published by Hunt *et al.* in [67].

A Luneburg lens is a GRIN lens with a spherically or cylindrically symmetric index distribution that exhibits aberration-free focusing of light incident from any direction onto a spherical or cylindrical surface [55, 68]. Despite its advantageous imaging properties, however, the Luneburg is not widely used since its focal surface is not compatible with standard detector and transmitter arrays. The unique properties of a Luneburg lens or similar optical element can be accessed utilizing a detector array built on a nonplanar surface that conforms to the focal surface of the device.[69] Alternatively, the possibility exists to seek a gradient index profile that retains the nearly ideal optical properties of the Luneburg lens, but allows one or more surfaces to be planar. Such a design was suggested in the context of the

emerging field of transformation optics, where it was shown that a simple analytic coordinate transformation could be applied to flatten one side of the lens.[18] While the initially suggested transformation required a complex, anisotropic medium, Kundtz et al. have investigated the possibility of obtaining numerical transformations that, at least for cylindrical lenses with transverse electric (TE) polarization, result in a Luneburg lens with a flattened focal plane that can be implemented using only isotropic GRIN media.[19] The resulting lens retains nearly identical optical characteristics as the untransformed lens but focuses onto a flat surface over a limited field of view.

In the flattened Luneburg lens reported by Kundtz et. al. prior to this work, the necessary isotropic permittivity distribution was implemented using an artificially structured metamaterial comprising non-resonant electric dipoles of varying size. This method of implementation may not scale well towards infrared (IR) and visible wavelengths, however, since metals behave less as conductors and increasingly like lossy dielectrics. Thus, for better scalability, a dielectric-only implementation would be preferable. In addition, it would be advantageous for the entire device to be fabricated from a single dielectric slab using routinely available lithographic techniques. A simple way of achieving these requirements is to drill uniformly sized sub-wavelength diameter holes in a dielectric slab such that the density of holes in a given location yields the desired index at that location. This approach has been used to fabricate a variety of quasi-conformal transformation optics devices, such as "carpet cloaks", that operate at IR wavelengths.[12, 13]

The index profile for a standard Luneburg lens of unit radius is given by,[70]

$$n(r) = \sqrt{2 - r^2} \tag{2.4}$$

This distribution is difficult to implement assuming uniformly sized holes drilled into a host dielectric, because the index goes to unity at the lens boundary. Since

the holes have some minimum spacing after which they overlap, an index of unity cannot be achieved since the overall device loses mechanical integrity. Fortunately, the index distribution specified by Eq. 2.4 is not the only solution to the Luneburg lens problem - it is a special case of a more general solution which allows for designs that have non-unity index at the boundary. These refractive Luneburg lenses exhibit some refraction at the lens boundary but still result in perfect focusing. For a lens with a minimum outer index of n_0, the index, n, and corresponding radial distance, r, are given by the parametric equations,[70]

$$\Omega(\alpha) = \frac{2}{\pi} \int_{\frac{1}{n_0}}^{1} \frac{1}{r'} atan \left[\frac{1-\alpha^2}{(n_0 r')^2 - 1} \right]^{\frac{1}{2}} dr' \tag{2.5}$$

$$n(\alpha) = \begin{cases} n_0 \sqrt{1 + (1-\alpha^2)^{\frac{1}{2}}}\ e^{-\Omega(\alpha)} & , \ \alpha \leqslant 1 \\ n_0 & , \ \alpha > 1 \end{cases} \tag{2.6}$$

$$r(\alpha) = \frac{\alpha}{n(\alpha)} \tag{2.7}$$

where the parameter α goes from zero to n_0.

In the present refractive Luneburg design, the index value at the lens boundary is determined by the minimum allowed separation of the holes, which is in turn determined by fabrication and mechanical strength constraints.

Once a profile for the untransformed refractive Luneburg lens is obtained, a coordinate transformation is applied that flattens one surface of the lens.[19] Quasi-conformal optimization is applied to the transformation, such that any anisotropy is minimized and can be neglected in the final structure. The material properties (the index of refraction distribution) needed to implement this transformation are then obtained from the TO equations. The degree of flattening of the lens, and thus its field-of-view, is ultimately determined by the dielectric constant of the host dielectric material.

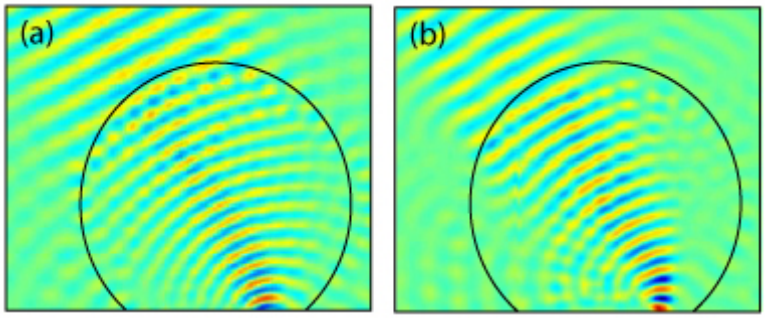

FIGURE 2.5: Out of plane electric field for a 30 degree incident plane wave for the (a) simulated continuous index lens and (b) the measured, fabricated lens. A 10 GHz source was used in both the simulation and the experiment.

When a continuous index profile has been determined, a method for translating that index profile into a distribution of holes must be employed. Again, we use the hole-relaxation design technique discussed in 2.1 and A to come up with a holey-dielectric metamaterial.[45]

To investigate the performance of the flattened refractive Luneburg lens, we chose to fabricate and characterize an implementation designed to operate over a broad range of frequencies in the microwave range (at least spanning the 8-12 GHz band measurable in our apparatus). The untransformed lens had a diameter of ten free space wavelengths at our central frequency. The transformation was truncated at the transformed lens boundary. The lens was machined from a slab of low-loss polymer-ceramic with index of $\sqrt{6}$. The selected design of the refractive Luneburg called for an index of $\sqrt{2}$ at the outer boundary. The host index allows the lens to be compressed by 13.4 percent of the radius, giving a field of view of $\pm 30^o$. The lens comprises 7979 holes. To achieve the aspect ratio required it was necessary for the lens to be drilled halfway through from both sides of the slab using a computer controlled milling machine. Holes of diameter $1/8^{th}$ inch were drilled into the ceramic composite material. The lens was fabricated by Tim Perram and Dr. Anthony Starr at SensorMetrix.

Fig. 2.4 shows the optimized relative permittivity distribution for the flattened lens, the hole distribution computed by the particle interaction approach described in Appendix A, and the final fabricated lens. Plots of the simulated and measured electric field distributions are shown in Fig. 2.5. The field distribution was measured using a 2D electric field mapping apparatus previously reported.[71] For both the simulations and the experimental measurements, a source was placed at the focal plane of the lens, with a roughly collimated beam expected as the output. In the experimental setup, the source consisted of a dielectric rod waveguide with square cross-section coupled to the focal surface of the lens. Simulations were performed using COMSOL Multiphysics, a commercial finite element solver. The agreement between the simulated and measured field patterns was found to be excellent.

In this implementation of the flattened Luneburg, two approximations of the index distribution prescribed by the transformation were made. Because the transformation ideally extends through all space, the free space index outside the untransformed lens is also modified. In order to perfectly preserve the behavior of the Luneburg, the entire transformation should be implemented, but to make a reasonably sized lens the transformation should be truncated close to the transformed lens's boundary. The deviation from unity index decreases with distance from the lens, but at some point the transformation must be truncated and the index set to one. Thus the first approximation is to set the transformation index to one beyond some radius. Rays incident from free space outside the transformed region will refract at the boundary, slightly distorting their paths. In addition, they will not be guided by the transformation where it has been truncated. For the lens implemented here, the transformation was truncated at the boundary of the transformed lens.

The second approximation has a slightly more severe effect. For regions at the edges of the flattened region of the lens, the transformation indices take values less than one. To avoid using resonant metamaterials, these indices must be approxi-

mated as one. This reduces the aperture of the lens because rays that enter the lens at the edge of the aperture, or rays incident from the side of the lens, must pass through these $n < 1$ regions and so are not steered correctly when these regions are removed.

When the $n < 1$ regions of the lens are set to one, rays that pass near the center of the lens are still focused correctly but rays that pass near the edge of the lens aperture are not, reducing the effective aperture of the lens. For rays near normal incidence this approximation has little effect because the only rays that travel through this $n < 1$ region are the rays very close to the edge of the lens aperture. This becomes more of a problem for rays incident far off normal because more rays must travel directly trough the $n < 1$ region outside the lens before entering the lens. Beyond a certain angle, the spot diagram rapidly spreads out. This is the angle at which rays begin to pass trough the $n < 1$ region outside the lens.

2.4 Infrared transformation-optical Luneburg lens

As mentioned in Section 2.1, the holey dielectric metamaterial was designed with the explicit intention of scalability to small wavelengths. In this section we demonstrate a TO flattened 2D Luneburg lens similar to that of Section 2.3 that operates at infrared wavelengths. The work in this section was published by Hunt *et al.* in [21].

The index profile for a Luneburg is given by Eq. 2.4 and shown in Fig. 2.6 (a). By applying a quasi-conformal transformation that flattens a section of the lens surface and applying the equations of TO, a new index distribution that focuses light to a flat surface, shown in Fig. 2.6 (b), is obtained [15-17]. As the degree of flattening increases, the maximum required index also increases. The degree of flattening, and thus the field of view of the lens is determined by the index of the host dielectric.

In previous microwave realizations of flattened TO Luneburg lenses, the transformation was truncated at the lens boundary. This truncation was a reasonable

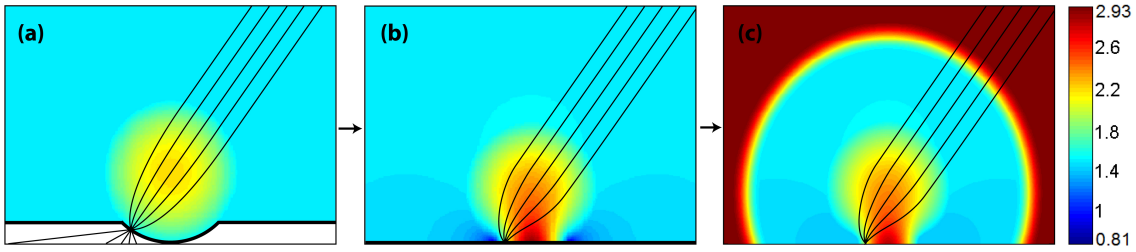

FIGURE 2.6: Raytraces through IR Luneburg index distributions. (a) The original 2D Luneburg lens, (b) the flattened Luneburg lens, and (c) the fabricated flattened Luneburg lens. The bold black line in (a) and (b) shows the transformed boundary. The range of indexes of the flattened lens, (b), have increased compared to the original lens, (a). In the fabricated lens, (c), indices less than 1.5 have been approximated as 1.5 to maintain waveguiding, and the transformation has been truncated with an index matching region that matches the transformation to the waveguide index.

approximation of the transformed lens because the index required by the transformation outside the lens, while having some spatial variation, was close to unity everywhere [16,17]. Because the device implemented here is embedded in a slab waveguide — essentially a high index background — a similar truncation is not suitable since it would introduce refraction at the lens interface. For the present work, the transformation is truncated at a distance of $2.5r_{lens}$ from the center of the lens, so that the flattened lens is surrounded by a circular low index region concentric with the center of the transformed lens. Not only does including this region avoid unwanted refraction at the lens-waveguide interface, but because more of the transformation is included spherical aberrations introduced by truncating the transformation are reduced [17]. At the boundary of the transformation, we must transition to the unpatterned waveguide. This is achieved by matching the index at the boundary of the transformation to the index of the slab waveguide with a low-reflection index matching region. In addition, the transformation also introduces spatial regions where the refractive index assumes values below unity. Values of refractive index less than unity are undesirable, as they imply frequency dispersion and hence introduce bandwidth

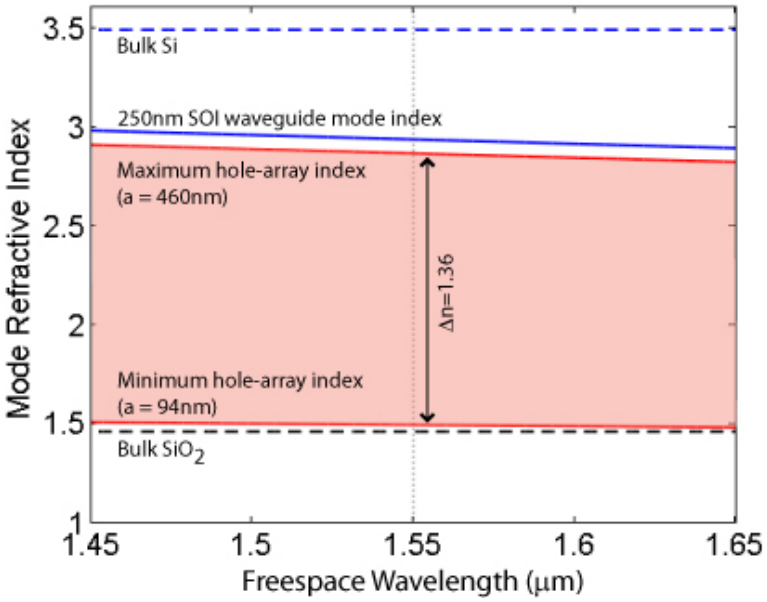

FIGURE 2.7: Effective index dispersion of IR slab waveguide. The dashed lines show the index of bulk Si and SiO2 while the solid lines show the effective mode index in the Si slab waveguide vs. frequency. The solid red region is the range of indexes achievable with the hole-array metamaterial used here. This region covers nearly the entire range of accessible indices and exhibits small dispersion.

limitations. Fortunately, approximating these regions by setting their index value to unity has little effect on the focusing behavior of the lens.[72] These modifications to the index profile of the transformed lens are shown in Fig. 2.6 (c).

To realize a GRIN device in a slab waveguide, sub-wavelength holes can be etched into silicon on insulator (SOI) to create a dielectric-only metamaterial. The specific distribution of holes was designed using the holey dielectric metamaterial design discussed in Section 2.1 and Appendix A.

The transformed lens had a diameter of ten free-space wavelengths or 15.5μm, and consisted of 84303 holes. Because our waveguide mode is TE_0, where the electric field is polarized perpendicular to the axis of the holes, the desired filling fraction was determined by applying the 2D Maxwell-Garnett effective medium (MG) formula for the homogenization of mixtures of cylindrical voids in a dielectric matrix. For the

permittivity of the matrix we used the square root of the mode index of our TE_0 mode [18]. For 1.55μm wavelength TE_0 mode in a 250nm thick SOI waveguide, this mode index is 2.93. The upper limit on the spacing of the holes, determined by the deviation of unit cell simulations from the MG mixing formula and the onset of photonic crystal effects, is 460nm. The lower limit was determined by fabrication constraints and in our case was 94nm for 85nm diameter holes. These limits allow us to vary the mode index from 1.5 to 2.86, as shown in Fig. 2.7. Since the minimum index cannot be smaller than the index of the bulk SiO_2 cladding layer, this index range covers nearly the entire range of available indices. The dispersion of this hole-array metamaterial is related to the dispersion of the mode index of the SOI slab. Over a wavelength range of 1.45μm-1.65μm the fundamental mode index varies only 1.5% from the design index of 2.93, giving a wide operation bandwidth.

The lens was designed to be excited by an array of four waveguides, each at a different location on the focal plane of the flattened lens. When an IR laser is coupled into its corresponding input grating, each 0.8μm wide input waveguide forms an approximate diffraction limited source on the image plane of the lens which produces a Gaussian plane wave in a different direction (Fig. 2.9 (b)-(e)). Because the lens is reciprocal, this is equivalent to focusing a plane wave to a point on the flattened focal surface. The output beam transitions from the low index region of the transformed free-space outside the lens to the high index unpatterned slab waveguide through an index matching region concentric with the center of the lens. For characterization purposes, the beam is then coupled out of the waveguide by a curved grating.

The fabrication process was designed and the samples were realized by Dr. Talmage Tyler and Dr. Sulochana Dhar in Dr. Nan Jokerst's group. Fabrication began with a <100> oriented SOI wafer with a Si top device layer thickness of 340nm and a buried oxide layer thickness of 2μm. In order to achieve the designed device layer thickness of 250nm, the SOI wafer was thermally oxidized such that 90nm of silicon

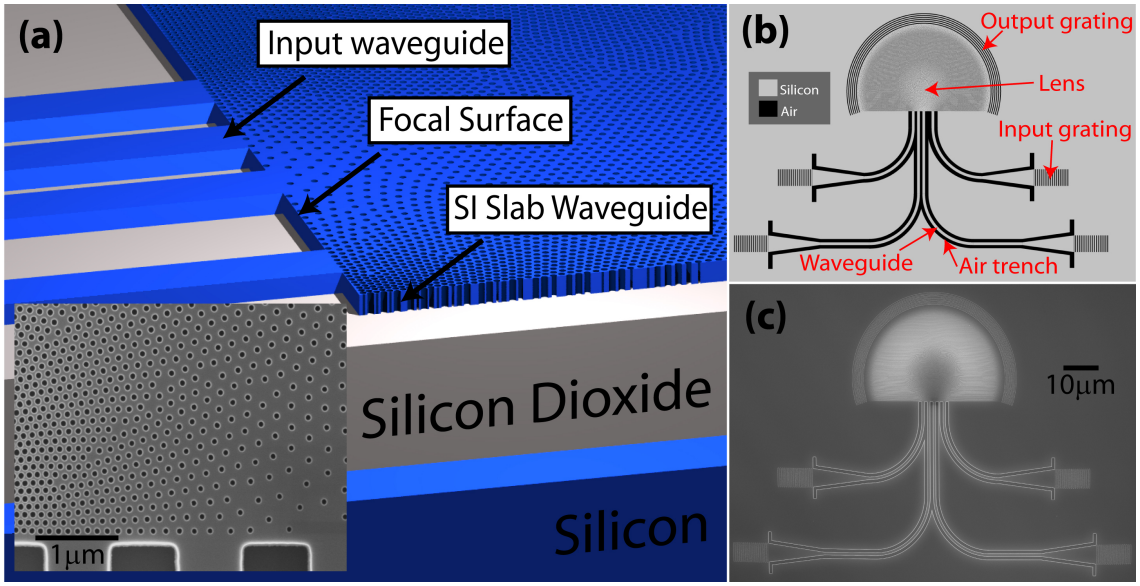

FIGURE 2.8: Fabricated IR TO Luneburg sample. (a) Cut-away view of the lens fabricated in silicon-on-insulator (SOI). Inset shows an SEM image of the same region of the lens where the local-crystallinity of the hole distribution can be seen. (b) Schematic of the fabricated lens. The pattern shown was etched through the Si slab using EBL followed by DRIE, stopping abruptly at SiO2 layer - except for the input/output gratings which only partially penetrate the Si slab. Input waveguides were defined by etching air trenches in the silicon slab-waveguide. (c) SEM image of the fabricated lens taken by Dr. Talmage Tyler in Dr. Nan Jokerst's group.

was consumed; the sacrificial oxide layer was then removed in buffered oxide etch, yielding a silicon device layer thickness of 250 nm. The hole pattern was achieved using electron beam lithography (EBL; Elinonix ELS-7500) followed by deep reactive ion etching (DRIE; SPTS Pegasus). DRIE (Bosch process) is extremely selective with respect to silicon versus silicon dioxide, so the etched holes pass completely through the silicon device layer and terminate abruptly at the buried oxide interface. A second EBL step was performed to define the four input gratings and the semi-circular output grating along the perimeter of the lens; again, DRIE was used to etch the silicon, but for the gratings the etch depth was 120nm. Finally, a third EBL step followed by DRIE was used to define the four input waveguides. Because the silicon device layer serves as the waveguide material, the the waveguides were

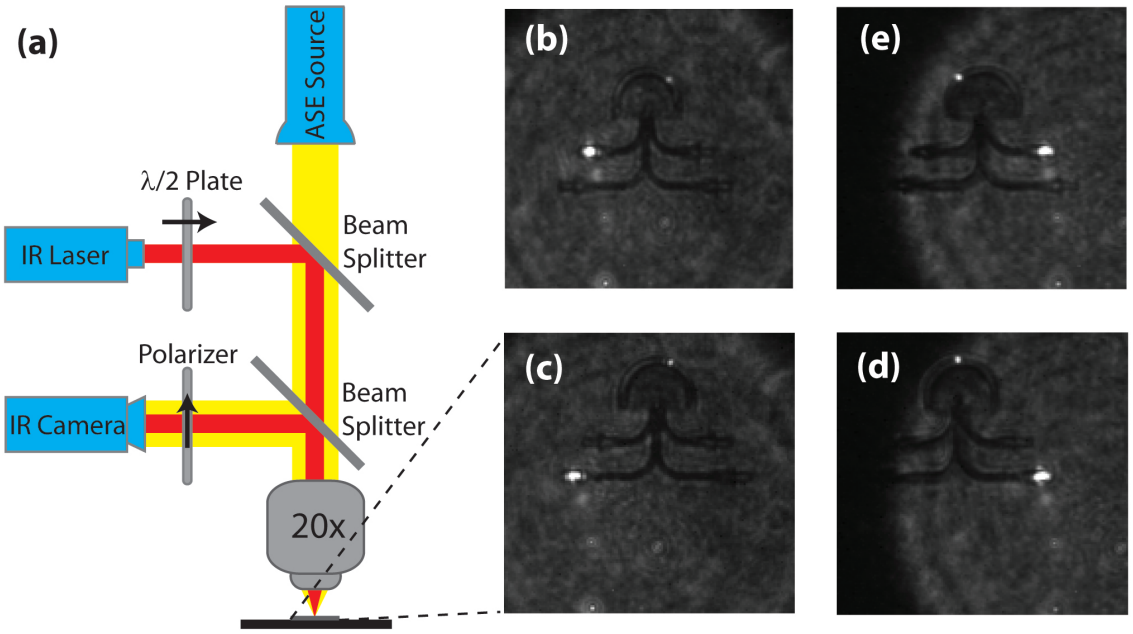

FIGURE 2.9: Experimental characterization of IR TO Luneburg was performed by Dr. Yu-Ju Tsai in Dr. David Smith's group. (a) The optical circuit of our characterization setup. An amplified spontaneous emission source was used to illuminate the entire lens, while a 1.55 m laser was focused to one of the four input gratings at a time. A CCD camera was used to image the lens and observe the location of the output beam. The half-wave plate and polarizer were oriented to partially filter the input illumination to reduce saturation of the CCD detector. (b)-(e) IR images of the lens with the IR laser coupled to each of the four input gratings.

defined by patterning 0.8μm wide trenches on both sides of the four waveguides; the trenches were fully etched and terminated on the buried of the SOI, thus providing air cladding on the sides of the waveguides.

The lens was characterized by Dr. Yu-Ju Tsai in Dr. David Smith's group. A $\lambda = 1.55\mu$m optical laser was coupled into each waveguide independently with a 20x objective lens and observing the location of the output spot on the output grating with an IR camera. The experimental setup and images of the operating device are shown in Fig. 2.9. The output beam direction was determined from the experimental images of the operating lens by measuring the position of the output spot relative to features on the lens structure. Due to the resolution of camera, there

is an uncertainty of 3.6^o in the measured angles.

Analysis of SEM images of the fabricated device showed that the input waveguides, which were patterned in a separate step from the lens hole array, were shifted by 170nm from the center line of the lens, which accounts for the offset of the central beam from the optical axis. Taking this shift into account, the experimentally measured beam directions agree very well with theory, and shows focusing over a range of incidence angles of $\pm 33.5^o$.

This was the first transformation-optical device based on a transformation of an existing GRIN device operating at IR wavelengths. Such an approach allows new optical elements to be designed that utilize the optical properties of existing devices, but enables the designer to reconfigure the geometry of the device to different more useful geometries, as demonstrated herein by the flattening of the focal surface of a Luneburg lens. By implementing this TO device with a dielectric-only hole-array metamaterial, it is possible to implement this new GRIN device in SOI with a broad bandwidth. The flattened Luneburg lens implemented here shows beam forming (focusing) from a planar focal surface over a wide field of view of 67^o, in excellent agreement with the theoretical perfect focusing of the Luneburg lens.

2.5 Microwave transformation-optical Maxwell Lens

The lenses discussed in Sections 2.1, 2.3, and 2.4 were all designed to image light from infinity to a focal plane. But lenses are much more versatile than this. In general a lens take a light distribution at one place in space and transforms it to another distribution at another place in space. The simplest example of this lensing behavior is a relay lens which aims to reproduce a light distribution at one plane to another plane with no distortion or scaling. In this section we discuss such a relay lens designed with TO and implemented with metamaterials. The work in this section was published by Hunt *et al.* in [54].

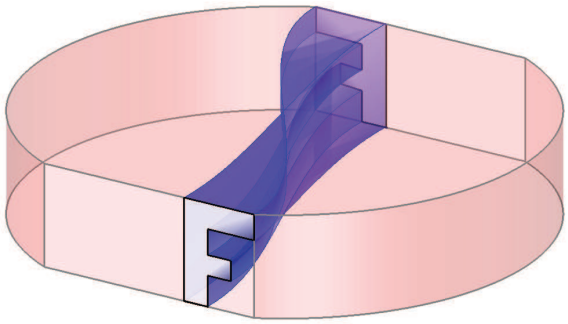

FIGURE 2.10: Ray trace through a perfect relay lens.

In this section we consider the design and implementation of a two-dimensional metamaterial relay lens, conceptually formed by flattening a Maxwell fisheye lens — a perfect imaging device — through the use of a coordinate transformation. The specifications for the constitutive parameters of the device are obtained using transformation optics (TO). To obtain a more favorable implementation of the lens, we seek a quasi-conformal TO (QCTO) transformation that minimizes the required anisotropy, such that the resulting lens can be formed using isotropic, dielectric-only media. We demonstrate such a flattened Maxwell lens at microwave frequencies using a non-resonant metamaterial and confirm its focusing and broad bandwidth behavior. Such planar, dielectric-only structures can be readily implemented in infrared and optical waveguides.

TO had been suggested as a means of forming a perfect relay lens from a Maxwell fisheye lens by Smith et al.[66]. The Maxwell lens is a spherical or cylindrical lens with a radially varying, azimuthally symmetric index profile that images a point on the boundary of the lens to a point on the opposite side of the lens. Like the examples cited above, the Maxwell lens is a perfect imaging instrument having zero geometrical optical aberrations. The index at radius r of the Maxwell lens is given by,

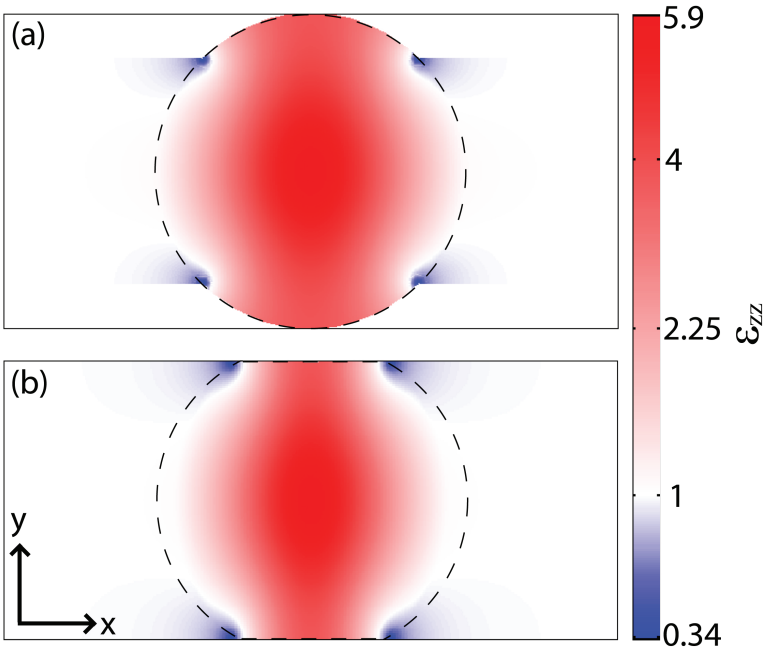

FIGURE 2.11: The permittivity distribution of the transformed Maxwell lens in (a) the virtual space and (b) the physical space. The red-blue transition shows the boundary between indexes above unity, realizable with non-resonant metamaterials, and indexes below unity, realizable only with resonant metamaterials

$$n(r) = \frac{n_0}{1 + (r/a)^2} \tag{2.8}$$

where n_0 is the index at the center of the lens and a is the radius of the lens.[55] With both sides of the Maxwell lens flattened, the resulting optical device would function as a perfect relay lens, projecting and inverting an image from one plane to the other. The relay lens represents an important optical element in many imaging instruments, including night vision systems, endoscopes, microscopes and photocopiers. As is common with most optical systems, relay lenses are typically composed of many singlet lenses, the combination of which minimize but do not eliminate geometrical aberrations. To the extent to which it is feasible, an aberration free, single element relay lens would be an extremely useful device.

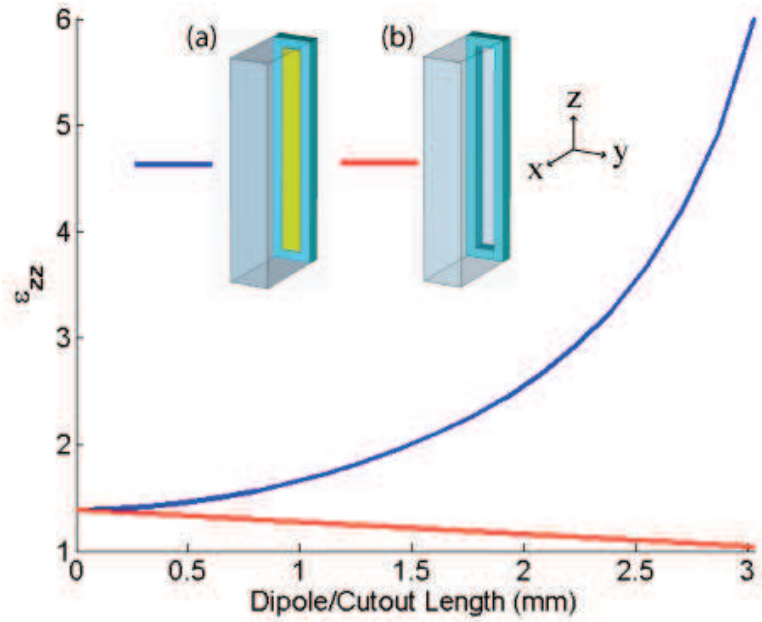

FIGURE 2.12: The two types of unit cells used to implement the Maxwell and their effective epsilon in the z-direction. (a) is the unit cell for the non-resonant electric dipole composed of copper on FR4 in air. (b) shows the unit cell for the air slot in FR4.

A quasi-conformal transformation that flattens opposite segments of the boundary of a Maxwell fisheye lens has recently been described by Smith et al.[66] This transformation of the fisheye lens is shown in Fig. 2.11. Since these flattened segments are mirrors of each other across the center of the lens, a point on one flattened boundary will be imaged to the opposite boundary, as seen in Fig. 2.10. This transformation preserves the perfect geometric optical properties of the fisheye lens, thus forming a perfect relay lens. As larger length segments of the lens are flattened, the magnitudes of the maximum and minimum required material responses increase.

We implemented a 2D version of the perfect relay lens using non-resonant metamaterials, so that the performance was broadband. To within the QCTO approximation that the in-plane diagonal tensor components are unity, the optimized transformation requires that only $\epsilon_{zz}(x, y)$ and $\mu_{zz}(x, y)$, the out of plane components,

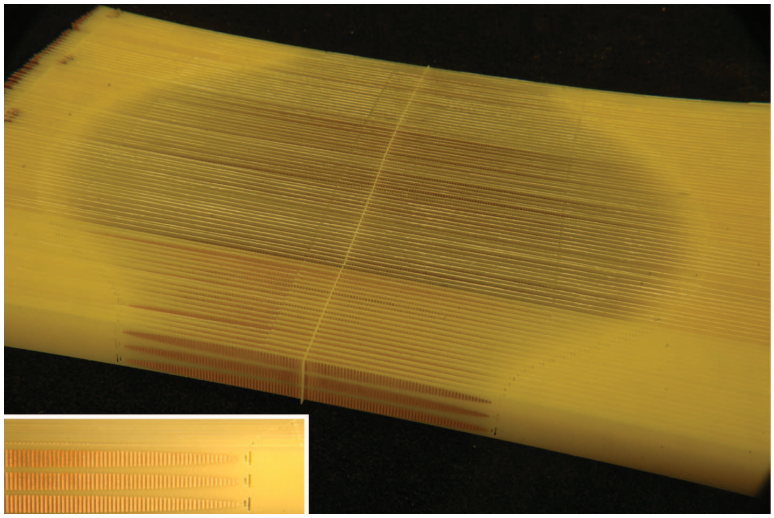

FIGURE 2.13: The fabricated metamaterial TO Maxwell relay lens.

be non-unity. If we further restrict the polarization of waves to be perpendicular to the plane of the transformation (TE) or in the plane of the transformation (TM), then only $\epsilon_{zz}(x, y)$ or $\mu_{zz}(x, y)$, respectively, need be controlled. Here we restrict the polarization to be TE, and fold the fisheye index profile of Eqn. 2.8 into the transformation by applying the transformation to the permittivity distribution in the virtual space $n(r)^2 = \epsilon_{zz}(r)$.

To achieve the required spatial variation of ϵ_{zz}, two variations of metamaterial elements were used. The first was a non-resonant, anisotropic split-wire copper wire patterned on FR4. The second was a slot-like void in the FR4. The combination of these two unit cells allows all indexes from nearly one up to 2.46 to be reached. The split wire structure acts like an electrically polarizable inclusion in the FR4/air matrix which increases ϵ in the direction of the wire.[19] Because we only need to control ϵ_{zz} to fully implement our transformation, wires aligned out of the plane of the transformation are sufficient. Each split wire unit cell consisted of copper strips of varying length from zero to 3.03mm patterned onto 200μm thick FR4 sheets. The width and pitch pitch of the wires was 300μm and 600μm, respectively. However,

this unit cell alone cannot achieve the lowest indexes required by the design. To reach permittivities below that afforded by the volume filling fraction of the FR4 alone, a second air-void unit cell was introduced. This unit cell consisted of a 300μm wide slot cut through the FR4 substrate. Varying the length of this unit cell from zero to 3.03mm varies the volume fraction of FR4 in the unit cell and allows the permittivity to be smoothly reduced to nearly one. Stacking sheets adjacent unit cells with a spacing of 1.5mm formed a three dimensional array of copper wires and air slots aligned in the z-direction. The geometry of the unit cell put an upper limit on ϵ_{zz}, and hence the arc length of lens that could be flattened.

The lens was characterized in a parallel plate 2D mapper, as has previously been described.[71] Such a parallel plate implementation constrains the polarization to be TE, as required by our design, and allows for the field magnitude and phase inside the lens to be imaged. The maximum ϵ_{zz} that can be attained with our split wire unit cell determines the degree of flattening, i.e. the length of the focal planes, that can be achieved. In this case our maximum ϵ was 6, corresponding to a flattening of 28% of the radius on either side of the lens or a flattened focal surface of arc length $1.54 radius$ or 88^o. The actual lens was designed to operate in the X-band from 8GHz to 12GHz. To create the lens permittivity profile, the length of each wire/void was varied according to its position in the lens permittivity profile by interpolating the permittivity retrieved from simulations of the unit cells with varying length wires/voids.[73] To emulate infinite extent in the direction out of the plane of the transformation, a slice of the lens three unit cells thick was placed in a parallel plate waveguide. This constrains the polarization to be TE. Thus all fields and material properties are invariant in the z-direction. The source was a dielectric rod waveguide placed at various positions on the object plane of the lens. The field inside the lens was imaged for sources from 8GHz to 12GHz and for five source positions spanning the flattened boundary of the lens. The imaging of the lens was equally effective for

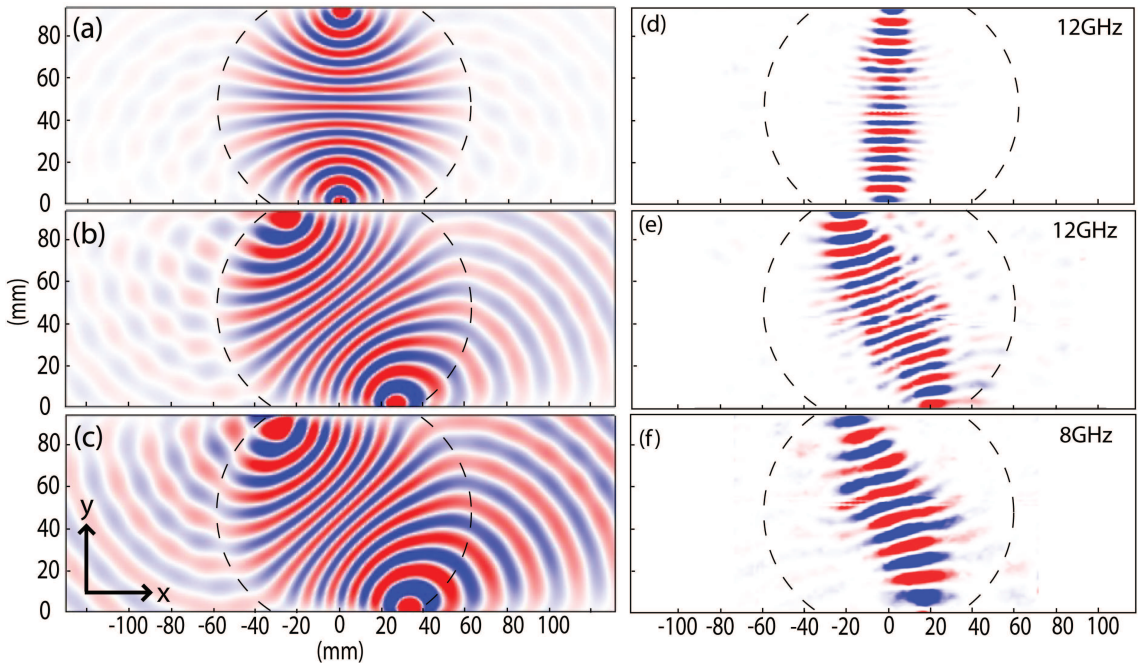

FIGURE 2.14: (a),(b), and (c) Show full-wave finite element simulation results for the truncated, ϵ'_{zz}, permittivity distribution. a) shows the source located at the center of the lens, b) shows the source located just inside the truncation, and c) shows the source located in the truncated region, but still on the boundary of the transformed lens. This qualitatively shows the effect of truncating the index profile as the source in c) is poorly focused through the lens with much of its energy being radiated away. Figures (d),(e), and (f) Show the experimentally measured electric field in the transformed Maxwell lens. (d) shows the field for the source located at the center of the flattened lens boundary. (e) and (f) show the source located at the edge of the flattened boundary at 12GHz and 8Ghz, respectively. In all cases the source is located at the lower boundary.

all source positions and frequencies, as shown in Fig. 2.14.

This type of QCTO device requires dielectric-only gradient index materials. Although an approximation step has been used to achieve more robust and broadband performance, the effect of truncating index values below unity appears to have little effect on the device operation as long as the regions having index less than one are marginal. Such dielectric-only TO devices are readily scalable to optical wavelengths. The observed transmission losses can be reduced by using a low-loss substrate and/or

impedance matching a detector array on the image plane to the lens. This type of 2D optical device is ideally suited to implementation in guided wave devices such as silicon-on-insulator waveguides where the effective index of the waveguide can be controlled by making holes/columns in the silicon or by tapering its thickness.[12, 13] A three dimensional version of this relay lens could be approximated by revolving this 2D index profile around the optical axis to create an inhomogeneous isotropic index profile, or by using a true three dimensional transformation which would require anisotropic material parameters.

2.6 Microwave transformation-optical Rotman lens

The lenses discussed in Sections 2.1,2.3,2.4, and 2.5 were all bulk-dielectric lenses where light incident on the surface of the lens from free-space enters the lens, propagates within the dielectric of the lens, and exits the lens into free-space through the second lens boundary. However, as mentioned in 2.5, a lens is generally a device that transforms light from one place to another - the exact means of how this transformation happens is somewhat irrelevant to the lensing behavior. An example of this abstraction is the so called Rotman lens which uses antennas that couples light in and out of the lens and transmission lines that guide light around within the lens itself. Even for this type of lens, metamaterials find utility in improving the performance of the lens. The work in this section was published by Hunt *et al.* in [74].

The solutions to the Rotman lens design equations constrain the minimum size of the device. Here we use Transformation Optics (TO) to compress a standard Rotman lens by 27 percent along the optical axis while maintaining the beam steering range, gain, and side lobe amplitudes over a broad frequency range. This kind of transformation requires an anisotropic magnetic response, which is achieved using complementary electric dipole metamaterials. These metamaterials are ideal for

transmission line applications and exhibit broadband magnetic response.

Recently there has been increasing interest in broad band beam-steering microwave lenses for imaging and communication. The Rotman lens is commonly used in such lensing applications since its transmission line based structure makes it low profile and easy to fabricate.[75, 76, 77, 78] The Rotman lens consists of a parallel plate transmission line with a set of input ports and a set of output ports. Each output port then has a microstrip transmission line of some electrical length that feeds an antenna. The relative positions of the input and output ports and the electrical length of each antenna feed are determined by the Rotman lens equations. The solution of these equations is such that when a single input feed is excited, the phase distribution across the antennas is that of a plane wave traveling in a direction determined by the position of the excited port.[75] In order to emulate a reflectionless open boundary, the parallel plate region between the input and output ports is terminated with impedance matched dummy ports. The positions of these dummy ports is not prescribed by the Rotman lens equations and choosing these in a manner that reduces reflections back into the lens is a major optimization factor in the design of the lens.[79, 76]

For many applications it is desirable to reduce the size of the lens in the in-plane directions. Here we aim to achieve this by applying the techniques of Transformation Optics (TO) and metamaterials. TO provides a method to transform the geometry of an optical device while maintaining its optical properties by varying the material parameters of the transformed device.[80] The required permittivity and permeability of the transformed device are generally spatially varying and anisotropic. Metamaterials provide the means to implement these complicated material parameters. Previous work has used spatial variations in the isotropic index of refraction of the substrate material inside a Rotman lens to reduce the energy lost to the absorbing dummy ports.[81, 82] However, our TO design requires an anisotropic material re-

sponse. Furthermore, previous Rotman designs employing gradient index materials have used multiple fabrication steps to create the index gradients in the substrate material of the transmission line structures. Here we have used complementary electric dipole metamaterials, which can be fabricated in the same step as the Rotman transmission line structure itself, to achieve an anisotropic index of refraction. The use of complementary metamaterials requires only a single layer circuit board.

Transformation Optics has been used to create entirely novel devices such as cloaks and to modify or improve the operation of existing optical devices.[83, 10, 63, 13, 12, 19] However, TO can also be used to decrease the size of an optical device by applying a coordinate transformation that compresses the space in which the optical device is embedded.[80] A transformation is chosen that distorts virtual space, described by unprimed coordinates $(x, y, z) = (x_1, x_2, x_3)$, into the desired physical space, described by primed coordinates $(x', y', z') = (x'_1, x'_2, x'_3)$. Physical space represents the actual location and geometry of the device when implemented, while light will behave as though it is in the virtual space. A transformation can be implemented by varying the permittivity and permeability in the physical space using Eqns. 2.2 and 2.3.

In general this results in spatial variations in both the permeability and permittivity of a device and results in anisotropic material parameters. However, in the short wavelength limit where the spatial variations in the material parameters are small over the length scale of a wavelength, the ray optics approximation becomes valid and only the index of refraction is important. Thus an eikonal approximation can be made where only the index of refraction prescribed by the transformation is maintained and the impedance is ignored.[80] For example, for transverse electric (TE) polarization and propagation in the plane perpendicular to the z-axis, the relevant indices are

$$n_x = \sqrt{\mu_y \epsilon_z}$$
$$n_y = \sqrt{\mu_x \epsilon_z}. \tag{2.9}$$

We can then define

$$\epsilon_z' = 1$$
$$\mu_y' = \mu_y \epsilon_z$$
$$\mu_x' = \mu_x \epsilon_z \tag{2.10}$$

such that the indices are maintained but only the permeability in the plane of propagation must be controlled. This is the case relevant to a Rotman lens because propagation in the parallel plate region of the lens is TE and in the plane. It is important to note that even when ray optics is valid, the Fresnel reflection coefficients will change and scattering at the boundaries of the transformed region, which does not occur if the full transformation material parameters are implemented, may occur. This is because the eikonal approximation does not maintain the correct impedance.

To reduce the overall size of the Rotman lens, we transform the space within the parallel plate region of the Rotman lens. This transformation is contained entirely within the boundaries of the lens so that the input and output contours are the same as obtained from the Rotman lens equations but shifted towards one another by an amount determined by the transformation.

The transformation implemented here was a parabolic transformation that compresses space along the optical axis (x-axis) of the Rotman lens in such a manner that the material parameters go to free space at the boundaries of the transformed region. This transformation is given by

$$\frac{dx'}{dx}(x) = \begin{cases} (1-\alpha)\left(\frac{2x-l_1-l_2}{l_1-l_2}\right)^2 + \alpha & , \ l_1 < x < l_2 \\ 1 & , \ x \leqslant l_1 \cup x \geqslant l_2 \end{cases} \tag{2.11}$$

where $\alpha \in [0,1]$ is a free parameter that controls the degree of compression. l_1 and l_2 are the boundaries of the transformation in untransformed space. The degree of compression is constrained by the realizable material parameters, with larger compressions requiring larger material parameters.

This expression can be integrated to determine the coordinate map,

$$x'(x) = \begin{cases} \frac{(1-\alpha)}{6(l_1-l_2)^2}(2x-l_1-l_2)^3 + \alpha x + c & , \ l_1 < x < l_2 \\ l_1' + (x-l_1) & , \ x \leqslant l_1 \\ l_2' + (x-l_2) & , \ x \geqslant l_2 \end{cases} \tag{2.12}$$

where c is a constant that determines the translation of the transformed region. This transformation and the transformed Rotman lens outline are shown in Fig. 2.15.

This transformation requires results in $\epsilon_z(x) = \mu_y(x) = 1/\mu_x(x)$. In order to simplify the fabrication of this lens, an eikonal approximation of the form given in Eqn. 2.10 is used. The approximated material parameters are then, $\epsilon_z' = \mu_x' = 1, \mu_y' = \mu_y^2$,. This means that only the permeability in the y-direction, perpendicular to the optical axis and in the plane of the parallel plates, needs to be controlled. In most material systems, controlling the permeability is very difficult, especially if broad-band and low-loss is desired. Here we avoid these problems by taking advantage of the transmission line geometry of the Rotman lens and use complementary metamaterials to achieve the needed permeability.

Complementary metamaterials (discussed in detail in 4) are planar metamaterials or metasurfaces, where the metal and dielectric comprising the material unit cell have been exchanged as compared to bulk metamaterials. For instance, the unit cell

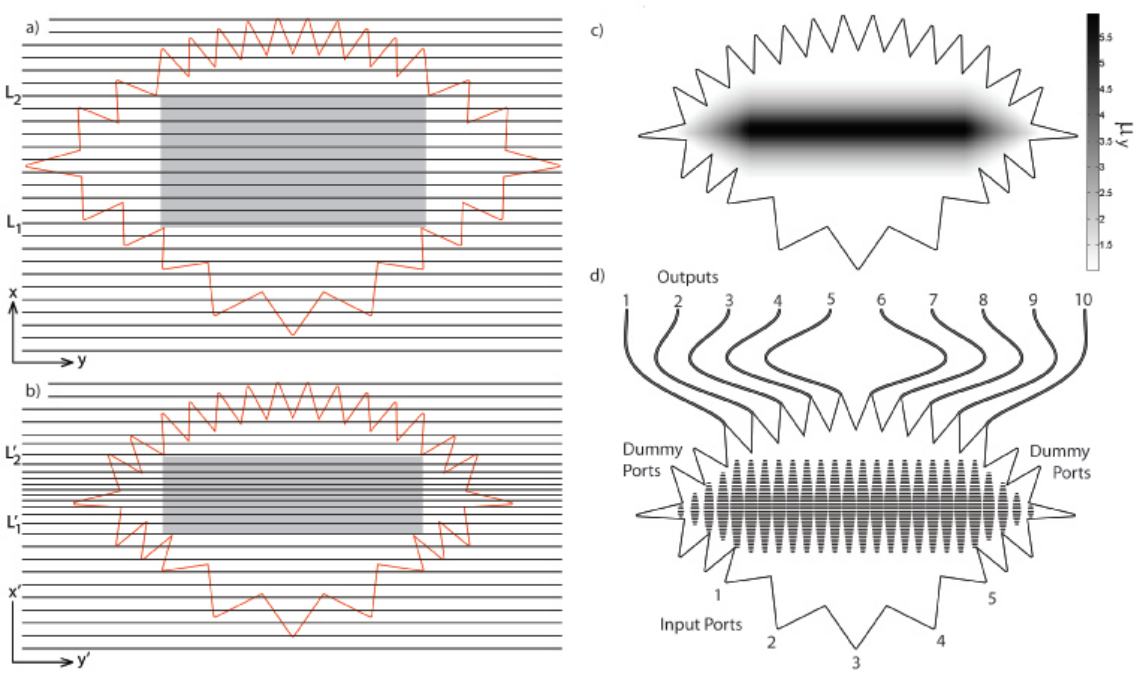

FIGURE 2.15: The a) untransformed and b) transformed Rotman lens outlines. In a) and b) lines of constant x are shown and the transformation region is shaded. The transformed region is limited in the y-direction to a rectangle entirely within the boundary of the lens, resulting in the observed change in the dummy port geometry. c) The permeability in the y-direction prescribed by the transformation. d) The fabricated lens outline with output transmission lines and C-dipoles corresponding to the permeability distribution in c).

for a complementary electric dipole (C-Dipole) is a slot cut into a metal sheet, as seen in Fig. 2.16. By the Babinet principal, these structures exhibit the dual material response to their bulk counterparts.[84] So the C-dipole gives rise to a magnetic response, allowing for the control of permeability. Furthermore, the magnetic response may be broadband, anisotropic, and low-loss. Since complementary metamaterials are planar, they cannot be used as bulk materials. However, when patterned onto a transmission line device, an effective loading is obtained. Among other devices, this effective loading has previously been used to implement a transmission line gradient index lens.[85] Fig. 2.16 shows the effective permeability, retrieved from

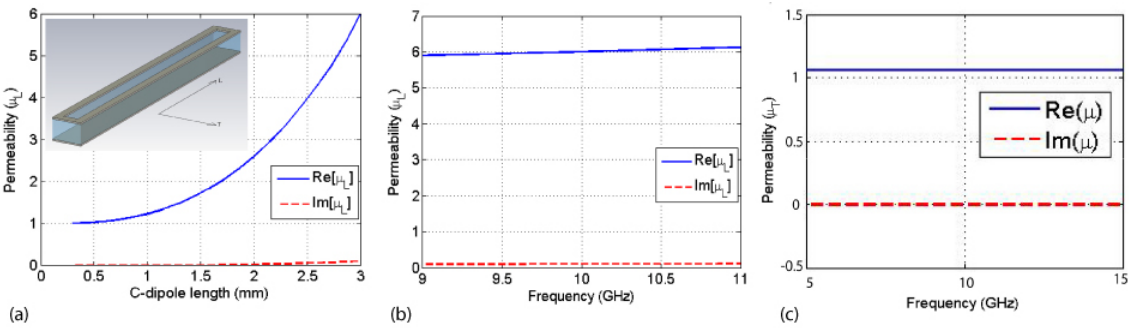

FIGURE 2.16: a,inset) The unitcell for a complementary dipole patterned on a parallel plate transmission line. The unitcell used in the fabricated lens was 300μm wide patterned in 17μm thick copper on a 200μm FR4 substrate. a,plot) The real and imaginary retrieved permeability for a $10GHz$ TE wave traveling perpendicular to the long dimension the C-Dipole. b) The retrieved permeability versus frequency for a 3mm long C-dipole. c) The retrieved permeability versus frequency for the same C-dipole and a wave traveling in the longitudinal direction.

simulations, of the C-dipole structure used in the fabricated lens. The permittivity for all frequencies and propagation directions is equal to the substrate permittivity. The maximum achievable permeability is limited by the maximum length of the of the C-dipole, which is in turn constrained by the operating wavelength such that an effective medium approximation is valid, and by the minimum fabricatable feature size. Increasing the C-dipole area density will increase the maximum permeability.

The eikonal approximation is useful because it simplifies the material parameters and the device fabrication. It does however introduce reflections that would be nonexistent if the full material parameters were implemented. By choosing a transformation for which the gradient smoothly goes to one at the boundaries of the transformed region, in this case a parabolic transformation, these reflections are minimized but are not absent. Furthermore, the transformation must be truncated at some point in the y-direction. Since the transformation cannot extend into the dummy ports themselves, there would be an impedance mismatch causing reflections if it was simply truncated at the ports. An additional problem with extending the

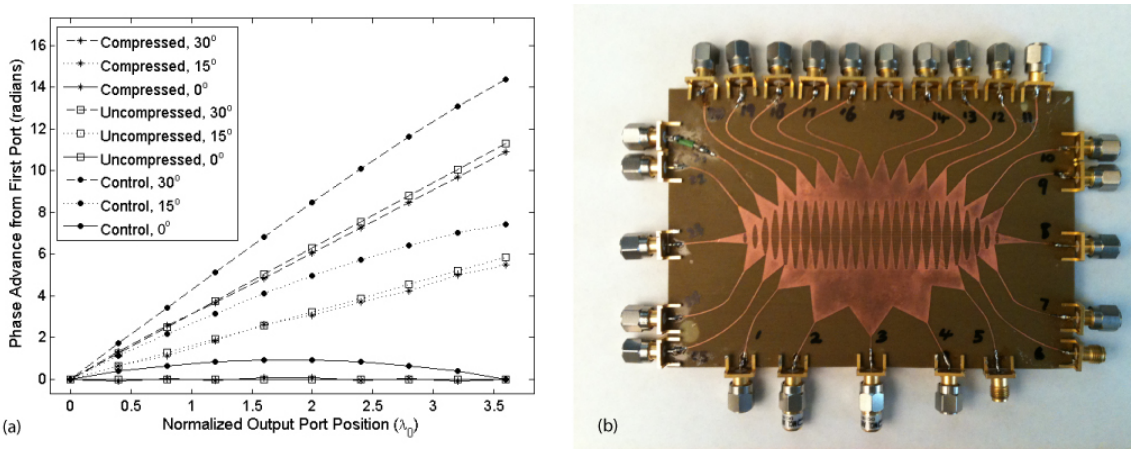

FIGURE 2.17: Phase distributions across the output antennas for three nominal focusing directions, for the uncompressed, compressed, and control lenses.

transformation to the boundaries of the parallel plate region is that the retrieved properties of the C-dipoles are only correct when the C-dipoles are embedded in a parallel plate, which is an approximation that breaks down at the lens edges. Thus we choose to end the transformed region at the point where it intersects with the lens boundary. To minimize reflections from this truncation boundary, the permeability is linearly graded in the y-direction from the value at the boundary of the transformation to one. This does not correspond to a true transformation of the field in these regions, and the phase entering the dummy ports is modified as compared to the untransformed lens.

The uncompressed lens was designed for 10GHz operation using the Rotman lens equations with five input ports and ten output ports. The nominal focusing directions for the ports were $-30^o, -15^o, 0^o, 15^o$, and 30^o. The dummy port positions were determined by placing them along the lines tangent to the extremes of the input and output contours. The compressed lens was then obtained from this design by shifting the input and output boundaries toward each other according to Eqn. 2.12, where α was chosen such that our maximum required permeability was equal to our

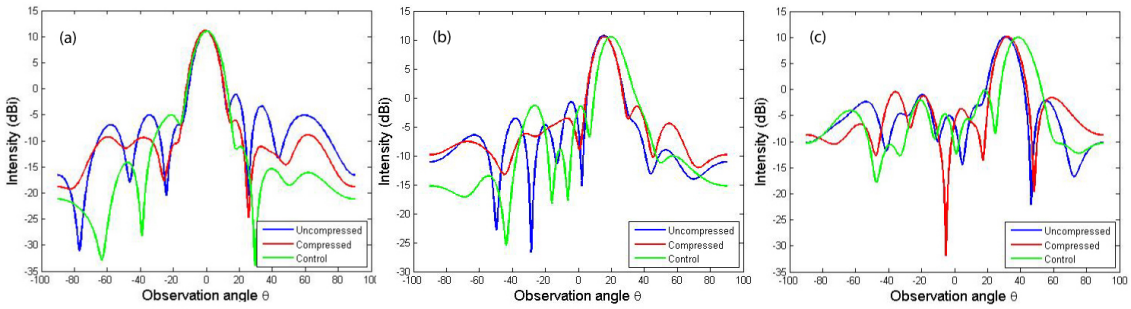

FIGURE 2.18: (a)The far field radiation pattern for the compressed, uncompressed and control Rotman lens.

maximum achievable. This shift of the boundaries corresponded to a 27% decrease in the length of the Rotman lens along the optical axis. The dummy port positions for the transformed lens were determined in the same manner as for the untransformed lens. The region between l_1 and l_2 was then patterned with C-dipoles to achieve the anisotropic index prescribed from Eqn. 2.11 and Eqn. 2.10 by interpolating Fig. 2.16 for the necessary length of the C-dipole. A control lens was also designed such that the boundaries of the lens were identical to the compressed lens but the material parameters required to implement the transformation were omitted.

Fig. 2.17 shows the analytical phase distribution across the output ports for the uncompressed, compressed and control lens. While the ideal phase distribution is not exactly preserved through the transformation, it is much closer to the ideal phase distribution than the control phase distribution. The control lens shows a shift in the phase slope, which corresponds to a shift in the propagation direction, as well as a deviation from linearity, which corresponds to defocusing of the beam.

The uncompressed, compressed, and control lenses were fabricated on 0.2mm FR4 using standard circuit board fabrication techniques. An Agilent network analyzer was used to measure the multi-port scattering matrix from which the output phase distribution, far-field pattern, and loss characteristics were calculated.

As expected from the analytic phase distributions, the control lens shows both a

Table 2.1: Transformation-optical Rotman lens performance. FWHM/($\theta_{actual} - \theta_{nominal}$) for each lens and for each nominal focusing direction

Focusing direction	$0^o_{nominal}$	$15^o_{nominal}$	$30^o_{nominal}$
Uncompressed	$17^o/0^o$	$17^o/0^o$	$17^o/0^o$
Compressed	$17^o/0^o$	$17^o/0^o$	$17^o/0^o$
Control	$19^o/0^o$	$20^o/5^o$	$20^o/10^o$

wider beam and a divergence from the nominal focusing direction. The transformed lens, on the other hand, preserves the width and direction of the uncompressed beam, though some mismatch in the side lobes is seen. The beam full-width-at-half-max (FWHM) for the uncompressed and compressed lenses is 17^o_{FWHM} for all nominal focusing directions while the control lens FWHM is 19^o_{FWHM} for the 0^o nominal focusing direction and 20^o_{FWHM} for the 15^o and 30^o nominal focusing directions. While the true focusing directions for uncompressed and compressed lenses are exactly equal to the nominal directions, the control lens shows deviation with increasing nominal direction. The deviation from the nominal focusing direction for the control lens is 0^o, 5^o, and 10^o for the 0^o, 15^o, and 30^o nominal directions, respectively. This is summarized in Table 2.1. The variation in the side lobes is caused by reflections at the boundaries of the transformation region due to the eikonal approximation and truncation of the transformation in the y-direction. The transformed lens shows an average insertion loss of 1.448dB, which is contributed to a lower average return loss of 5.674dB for the transformed lens as compared to 6.484dB for the untransformed lens, as well as the loss of the C-dipoles. The increased return loss is due to reflections introduced by the eikonal approximation.

In this section we have shown the first ever example of a transformation-optical device implemented with complementary metamaterials. This was achieved by leveraging the unique anisotropic, broadband and low loss nature of the C-dipole to control the effective permeability inside a parallel-plate transmission line. The transformed

Rotman shows performance nearly identical to the untransformed lens 1.44dB insertion loss while being compressed along the optical axis by 27%. The degree of compression could be increased by using a lithography that supports smaller features so that a higher C-dipole density, and hence permeability, can be achieved. These complementary metamaterials require no additional cost or processing beyond that required to fabricate the untransformed Rotman lens. Such metamaterials could be used in non-TO devices as well, for example to provide index gradients to steer power away from the dummy ports to reduce the insertion loss and to correct the abberations seen at the off-focus ports.[81]

2.7 Negative index of refraction lens: the superlens

No discussion of metamaterial lenses could be complete without mentioning the negative index of refraction superlens. Though the author has not been involved in research into negative index lenses, a brief description of them is given here for completeness.

The first metamaterial to capture the imagination of the the general public was a piece of metamaterial with a negative index of refraction.[86, 71] At the interface between air and a material with negative index of refraction, rays of light to the 'wrong' side of the surface normal. Inside a negative index material phase fronts propagate 'backward' i.e. opposite to the direction of power transfer. These behaviors are unusual and exciting, but the truly fantastic power of such a material is in their ability to focus the evanescent fields of light. In the seminal paper on negative index materials published in 1968, Veselago noted that a flat slab of such material will focus light like a lens.[87] Then in 2000, shortly after the first negative index of refraction material was experimentally demonstrated by Smith et al., Pendry pointed out that a negative index slab would not only focus light, but it would also capture and focus evanescent waves - which normally do not propagate far enough away from

a scene to contribute to the focused image - resulting in a 'perfect' image of the scene.

As discussed in more detail in section 3.4, when light scatters off a scene, the sub-wavelength structure in the scene - structure with spatial frequencies, k_x, larger than the free-space wavenumber, k_0 - scatters into plane wave components with imaginary wavenumbers. I.e. if the optical axis is along z, these plane waves propagate along z with $k_z = \sqrt{k_0^2 - k_x^2} = i|k_z|$ when $k_x > k_0$. These 'evanescent' plane waves attenuate as $e^{-i(i|k_z|z)} = e^{-|k_z|z}$ and do not contribute to the image. However, when these waves enter a material with negative index of refraction, $-|n|$, the evanescent wave are amplifed with propagation along z as $e^{+|n||k_z|z}$! This means that after propagating from a scene through a distance d of air, then a distance $2d$ of a negative index slab, and then another distance d through air, all the plane waves, including the evanescent ones, will be have exactly the same amplitude they had at the scene. The resulting image will include information about structure in the scene below the diffraction limit yielding a super-resolution image. Thus the negative index of refraction lens is also called a superlens.

In practice, the inherent losses involved in making a material with negative index of refraction prevents the image from having infinite resolution, but many demonstrations of superlenses have indeed beaten the diffraction limit. Super lenses have been demonstrated from RF[88], to optical[23], and even ultraviolet[89].

2.8 Conclusions

Metamaterials enable many novel types of lenses. In this chapter we have demonstrated how the design flexibility of metamaterials makes them useful in creating lenses with unprecedented form-factors and performance. In the following chapters we will describe how these different types of lenses can be used for imaging, and present an entirely new type of imaging system enabled by the unique properties of metamaterials.

3

Theory of Metamaterial Imaging Apertures

In Chapter 2 we discussed several different types of metamaterial lenses and imaging systems. Some of the systems discussed look quite different from what many people would consider a lens, however they all share the ability to transform light from one location to another. For imaging, this ability is used to transform the light emitted, or scattered, from a scene of interest to a detector of some type, with the objective of determining properties of the scene. Typically these properties are spatial and spectral information about the scene. Despite the vast differences in implementation of the lenses we have presented, they all share this common behavior. Understanding this general perspective on imaging is the goal of the field of computational imaging. Before we may understand the more abstract metamaterial imaging systems discussed in this thesis, we must first become familiar with the mathematics and terminology of computational imaging. The following chapter provides general concepts and terminology that will be referenced throughout the rest of this document.

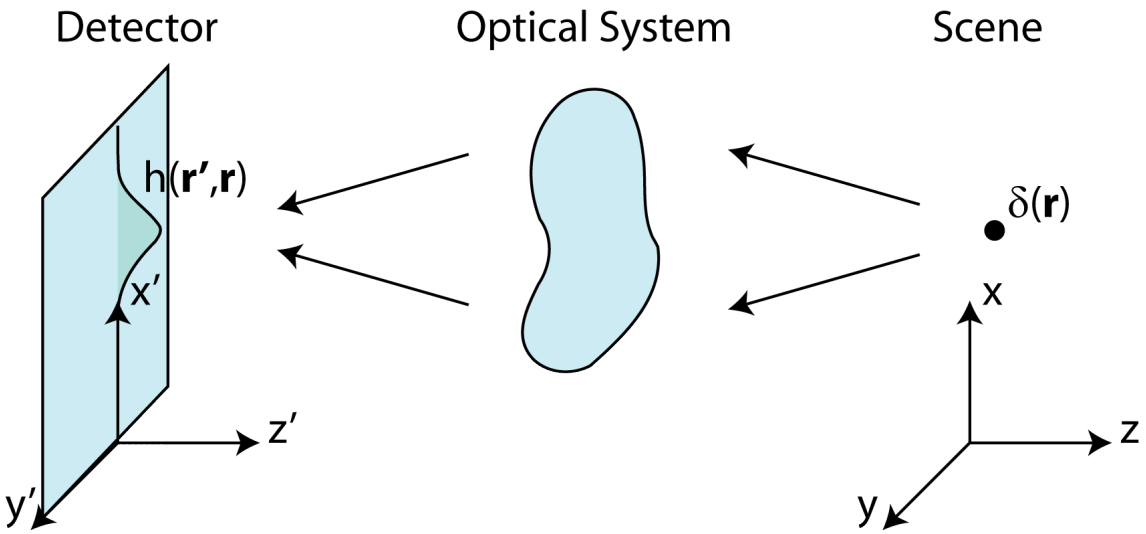

FIGURE 3.1: Schematic representation of a general imaging system.

3.1 Computational imaging

The information presented in this section is largely credited to D. Bradys book Optical Imaging and Spectroscopy[90]. The process of imaging can be thought of as a general signal transmission problem. The signal to be sent is information about the objects in the scene and the transmission channel is the optical imaging system - including light scattering, propagation, and detection. This is depicted in Fig. 3.1. In Fig. 3.1, the impulse response, or point spread function (PSF), of the optical system is given by $h(r', r)$. Then the measured noisy signal at the detector from a scene, defined as the scalar function $f(r)$ which represents some spatially varying property of the scene that we aim to measure, is given by,

$$g(r') = \int_{scene} f(r)h(r', r)dV + n(r') \tag{3.1}$$

where $n(r)$ is a noise term.

Often for imaging systems, measurements are made by spatially separated detectors such as pixels, but almost any physical parameter may be used to index or

multiplex the measurements. For a pixel-type detector space is used to index the measurements, but time, frequency, temperature or any other property that causes the PSF of the system to change may be used to index the measurement modes. For the imaging system presented in chapter 7 frequency is used to index the measurements

3.1.1 Discretization of the imaging equation

Lets call the general mode indexing variable w. Usually we make M discrete measurements for different values of w, such as for different discrete pixel-detectors separated in space, a single measurement made for the m^{th} value of w is given by,

$$g(w_m) = \int_{detector} g(w)p(w_m - w)dV + n(w_m) \tag{3.2}$$

where $p(w)$ is the detector response function. From here on, *we assume that the detector response is perfectly selective in* w and is so a Delta function. With this assumption, and implicitly representing the w mode-indexing variable with a subscript m, the m^{th} measurement is,

$$g_m = \int_{scene} f(r)h_m(r)dV + n_m \tag{3.3}$$

It is possible to discretize the integral over the scene volume in under the condition that the scene function is limited in both space and frequency. For the moment, lets consider a one-dimensional (1D) scene function $f(x)$. Given some basis of functions, $\{\phi(x,k), k \in R\}$, which are orthonormal,

$$\int_{-\infty}^{\infty} \phi(x,\alpha) \cdot \phi(x,\beta)dx = \begin{cases} 0 & \alpha \neq \beta \\ 1 & \alpha = \beta \end{cases} \tag{3.4}$$

$f(x)$ can be represented on as,

$$f(x) = \int_{-\infty}^{\infty} a(k)\phi(x,k)dk \tag{3.5}$$

provided that the basis spans the support of $f(x)$. The basis-coefficients $a(k)$ are given by projecting the scene function onto each basis function,

$$a(k) = \int_{-\infty}^{\infty} f(x)\phi(x,k)dx \tag{3.6}$$

For example, a commonly used basis is the Fourier basis, $\left\{e^{-ikx}, k \in \mathbb{C}\right\}$.

The Whittaker-Shannon sampling theorem says that if $f(x)$ has no spatial frequencies, u, larger than B - i.e. the Fourier transform, $\hat{f}(u)$, of $f(x)$ is zero beyond some maximum frequency,

$$\hat{f}(u) = 0 \text{ for } |u| > B \tag{3.7}$$

then $f(x)$is bandwidth-limited and can be represented with the discrete summation,

$$f(x) = \sum_{n=-\infty}^{\infty} a_n sinc(2Bx - n) \tag{3.8}$$

The fantastic thing about the Shannon-basis, the basis composed of shifted sinc functions, $\{sinc(2Bx - n), n \in \mathbb{Z}\}$, is that the basis-coefficients are simply samples of $f(x)$ taken with a period of $\Delta x = B/2$!

$$a_n = \int_{-\infty}^{\infty} f(x)sinc(2Bx - n)dx = f(n/2B_x) \tag{3.9}$$

This is an important and powerful observation. It means that the complete, smooth, band-limited function can be formed simply by knowledge of the functions value at discrete points. This is much easier both mathematically and physically than integrating the full function times the basis functions over all space to get the basis coefficients. Henceforth, if we refer to the 'canonical basis' we are referring to the Shannon-basis. The smooth function can then be exactly reconstructed using these discrete measurements and Eqn. 3.8, which is sometimes called the Shannon-interpolation formula.

For simplicity, and because most displays have some maximum resolution due to display pixel size, we often represent $f(x)$ on the Haar basis, $\left\{\frac{1}{\Delta x} rect\left((x - n\Delta x)/\Delta x\right), n \in \mathbb{Z}\right\}$ which is an approximation of the Shannon/sinc basis. This basis does not completely span the support of $f(x)$, but has the advantage that it is easier to compute this approximate $f(x)$ from the basis-coefficients since the Haar basis functions do not overlap and are finite in extent, while sinc functions are infinite in extent. This is the pixel basis where every rectangular pixel in an image of the scene is assigned a constant value.

Now if $f(x)$ is limited in spatial extent, i.e.

$$f(x) = 0 \text{ for } |x| > X \tag{3.10}$$

then the number of samples of $f(x)$ needed to exactly represent is,

$$X/\Delta x = 2BX \tag{3.11}$$

or in three dimensions, $8B_xXB_yYB_zZ$.

This total number of basis-coefficients, N, is known as the space-bandwidth-product (SBP) of $f(x)$. This will be the maximum number of basis-coefficients needed to represent any function with the same bandwidth and extent with any other orthogonal basis[91]. The function $f(x)$ can then be exactly represented by the finite-length vector of basis-coefficients $\mathbf{f} = [a_0, a_1, a_2, \ldots, a_N]$.

Of course, no real-world scenes will be bandwidth- or extent-limited. However any imaging system will have some maximum field-of-view (FOV), and some minimum resolution (maximum spatial bandwidth). Thus we can define the SBP to be a property of the imaging system itself, and then the best image we can obtain with the system is limited to a low-pass filtered and spatially-truncated approximation of the true scene, as discussed in section 3.4.

Thus if $f(r)$ is bandwidth and extent limited, it can be represented on an orthonormal basis as $f(r) = \sum_{n=0}^{N} a_n \phi_n(r)$ and the continuous measurement equation

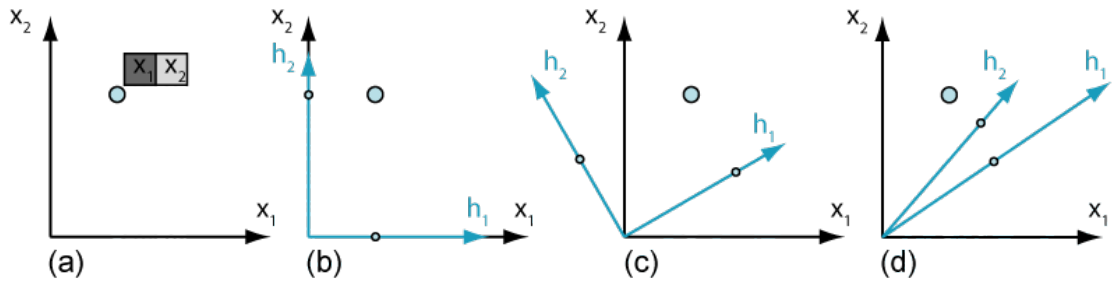

FIGURE 3.2: A discretized scene vector consisting of N pixels can be represented as a point in N-dimensional space. Likewise the measurement modes can be represented as vectors in the same space. Then the measurement process can be envisioned as projecting the scene vector onto the measurement vectors. In (b) the measurement modes are the individual pixels themselves, and the measured values can be immediately interpreted as the reconstructed image since $H = I$. The measurement modes may be any linear combination of the pixels (c), and do not need to be orthonormal (d). As long as the measurement modes span the N space, the scene may be recovered. However, when noise is added to the measurements the importance of orthonormal measurement modes becomes apparent - inverting the measurement matrix will amplify the noise associated with smaller measurement modes, and for modes with small inner product.

(Eqn. 3.3) above can now be discretized as,

$$g_m = \int_{scene} f(r)h_m(r)dV + n_m = \int_{scene} \sum_n^N a_n \phi_n(r) h_m(r) dV + n_m \tag{3.12}$$

or

$$g_m = \sum_n a_n \int_{scene} \phi_n(r)h_m(r)dV + n_m = [h_{m1}, h_{m2}, \ldots, h_{mn}, \ldots, h_{mN}] \cdot \mathbf{f} + n_m \tag{3.13}$$

and the complete set of measurements can be expressed as,

$$\mathbf{g} = \mathbf{H}\mathbf{f} + \mathbf{n} \tag{3.14}$$

where $\mathbf{f}$ is a length N vector of basis-coefficients representing the scene, $\mathbf{g}$ is a length M vector of measurements made at the detector, $\mathbf{n}$ is a length M vector of measure-

ment noise, and $\mathbf{H}$ is a $M \times N$ matrix with elements,

$$h_{mn} = \int_{scene} h_m(r)\phi_n(r)dV \tag{3.15}$$

If we choose the $\phi_n(r)$ to be the Shannon-basis, then the entries of $\mathbf{H}$ become simply the values of the point-spread functions h_m at Nyquist-sampled points in space, r_n,

$$h_{mn} = h_m(r_n) \tag{3.16}$$

The columns of the measurement matrix, are the discretized point spread functions (PSFs) describing how light from every point in the scene contributes to every measurement. Conversely, the rows of the measurement matrix are the measurement modes. Each measurement $g_m = [h_{m1}, h_{m2}, \ldots, h_{mN}] \cdot \mathbf{f} + \mathbf{n}$ can be thought of as the projection of the scene onto one of the measurement modes of the imaging system. This is visualized geometrically in Fig. 3.2.

In a conventional imaging system, the measurement modes might be diffraction-limited spots, each of which samples a small portion of the scene (Fig. 1.1A). Because these modes have little or no spatial overlap in the detector plane, they can be acquired nearly independently and simultaneously with N detectors, such as a charge-coupled device (CCD) array. But in general the measurement modes need not be indexed by spatially independent detectors. The measurement modes may be generated and measured sequentially by reconfiguring the measurement system. This sequential measurement mode formation is the basis for single-pixel imaging systems. Any method that provides measurements that can be obtained independently can be used to index the measurement modes this is where the ability of metamaterials to independently control different properties of light comes plays an important role, as will be discussed in more detail in chapters 6 and 7. The information presented in this section is largely credited to D. Bradys book Optical Imaging and Spectroscopy[90].

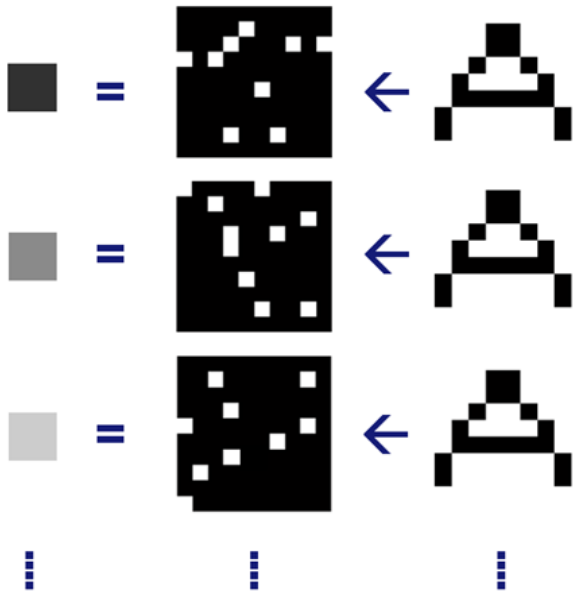

FIGURE 3.3: A graphical representation of the imaging process corresponding to Fig. 1.1B. The scene (the letter A) is imaged with a lens onto a series of random masks that transmit a subset of all the image pixels. The mask is then imaged with a second lens onto a single detector. The value measured at the detector for each mask is the sum of the that mask times the scene. Each mask is one row of the measurement matrix.

3.1.2 Image reconstruction

So now the problem of imaging is that of inverting the equation $\mathbf{g} = \mathbf{Hf} + \mathbf{n}$ to obtain an estimate of $\mathbf{f}$, $\mathbf{f_e}$. This process is called scene reconstruction. If there is no noise and $\mathbf{H}$ is an invertible matrix, then this can be done by direct matrix inversion. In the presence of noise, or if $\mathbf{H}$ is ill-conditioned then direct inversion may fail to produce a suitable estimate of $\mathbf{f}$. If the singular value decomposition (SVD) of $\mathbf{H}$ is,

$$\mathbf{H} = \mathbf{USV}^* \tag{3.17}$$

where $\mathbf{U}$ is a $M \times M$ complex unitary matrix, $\mathbf{V}$ is an $N \times N$ complex unitary matrix, and $\mathbf{S}$ is a $M \times N$ rectangular diagonal matrix of real non-negative singular values, $\mathbf{S} = diag_{M\times N}(s_1, s_2, s_3, \ldots, s_r)$ such that $s_1 \geqslant s_2 \geqslant s_3 \geqslant \ldots \geqslant s_r$ and $r = min(M, N)$. The columns of $\mathbf{U}$ are the left-hand singular-vectors, $\mathbf{u}_m$, that span

the measurement space, and the columns of $\mathbf{V}$ are the right-hand singular-vectors, $\mathbf{v}_n$, that span the scene space. The ratio of the largest to the smallest non-zero singular values in $\mathbf{S}$ is the condition number of the matrix while the number of non-zero singular values in $\mathbf{S}$ is the rank of the matrix. The null-space of $\mathbf{H}$ is spanned by the last $N - M$ vectors in $\mathbf{H}$. The inverse of $\mathbf{H}$ is given by,

$$\mathbf{H}^{-1} = \mathbf{V}^{*-1}\mathbf{S}^{-1}\mathbf{U}^{-1} = \mathbf{V}\mathbf{S}^{-1}\mathbf{U}^{*} \tag{3.18}$$

which may be generalized for non-square $\mathbf{H}$ using the pseudo-inverse,

$$\mathbf{H}^{+} = \mathbf{V}\mathbf{S}^{+}\mathbf{U}^{*} \tag{3.19}$$

where + indicates the pseudo-inverse which for a diagonal matrix like $\mathbf{S}$ is obtained by simply inverting the non-zero diagonal elements and leaving all zero elements alone. The pseudo-inverse of a square and non-singular matrix is the normal inverse.

This explains why direct inversion of an ill-conditioned matrix (a matrix with large condition number) fails to provide an estimate of $\mathbf{f}$ in the presence of noise. If a measurement is corrupted by gaussian white noise with variance $Var(\mathbf{n}) = \sigma^2$ then using the pseudo-inverse of $\mathbf{H}$ to attempt to estimate $\mathbf{f}$ gives,

$$\mathbf{f_e} = \mathbf{H}^{+}\mathbf{g} = \mathbf{f} + \mathbf{V}\mathbf{S}^{+}\mathbf{U}^{*}\mathbf{n} = \mathbf{f} + \epsilon \tag{3.20}$$

The error in the estimate is $\epsilon = \mathbf{V}diag_{M\times N}(1/s_1, 1/s_2, 1/s_3, \ldots, 1/s_r)\mathbf{U}^{*}\mathbf{n}$ (unless some of the singular values are zero in which case their reciprocal in the pseudo-inverse of $\mathbf{S}$ is replaced by zero). Geometrically, the unitary matrices $\mathbf{U}^{*}$ and $\mathbf{V}$ correspond to magnitude-preserving rotations and $\mathbf{S}^{+} = diag(1/s_1, 1/s_2, 1/s_3, ..., 1/s_r)$ is a scaling. Since the noise distribution is white, the distribution can be represented as an n-sphere with radius σ^2 and the first rotation by $\mathbf{U}^{*}$ has no effect on the distribution. The scaling by $\mathbf{S}^{+}$ and subsequent rotation by $\mathbf{V}$ distorts the noise distribution by $1/s_i$ along the $\mathbf{v}_i$ singular-vector direction. Thus the error in the reconstruction

has more energy in the right-hand singular vector directions with smaller singular values. The energy of the reconstruction error is,

$$|\epsilon|^2 = \sigma^2 * \sum_i = 1^r 1/s_i^2 = \sigma^2 \Psi \tag{3.21}$$

So the reconstruction error has magnitude related to the sum of the inverse singular value spectrum squared, Ψ, and is primarily in the scene-spanning singular vectors with small singular values. For measurement matrices with large condition number the small singular values amplify the noise. Concave measurement matrices with large Ψ will do better than convex measurement matrices with low Ψ.

The estimation problem may be stated more generally as the convex optimization problem,

$$\mathbf{f_e} = argmin_{f_e} \|\mathbf{H}\mathbf{f_e} - \mathbf{g}\|_2^2 \tag{3.22}$$

We recognize this as an ordinary least-squares problem which, in the presence of white noise, has a solution given by,

$$\mathbf{f_e} = (\mathbf{H}'\mathbf{H})^{-1}\mathbf{H}^*\mathbf{g} = \mathbf{H}^+\mathbf{g} \tag{3.23}$$

The rank of $\mathbf{H}$, obtained from the SVD, provides a measure of the number of orthogonal modes that a given measurement matrix samples. If the rank is equal to the space-bandwidth-product, then the measurement matrix captures all the available information in the scene and achieves the maximum possible resolution. Thus the SVD of a measurement matrix provides a useful metric to characterize the corresponding imaging system, with the rank giving the best possible resolution of the system and the condition-number giving its robustness to noise. A useful metric the analyse a linear measurement system is the the effective-rank of the system's measurement matrix. This is the number of singular values higher than some noise power. The effective-rank estimates how many useful measurements are collected by

the system at a given SNR level and so gives a description of how a system responds to different noise levels.

3.1.3 Compressed sensing

To form a completely determined set of measurements (thus enabling a unique solution for $\mathbf{f}$), the rank of $\mathbf{H}$ must equal the scenes space-bandwidth-product[90]. This means that the number of measurements M must be greater than or equal to the space-bandwidth-product. If $M \leqslant N$, then the scene is underdetermined and there exist many possible scenes that would all produce the same measurements. Compressed sensing allows for the reconstruction ill-conditioned measurements where much of $\mathbf{f}$ lies in the null-space of the measurement matrix, or where the number of measurements M is much less than the space-bandwidth-product. This problem is visualized geometrically in Fig. 3.4. This is accomplished by using nonlinear estimators that attempt to solve the constrained-optimization problem,

$$\mathbf{f_e} = argmin_{f_e} \|\mathbf{H}\mathbf{f_e} - \mathbf{g}\|_2^2 + \lambda R(\mathbf{f_e}) \tag{3.24}$$

where we have added a constraint to the problem of 3.22. $R(\mathbf{x})$ represents a prior that measures some expected property of $\mathbf{x}$, e.g. smoothness or sparsity (number of non-zero basis-coefficients of $\mathbf{f}$). The first term in Eqn. 3.24 represents the l_2-norm corresponding to traditional least-squares estimation. An l_p-norm is a generalization of length measurement for a vector. The l_p-norm of a length N vector $\mathbf{x} = [x_1, x_2, \ldots, x_n, \ldots, x_N]$ existing in N-dimensional space is,

$$\|\mathbf{x}\|_p = \left(\sum_{n=1}^{N} |x_n|^p \right)^{\frac{1}{p}} \tag{3.25}$$

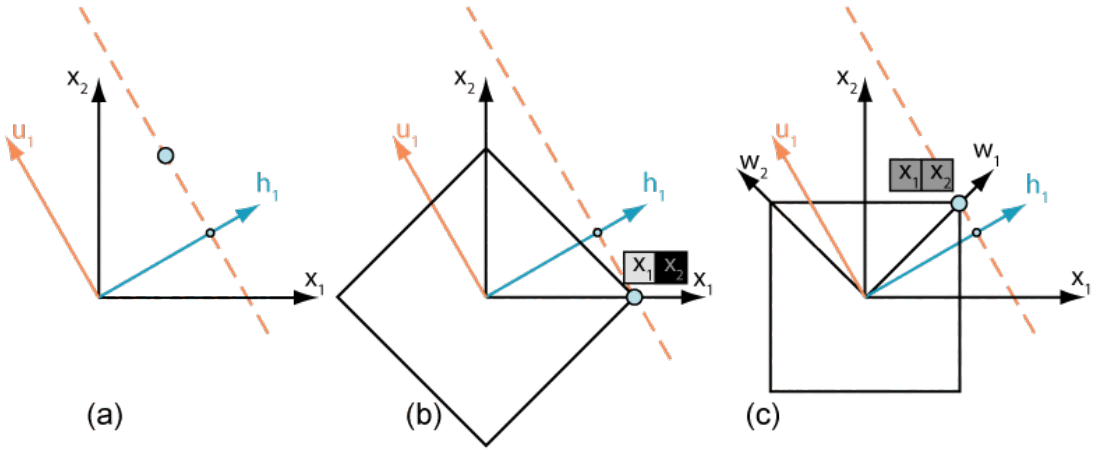

FIGURE 3.4: If the number of measurements, M, made is smaller than the dimension of the scene, N, (corresponding to the space-bandwith product), then the problem of estimating the scene from the measurements is underdetermined. In (a) we have a two-pixel scene, which is represented as the large blue dot in 2-dimensional space, and we make a single measurement of the scene by projecting it onto h_1. Our measurement matrix is simply the 1x2 matrix $H = h_1$. This measurement matrix has a null-space defined by u_1. In general, the null-space is an $(N - M)$-dimensional plane. With this one measurement we may only ever localize a scene along h_1; we can never know where the scene is along u_1. Given our measurement g_1, any scene $g_1 h_1 + \gamma u_1$ is a valid solution. Without additional information about our scene, we cannot pick a unique scene from that solution plane. If, however, we have the prior knowledge that our scene is sparse, we can select from the solution plane the solution with the smallest $\|l_1\|$ which is visualized as the point at which the smallest $\|l_1\|$ N-sphere contacts the solution plane. In (b) we have a scene which is sparse in the pixel-basis and, indeed, this is the point at which the smallest $\|l_1\|$ N-sphere (the black diamond) contacts the solution plane (dashed line). Because the $\|l_1\|$ N-sphere is 'pointy' it will contact the solution plane at one of its vertices with high probability, yielding a sparse solution if the vertices of the $\|l_1\|$ N-sphere are aligned with the sparsifying basis vectors. Knowing the basis in which a scene is sparse is equivalent to specifying the orientation of the $\|l_1\|$ N-sphere. In (c) the scene is sparse in a wavelet basis and the $\|l_1\|$ N-sphere oriented with the wavelet-basis vectors $[\mathbf{w}_1, \mathbf{w}_2]$ again contacts the solution plane at the true solution.

We find a few values of p particularity useful in computational imaging. The l_2-norm is then the Euclidean length of a vector.

$$\|\mathbf{x}\|_2 = \sqrt{\sum_{n=1}^{N} |x_n|^2} \tag{3.26}$$

If the vector represents a signal, the square of the l_2-norm is the signal power. The l_1-norm, sometimes called the taxi-cab length in analogy to distance measured between locations in a city measured in the number of city blocks required to drive between them, is the sum of the magnitudes of the elements of a vector.

$$\|\mathbf{x}\|_1 = \sum_{n=1}^{N} |x_n| \tag{3.27}$$

Taking the limit as p goes to zero we determine that the l_0-norm is the number of non-zero elements, regardless of their magnitude or sign, in a vector,

$$\|\mathbf{x}\|_1 = \sum_{n=1}^{N} \begin{cases} 1 & |x_n| > 0 \\ 0 & x_n = 0 \end{cases} \tag{3.28}$$

This is the 'sparsity' measure of the vector. Transforming a vector into a new basis is equivalent to rotating it. This preserves the l_2-norm of the vector (or the energy in a signal) however the other norms are not preserved through basis transformation. This means that a vector will have different sparsity when represented in different basis.

The scalar λ in Eqn. 3.24 is a weighting term that determines the relative importance of the data-matching term versus the prior-enforcing term. When $\lambda = 0$, the solution to this minimization optimization problem is traditional least-squares given by the pseudo-inverse of $\mathbf{H}$. In compressive sampling, $R(\mathbf{x})$ is the l_1-norm, which reflects the inherent sparsity that exists in natural scenes. Thus compressive

measurement leverages the realization that measurements need not conserve form of dimension in this sense[44, 92, 93]. The ability to estimate the scene, $\mathbf{f}$, from a substantially undersampled set of measurements is a result of the fact that natural images can be substantially compressed without excessive loss of image fidelity[94]. For the case of a sparse scene, this nonlinear minimization problem is rigorously solvable even with highly under-determined measurement datasets[43, 95, 96]. The power of using the l_1-norm as regularizer is that under certain conditions $\mathbf{f}_e = \mathbf{f}$ with overwhelming probability.4,5

Another regularizing function that is commonly used is total-variation (TV), which is the sum of the magnitudes of the gradients of an image[97]. For a two-dimensional image that is N_x pixels by N_y pixels the total-variation of the image is,

$$TV(\mathbf{f}) = \sum_{j=1}^{N_y-1} \sum_{i=1}^{N_x-1} |f_{j+1,i} - f_{j,i}| + |f_{j,i+1} - f_{j,i}| \tag{3.29}$$

As long as the chosen regularizer is a convex function (the line connecting any two points on the function never crosses the function, in which case there are no local minima) over the null-space of the measurement matrix, this optimization problem can be solved with a variety of numerically efficient approaches[98]. If the regularizer results in a non-convex objective function, then the finding the global minimizer may be computationally intractable. For example, the Iterated Soft Thresholding Algorithm[99, 100] finds the solution to this optimization problem with an l_1-norm regularizer by iterating the expression,

$$\mathbf{f}_{e,k+1} = soft\left(\mathbf{f}_{e,k} + \frac{1}{\alpha}\mathbf{H}^t(\mathbf{g} - \mathbf{H}\mathbf{f}_{e,k}), \lambda/2\alpha\right) \tag{3.30}$$

where $\alpha \geqslant maxeigenvalue(\mathbf{H}^t\mathbf{H}), \mathbf{f}_{e,1} = 0$, and

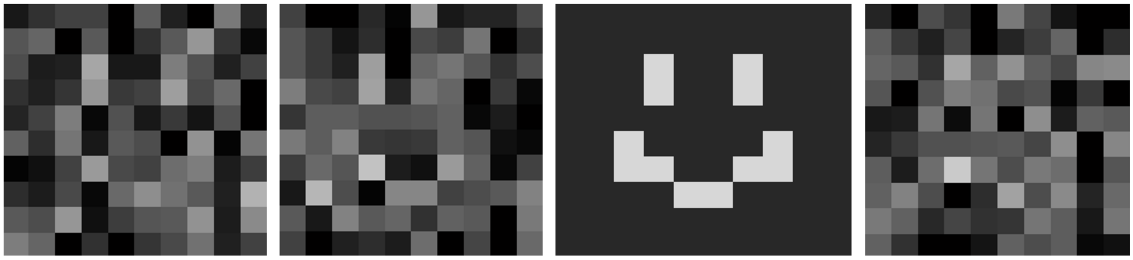

FIGURE 3.5: CS example: Suppose we measure a 10x10 pixel image with only 50 measurements (a compression of 50 percent). The measurements consist of imaging the scene through a series of 50 masks, with each mask having a random transparency for every pixel in the image. The signal measured for each mask is the sum of the intensities of the images pixels that pass through the mask. The random masks give some information about all parts of the scene, but with only 50 measurements of 100 pixels, the image is underdetermined. Each of the possible image estimates above, and an infinity more, give the same measurements when measured with our 50 simulated measurements. Which one is the real image? It is evident to a human because we expect natural images to have certain properties. Compressed sensing estimators attempt to search through all these possible images that match the measurements to find the one that has some property, such as smoothness, that we expect the true image to have.

$$soft(x, y) = \begin{cases} x + y & x \leqslant -y \\ x & |x| \leqslant y \\ x & x \leqslant -y \end{cases} \tag{3.31}$$

Another much faster-converging algorithm is the Two-Step Iterative Shrinkage/Thresholding Algorithm (TwIST)[101]. TwIST was the primary CS estimator used in the experimental work presented in chapter 6.

Natural images have properties that make them easy for a person to identify such as, sparsity, smoothness, lines, and edges. CS reconstruction algorithms try to find, from all the possible solutions, the solution that most exhibits the properties we expect the image to have — the prior. This is demonstrated in Fig. 3.5. These properties can usually be expressed in terms of sparsity minimization and so CS algorithms can be applied. For example an image of the night sky is expected to be

sparse in the Haar (pixel) basis. An image of a building on the other hand might be expected to be piecewise smooth and so would be sparse in a wavelet or curvelet basis. Then if $\mathbf{S}$ is a square matrix that transforms the scene into a basis in which we expect it to be sparse, $\mathbf{f_s} = \mathbf{Sf}$, then we can use the new measurement matrix,

$$\mathbf{H_s} = \mathbf{HS}^{-1} \tag{3.32}$$

to obtain the estimate for $\mathbf{f}$ in the sparse basis, $\mathbf{f}_{s,e}$ as,

$$\mathbf{f}_{s,e} = argmin_{\mathbf{f}_{s,e}} \|\mathbf{H}_s\mathbf{f}_{s,e} - \mathbf{g}\|_2^2 + \lambda R(\mathbf{f}_{s,e}) \tag{3.33}$$

and obtain $\mathbf{f}_e$ as $\mathbf{S}^{-1}\mathbf{f}_{s,e}$.

The nonlinear estimators of CS are also effective denoising algorithms and so are useful not only for solving linear equations with rank-deficient matrices, but also for equations with ill-conditioned matrices. The information presented in this section is largely credited to D. Bradys book Optical Imaging and Spectroscopy[90].

3.2 Measurement mode design

When undersampling a scene, the amount of information obtained per measurement becomes an important consideration because the the total information collected will be different for different sets of measurement modes. The more that is known about a scene, the more the measurement modes (the rows of $\mathbf{H}$) can be designed to maximize the expected information-per-measurement. For instance, if the scene is known to be sparse in the Haar basis, then making raster-scanned type measurements, where each mode measures a single point in the scene, would provide a lower expected information-per-measurement than a synthetic aperture radar (SAR)-type measurement where each sample measures every point in the scene but with different phases for each measurement. This is especially important for compressed sensing measurements because if the scene is undersampled with a set of measurements that

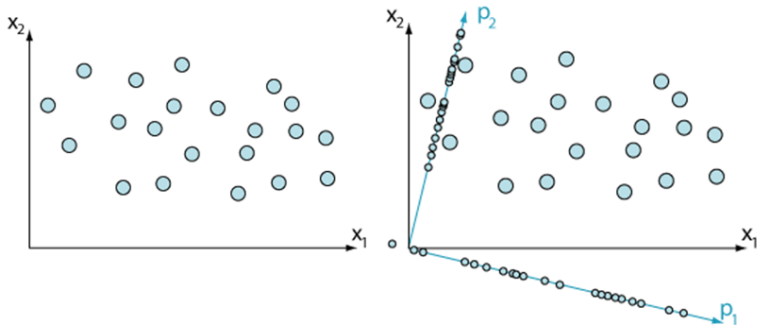

FIGURE 3.6: A scene can be represented as a vector (or point) in a space with dimension equal to the SBP. The space here has dimension 2, corresponding to a two pixel image. The axis $\mathbf{x_1}$ and $\mathbf{x_2}$ then might correspond to the intensities of these two pixels. We then plot each of our dictionary scenes as a blue circle. The first principal component vector, $\mathbf{p_1}$, is oriented such that the variance of the dictionary projected onto $\mathbf{p_1}$ is maximized there is no other possible vector that would result in a larger projected variance. The second principal component is perpendicular to $\mathbf{p_1}$. If the dimension of the space were higher, then $\mathbf{p_2}$ would be chosen to maximize the variance of the projected dictionary in that plane.

are inappropriate for that scene, no information at all may be obtained from some parts of the scene. Given any information about the expected structure of a scene, measurement modes can be designed for optimally undersampling the scene.

3.2.1 Principal component mode design

For these reasons we would like to consider how to design modes that are optimal for specific types of scenes. For instance, if we have a dictionary of examples of the type of scene we expect to image, how may we determine the best modes with which to image the scene? One approach is to use Principal Component Analysis (PCA)[102, 103]. PCA tries to estimate the vectors that most distinguish the variations in the data. Here we remember that an image can be considered as a vector existing in a space with dimension equal the SBP. The first principal component (PC) of a data set is the vector that maximizes the variance of the data set when it is projected onto that vector. The second PC is that vector that is orthogonal to the first PC of the

data that maximizes the projected variance, and so forth for the remaining PCs. To determine the principal components we must diagonalize the covariance matrix,

$$\mathbf{C} = (\mathbf{x} - \mu)(\mathbf{x} - \mu)^T \tag{3.34}$$

i.e. must solve the eigenvalue problem,

$$\mathbf{Cp} = \lambda \mathbf{p} \tag{3.35}$$

and sort the eigenvectors in order of decreasing eigenvalues. These are the principal components. The eigenvector of each principal component is the variance of the dictionary projected onto that principal component. The larger the eigenvalue, the more variance the projection onto the corresponding PC has, and thus the more information about the dictionary that PC measures.

The diagonalized covariance matrix will (of course) have zero off-diagonal (covariance) components, i.e. there is no correlation in the data between principal component directions. The PC vectors themselves are simply measurement modes that the scene can be projected onto. For example, illuminating a scene with a mode corresponding to one of the PCs and measuring the total light reflected from the scene corresponds to projecting the scene onto this PC. The PC modes can be thought of as capturing the most important/defining orthogonal properties of the dictionary elements, and so measuring scenes that are similar to the dictionary with the PCs will yield the most important features possible per measurement. As an example of PCA mode design, Fig. 3.7 shows the first 30 principal components, represented as images, of a dictionary of the letters 'D','U','K', and 'E'. If these 30 principal components are used as measurement modes, 400 pixel images of this type of letter can be successfully reconstructed directly from the 30 measurements, with no prior information. This is because for a known type of scene, described by a prior known dictionary of examples, PCA provides the ideal measurement modes. This

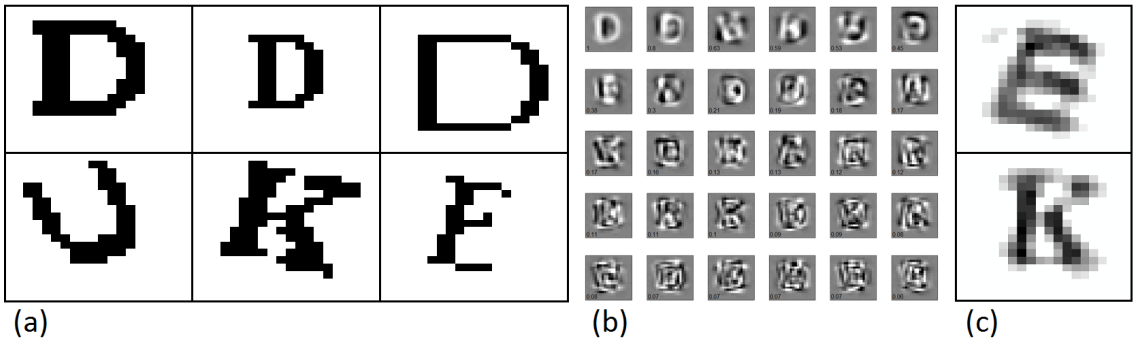

FIGURE 3.7: (a) Six elements from an 11,000 element dictionary of the letters 'D','U','K', and 'E'. The dictionary contains 20x20 pixel binary-color [0,1] images of these letters in 8 fonts with random rotations over $\pm 45^o$ and random shifts of up to 10% the letter size. (b) The first 30 principal components of this dictionary. The PCs contain values from -1 to 1; gray is zero. The numbers in the corners of each PCa image are the normalized eigenvalues of the PCs. (c) A 'K' and an 'E', not in the original dictionary, projected onto the largest 30 principal components.

technique is of measurement mode design has been experimentally demonstrated using structured illumination [38, 104].

3.2.2 Linear discriminant mode design

If we have yet more prior information about our dictionary and know the classes of the scenes present in the dictionary, how can we best distinguish the classes? Projecting onto the PCs offers no guarantee that we can distinguish the classes, unless the classes happen to be separated along the same axes as the variance of the over all dictionary. Projecting onto the mean-difference vector maximizes the separation of the projected means, but isn't necessarily any better at class segregation. Both the means of the class distributions and the variance of the distributions need to be taken into account. The solution: Maximize the projected mean separation while minimizing the variance of the projected classes. This yields Fishers linear discriminant [105],

$$J(\mathbf{l}) = \frac{\mathbf{l}^T \mathbf{C}_B \mathbf{l}}{\mathbf{l}^T \mathbf{C}_W \mathbf{l}} \tag{3.36}$$

$$\mathbf{C}_W = \sum_{\forall Classes} \sum_{x \in Class_i} \frac{\mathbf{x} - \mu_i}{\mathbf{x} - \mu_i}^T \tag{3.37}$$

$\mathbf{C}_B$ is the between-class covariance matrix, i.e. the covariance of the means of the classes, and $\mathbf{C}_W$ is the within-class summed covariance matrix, i.e. the sum of the covariance of the elements in each class. Or for two classes,

$$J(\mathbf{l}) = \frac{|\mu_1' - \mu_2'|^2}{v_1^2 + v_2'^2} \tag{3.38}$$

Maximizing $J(\mathbf{l})$ corresponds to finding the vector l that groups each class as tightly as possible while simultaneously separating the means of the classes as much as possible, when the dictionary is projected onto l. The vector that maximizes Fishers linear discriminant is found by solving the generalized eigenvalue problem,

$$\mathbf{C}_W^{-1}\mathbf{C}_B\mathbf{l} = \lambda\mathbf{l} \tag{3.39}$$

The eigenvectors of this equation are known as the linear discriminants of the classes that are present in the data. Linear Discriminant Analysis (LDA) tries to estimate the vectors that most distinguish the classes in the data. The amount of each linear discriminate mode present in a scene, relative to the amount of each of the other modes, gives the likelihood that the class discriminated by that linear discriminate is present in the scene. One challenge for LDA is that for a task with very high dimensional data such as images, the traditional LDA algorithm encounters several difficulties. Consider face recognition for example. A low-definition face image of size 64 by 64 implies a SBP of 64x64 = 4096 dimensions, and therefore scatter matrices of size 4096x4096 = 16M. First, it is computationally challenging to handle big matrices (such as computing eigenvalues). Second, those matrices are almost always singular, as the number of training images needs to be at least 16M for them to be non-degenerate. A solution to this is to first reduce the dimensionality of the

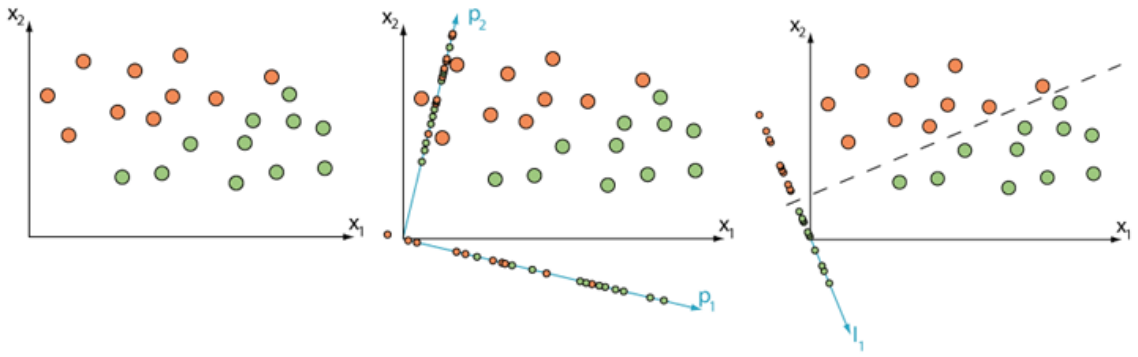

FIGURE 3.8: Here we know the class of our dictionary elements (represented as orange for class 1 and green for class 2). (Center) Projecting the dictionary elements onto the principal components results is some mixing. (Right) Projecting onto the linear discriminant, $\mathbf{l_1}$, separates the means of the projected data as much as possible and does a much better job dividing the projected dictionary elements into classes.

data set with PCA by projecting the dictionary onto the principal components, then perform decision with LDA[106].

To demonstrate the possibility of using metamaterial apertures to perform designer mode generation, we have considered a metamaterial hologram system that generates precise modes for object detection. The modes can be calculated from dictionary-analysis approaches, such as PCA or LDA, shown in Fig. 3.7. We have simulated a 'D','U','K','E' letter detector. This four-measurement system that detect the likelihood that each of the letters 'D','U','K', and 'E' are present in a scene. This is similar to feature-specific imaging[104], except that the number of features sampled are be very small, only enough to identify whether an object is present in the scene or not. Previous work on feature-specific imaging hardware implementations has been limited to traditional lens-based imaging systems with projector-based illumination[38, 39], or digital micromirrors (DMDs)[32, 33], to sample the specific feature detection modes.

Here we have designed a single metamaterial hologram that generates the desired measurement modes directly, without the need for lenses or other hardware. All the

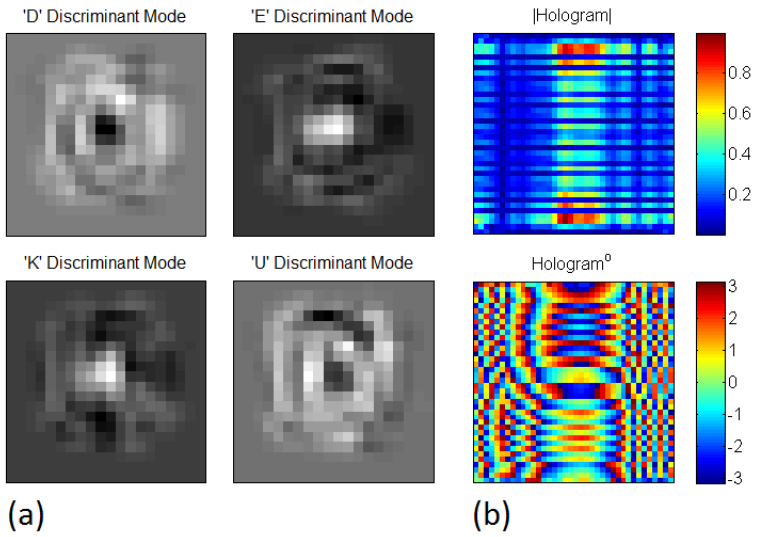

FIGURE 3.9: (a) The D,U,K,E linear discriminant modes. (b) The complex hologram that generates these modes when illuminated from four different directions.

processing occurs in the metamaterial, with the likelihood that each of the letters is present being directly related to the four measurements made by the system. The metamaterial hologram was designed such that when it is is illuminated with a horn from one of four different directions, it produces one of the four linear discriminant modes that detect one of the letters. The detection modes were determined by using PCA to reduce the dimensionality of the same 11,000 element dictionary of the four letters used above, and then applying LDA to determine the four discriminant modes.

The hologram itself was designed by inverting the mode formation equation with four sources and four modes. If a hologram, $h(r_p)$ consisting of P controllable pixels produces a radiation pattern, $s_k(r_n)$, when it is illuminated by a source located at r_k, then the radiation pattern produced by the hologram when illuminated by the k^{th} source is,

$$s_k(r_n) = \sum_p^P g(r_n - r_p)h(r_p)g(r_p - r_k) \tag{3.40}$$

where $g(r)$ is the Green's function for free-space propagation. This can be written in matrix form simply as,

$$\mathbf{s} = \mathbf{Gh} \tag{3.41}$$

where the entries of the matrix $\mathbf{G}$ are the Green's functions for each source concatenated together along the rows as $g_{nk,p} = g(r_n - r_p)g(r_p - r_k)$, $\mathbf{s}$ is a column vector containing each of the radiation patterns concatenated together, and $\mathbf{h}$ is a column vector with entries indicating the amplitude and phase that the hologram must have at each pixel to produce the desired mode. Inverting Eqn. 3.41 gives the hologram. The specific hologram that generates the LDA modes these modes is shown in Fig. 3.9. It was 0.5m x 0.5m and 0.8m from the sources which were located at the four corners of the hologram. Calculating the radiation patterns generated by this hologram shows perfect agreement with the desired LDA modes. Simulation of detection, made by projecting a new letter, not in the dictionary, onto the four modes generated by this hologram shows 90% accuracy in detection.

3.3 Metamaterial imaging forward model

As described above in section 3.1, the imaging process can be expressed mathematically by the relation $\mathbf{g} = \mathbf{Hf} + \mathbf{n}$, where $\mathbf{g}$ is a collection of measurements, $\mathbf{H}$ is the measurement matrix (a row-wise array of all measurement modes), and $\mathbf{f}$ is the sampled scene. The problem of image estimation becomes one of solving this equation for $\mathbf{f}$. The first step in building an imaging system then is the determination of the measurement matrix $\mathbf{H}$. This is accomplished by creating a forward model of the imaging system that contains all the physics of the imaging process. The forward

model can then be used to determine the entries of **H**. For the metamaterial imaging systems discussed below, the imaging systems will deal with metamaterial apertures emitting and receiving coherent light, so we need to develop a forward model that describes this process.

Consider a system in which one aperture coherently illuminates a scene and a second aperture coherently receives light scattered by the scene. Each aperture is coupled to a single source/detector. Let $S_{tx}(\mathbf{r}_{tx})$ be the transfer function from the source to point $\mathbf{r}_{tx}$ on the illuminating aperture A_{tx}. Then for source electric field magnitude, $\mathbf{E_s}$, the electric field across the transmitting aperture is given by,

$$E_{tx}(\mathbf{r}_{tx}) = S_{tx}(\mathbf{r}_{tx})E_s \tag{3.42}$$

The field at scene-point $\mathbf{r}_n$ generated by the transmitting aperture is then given by the convolution,

$$E_{scene}(\mathbf{r}_n) = \int_{A^{tx}} S_{tx}(\mathbf{r}_{tx})G(\mathbf{r}_n - \mathbf{r}_{tx})E_s d\mathbf{r}_{tx} \tag{3.43}$$

where $G(\mathbf{r})$ is the Greens function of free-space wave propagation, which according to the Kirchhoff-Fresnel diffraction formula[107] is $G(\mathbf{r}) = -\frac{e^{-ik_0|\mathbf{r}|}}{4\pi|\mathbf{r}|}\left(ik\cos(\theta) + \frac{\partial}{\partial z}\right)$. We note that dividing out the source electric field magnitude, the above integral gives the unitless radiation pattern $R(\mathbf{r}_n)$ of the transmitting antenna,

$$R_{tx}(\mathbf{r}_n) = \int_{A_{tx}} S_{tx}\mathbf{r}_{tx}G(\mathbf{r}_n - \mathbf{r}_{tx}d\mathbf{r}_{tx} \tag{3.44}$$

Now let $S_{rx}(\mathbf{r}_{rx})$ be the transfer function from the detector to point r on the receiving aperture A_{rx}. For an incident electric field $E_{rx}(\mathbf{r}_{rx})$ across the receiving antenna aperture, the electric field magnitude at the detector is,

$$E_d = \int_{A_{rx}} E_{rx}(\mathbf{r}_{rx})S_{rx}(\mathbf{r}_{rx})d\mathbf{r}_{rx} \tag{3.45}$$

We define a scene as a spatially varying scattering density $f(\mathbf{r}_n)$, such that when an electric field is incident on a point in the scene, the scattered field magnitude at the point in the scene is,

$$E_{scattered}(\mathbf{r}) = f(\mathbf{r})E_{scene}(\mathbf{r}) \tag{3.46}$$

In defining the scene this way, we are making the first Born approximation of the scene scattering and hence ignore multipath scattering.

The field scattered back to point $\mathbf{r}_{a'}$ on the receiving aperture from point all points in the scene is,

$$E(r_{rx}) = \int_{scene} f(\mathbf{r}_n) \int_{A^{tx}} S_{tx}(\mathbf{r}_{tx})G(\mathbf{r}_n - \mathbf{r}_{tx})E_s d\mathbf{r}_{tx} G(\mathbf{r}_{rx} - \mathbf{r}_n)d\mathbf{r}_n \tag{3.47}$$

Then the field magnitude at the detector, normalized to the source electric field, from the all the radiators on the receiving aperture is,

$$\frac{E_d}{E_s} = \int_{A_{rx}} \left(\int_{scene} f(\mathbf{r}_n) \int_{A_{tx}} S_{tx}(\mathbf{r}_{tx})G(\mathbf{r}_n - \mathbf{r}_{tx})E_s d\mathbf{r}_{tx} G(\mathbf{r}_{rx} - \mathbf{r}_n)d\mathbf{r}_n \right) S_{rx}(\mathbf{r}_{rx})d\mathbf{r}_{rx} \tag{3.48}$$

Carefully reordering the integrations gives,

$$\frac{E_d}{E_s} = \int_{scene} \int_{A_{tx}} S_{tx}(\mathbf{r}_{tx})G(\mathbf{r}_n - \mathbf{r}_{tx})E_s d\mathbf{r}_{tx} \int_{A_{rx}} S_{rx}(\mathbf{r}_{rx})G(\mathbf{r}_{rx} - \mathbf{r}_n s)d\mathbf{r}_{rx} f(\mathbf{r}_n)d\mathbf{r}_n \tag{3.49}$$

Because spatial information in the scene smaller than the diffraction limit does not propagate from the scene to the receive aperture, we may consider only a discrete set of N diffraction limited points in the scene. When we discretize the scene, the scattering density from the scene patch at point $\mathbf{r}_n$ becomes $F(\mathbf{r}_n, \mathbf{r}_{rx}, \mathbf{r}_{tx})f(\mathbf{r}_n)$, where $F(\mathbf{r}_n, \mathbf{r}_{rx}, \mathbf{r}_{tx})$ is the bistatic scattering pattern of the scattering to observation

point $\mathbf{r}_{rx}$ when the patch is illuminated from point $\mathbf{r}_{tx}$. We now have,

$$\frac{E_d}{E_s} = \sum_{s=1}^{N} \int_{A_{tx}} S_{tx}(\mathbf{r}_{tx}) G(\mathbf{r}_n - \mathbf{r}_{tx}) E_s d\mathbf{r}_{tx} \int_{A_{rx}} S_{rx}(\mathbf{r}_{rx}) G(\mathbf{r}_{rx} - \mathbf{r}_n) d\mathbf{r}_{rx} F(\mathbf{r}_n, \mathbf{r}_{rx}, \mathbf{r}_{tx}) f(\mathbf{r}_n) \tag{3.50}$$

We can write this summation over the N diffraction limited points in the scene in matrix form as,

$$\frac{E_d}{E_s} = [h_1 h_2 \dots h_n \dots h_N] \begin{bmatrix} f_1 \\ f_2 \\ \vdots \\ f_n \\ \vdots \\ f_N \end{bmatrix} \tag{3.51}$$

where,

$$h_n = \int_{A_{tx}} S_{tx}(\mathbf{r}_{tx}) G(\mathbf{r}_n - \mathbf{r}_{tx}) E_s d\mathbf{r}_{tx} \int_{A_{rx}} S_{rx}(\mathbf{r}_{rx}) G(\mathbf{r}_{rx} - \mathbf{r}_n) d\mathbf{r}_{rx} F(\mathbf{r}_n, \mathbf{r}_{rx}, \mathbf{r}_{tx}) \tag{3.52}$$

and,

$$f_s = f(\mathbf{r}_n) \tag{3.53}$$

If $F(\mathbf{r}_n, \mathbf{r}_{rx}, \mathbf{r}_{tx})$ is a constant (as it would be if the scene were composed of isotropic point scatters) or independent of $\mathbf{r}_{tx}$ and $\mathbf{r}_{rx}$ (as it would be if the scene is in the far-field of the apertures), then h_s can be further simplified. Dropping the $F(\mathbf{r}_n, \mathbf{r}_{rx}, \mathbf{r}_{tx})$ term, the integrals over the transmitting and receiving apertures are just the unitless radiation patterns of the two apertures. So,

$$h_n = R^{tx}(\mathbf{r}_n) R^{rx}(\mathbf{r}_n) \tag{3.54}$$

If the scene is illuminated with M different transmit/receive aperture combinations, giving M electric field amplitudes measured at the detector, then the vector of all

measurements may be expressed as,

$$\begin{bmatrix} f_1 \\ f_2 \\ \dots \\ f_N \end{bmatrix} \frac{1}{E_s} = \begin{bmatrix} h_{11} & h_{12} & \dots & h_{1N} \\ h_{21} & h_{22} & & \\ \vdots & & \ddots & \\ h_{M1} & & & h_{MN} \end{bmatrix} \begin{bmatrix} f_1 \\ f_2 \\ \vdots \\ f_N \end{bmatrix} \tag{3.55}$$

where,

$$h_{mn} = R_m^{tx}(\mathbf{r}_n) R_m^{rx}(\mathbf{r}_n) \tag{3.56}$$

and R_{mn}^{tx} is the radiation pattern at the n^{th} scene point from the m^{th} transmit aperture field distribution, and R_{mn}^{rx} is the radiation pattern at the n^{th} scene point from the m^{th} receive aperture field distribution. The transmitting and receiving apertures may simultaneously have the same field pattern and may even be the same aperture.

The scene-patch scattering pattern, $F(\mathbf{r}_n, \mathbf{r}_{rx}, \mathbf{r}_{tx})$ is an example of the complicated - and in this case non-linear - relationship between the scene-object and the scene-signal discussed in the Introduction. The scattered light may have a great deal of gain for large voxels and the direction of this gain is dependent on the structure of the surfaces inside the voxel making it non-linear. For relatively smooth surfaces this results in the signal being reflected mainly in the specular direction. In RF imaging systems this often manifests as a difficulty seeing the sides of objects.

3.4 Fourier optics overview

Having determined that the radiation modes of an aperture are directly related to the measurement matrix, it remains to determine what radiation modes are generated from an aperture. To do this we need to understand how the field at the aperture of an imaging system is related to the field everywhere else in space. An usefull and insightful way to relate these fields is with the plane-wave-spectrum formulation of wave diffraction. In the following discussion we consider a 1D aperture perpendicular

to the z-axis, parallel to the x-axis, and infinite in the y-direction, with some y-polarized field, E_a, across the aperture. Because of the geometry of the aperture and the polarization of the field we may treat E_a as a scalar field. The information presented in this section is largely credited to J. Goodmans book "Introduction to Fourier Optics"[107] and E. Hechts book "Optics"[108].

We may decompose the aperture field into the all the possible sinusoidial functions that, when integrated over the aperture plane, would give that field. This is a Fourier decomposition of the aperture field. Each of these components has the form,

$$A(k_x)e^{-ik_x x} \tag{3.57}$$

where,

$$A(k_x) = \int E_a(x)e^{ik_x x}dx = FT\{E_a(x)\} \tag{3.58}$$

where $FT\{\cdot\}$ is the Fourier transform. Thus the entire aperture field is given by the integral,

$$E_a(x) = \int A(k_x)e^{-ik_x x}dk_x \tag{3.59}$$

which is evaluated over $-\infty < k_x < \infty$. We can think of each of these fields as being caused by the intersection with the $z = 0$ plane of a plane wave (or, perhaps more accurately, as producing this plane wave),

$$A(k_x)e^{-i(k_x x + k_z z)} = A(k_x)e^{-i(k_x x + \sqrt{k_0^2 - k_x^2}z)} \tag{3.60}$$

The field on the aperture is given by the superposition of all the plane waves at z=0. The field at a distance z from the aperture is then given by,

$$\begin{aligned} E(x,z) &= \int A(k_x)e^{-ikr}dk_x \\ &= \int A(k_x)e^{-i(k_x x + \sqrt{k_0^2 - k_x^2}z)}dk_x \\ &= FT^{-1}\left\{FT\left\{E_a(x)\right\}e^{-i\sqrt{k_0^2 - k_x^2}z}\right\} \end{aligned} \tag{3.61}$$

Each of these plane waves will propagate away from the aperture-plane parallel to the vector (k_x, k_z), or in other words, along the angle from the z-axis (optical axis),

$$\theta = sin^{-1}\left(\frac{k_x}{k_0}\right) \tag{3.62}$$

and has a magnitude proportional to $A(k_x)$, the Fourier coefficient of the k_x spatial-frequency of the aperture field. This angle $sin^{-1}(k_x/k_0)$ is just the direction along which the infinite plane wave with this k_x will travel, so naively it would seem that this infinite plane wave actually contributes to every angle in the far-field. However this is not the case; the plane wave traveling along direction $sin^{-1}(k_x/k_0)$ only contributes to the far-field along this direction. The only plane wave that contributes field to the points along the direction θ in the far-field is the plane wave with the k_x that satisfies $\theta = sin^{-1}(k_x/k_0)$. The reason is because, in the far-field, all the other contributions from other plane-waves cancel out.

At first, this seems to directly contradict the previous statement that the far-field in a particular direction depends only on the amplitude of the plane-wave propagating in that direction, but what happens when we evaluate this integral?

A property of integrating over many periodic functions is that if their phases are approximately the same they add up, but if their phases vary rapidly with the integration variable they cancel out. This allows us to make a stationary-phase approximation. This approximation says that where the phase of an integrand varies rapidly with the integration variable, we can set the integral over that region to zero. Consider the integral,

$$I = \int A(k)e^{i\phi(k)}dk \tag{3.63}$$

If we know that the phase of the integrand varies rapidly everywhere except about special points of stationary phase we may only have to evaluate the integral about

these points. Call a point k_s where $d\phi/dk(k_s) = 0$ a point of stationary phase. The integration around this point will have the most contribution to the integral. Take the first three terms of a Taylor expansion of $\phi(k)$ about this stationary point,

$$\phi(k)\phi(k_s) + \frac{d\phi}{dk}(k_s)(k-k_s) + 1/2\frac{d^2\phi}{dk^2}(k_s)(k-k_s)^2\phi(k_s) + 1/2\frac{d^2\phi}{dk^2}(k_s)(k-k_s)^2 \quad (3.64)$$

and plug this into the integral for I,

$$I \approx \int A(k)e^{i(\phi(k_s)+1/2\frac{d^2\phi}{dk^2}(k_s)(k-k_s)^2)}dk = A(k_s)e^{i\phi(k_s)}\int e^{i1/2\frac{d^2\phi}{dk^2}(k_s)(k-k_s)^2}dk \quad (3.65)$$

We can take $A(k)$ outside the integral here because we assume that $A(k) \approx A(k_s)$ in the vicinity of the stationary phase point. Again, the idea here is that we only need to evaluate the integral over a small region about the stationary phase point since outside this region we know that the rapidly varying phase of the integrand will cause the integration to cancel out. Since we are integrating over a small region, we can integrate over an approximation of the integrand given by the first few terms of a Taylor series expansion. Evaluating the remaining integral for I gives,

$$I \approx \sqrt{\frac{2\pi}{i\frac{d^2\phi}{dk^2}(k_s))}}A(k_s)e^{i\phi(k_s)} \quad (3.66)$$

So back to the plane wave integration for the field at position (r, θ) from the aperture,

$$E(r,\theta) = \int A(k_x)e^{i(k_x x + \sqrt{k_0^2-k_x^2}z)}dk_x \quad (3.67)$$

where $x = rsin(\theta)$ and $y = rcos(\theta)$. Can we make a stationary phase approximation for this integral? The phase of our integrand is, $\phi = k_x x + \sqrt{k_0^2 - k_x^2}z$ We can make a stationary phase approximation if the derivative w.r.t. k_x is large everywhere except about a certain point(s). The derivative is,

$$\frac{d\phi}{dk_x} = x - \frac{k_x z}{\sqrt{k_0^2 - k_x^2}} = rsin(\theta) - rcos(\theta)\frac{k_x}{\sqrt{k_0^2 - k_x^2}} \quad (3.68)$$

We see *in the limit that r is very large* (i.e. in the far-field),

$$\lim_{r\to\infty} \frac{d\phi}{dk_x} = \begin{cases} 0 & \text{when} sin(\theta) = k_x/k_0 \\ \infty & \text{otherwise} \end{cases} \tag{3.69}$$

We see that we do in fact have a strongly isolated stationary point at exactly spatial-frequency corresponding to the plane wave propagating along the direction toward the point at which we are evaluating our field. If we evaluate the plane-wave integral with the stationary phase approximation about this point we get,

$$E_{far}(r,\theta) = \sqrt{\frac{i2\pi k_0}{r}} e^{-irk_0} cos(\theta) A(k_s) \tag{3.70}$$

where k_s is given by $k_s = k_0 sin(\theta)$. A similar derivation gives the field in two dimensions from a two-dimensional aperture as,

$$E_{far}(r,\theta,\phi) = \frac{i2\pi k_0}{r} e^{-irk_0} cos(\theta) A(k_{xs}, k_{ys}) \tag{3.71}$$

where $k_{xs} = k_0 sin(\theta) cos(\phi)$,and $k_{ys} = k_0 sin(\theta) sin(\phi)$. Here θ is still the angle from the z-axis (optical axis) and ϕ is the angle from the x-axis measured in the x-y plane (plane of the aperture).

Expressions 3.70 and 3.71 relate the one- and two-dimensional far-fields due to a field distribution across a planar-aperture to the Fourier transform coefficients of the aperture field. While the Fourier, or plane-wave, basis representation of the aperture field allows us to represent the fields at any point, in the near- or far-field regions, as a superposition of plane-waves, we find that in the far-field, we need only consider a single Fourier component per direction. This yields interesting consequences, for instance if we consider a lens placed in the far-field from some scene that we wish to image, only the spatial-frequency components of the scene that correspond to propagation directions captured by the lens are recorded. Since finer resolution information about the scene corresponds to plane waves with larger transverse wavenumbers, and

these plane-waves propagate at larger angles from the optical-axis, a lens acts as a low-pass filter where the spatial-bandwidth (i.e. resolution) passed is proportional to the diameter of the lens.

Additionally, because plane-waves with $k_x^2 + k_y^2 > k_0 = \omega/c$ are evanescent, free-space itself can be thought of as a low-pass filter[90]. At any given frequency there is a maximum propagating wavenumber. Any scene information, such as sharp edges, that has spatial-frequencies greater than k_0 will not be transmitted in the far-field. The plane waves corresponding to increasing spatial-frequencies of the aperture field will propagate with increasing angle from the optical axis until, for spatial-frequencies equal to k_0, the plane waves propagate at 90^o from the optical axis beyond which the waves become evanescent.

This angular spectrum interpretation of aperture radiation yields a simple understanding of the three propagation regions often referred to by antenna engineers. The *reactive-near-field* is the region close to the aperture, usually defined as within one λ, within which there may be substantial evanescent waves. Anything within this region can couple through the evanescent fields to capacitively or inductively load the antenna and must be considered as part of the antenna itself. The *far-field* is then the region where the stationary-phase approximation is valid, usually defined as beyond $2A^2/\lambda$ where A is the maximum dimension of the antenna, and the field at any point may be described as an a single plane-wave that propagates in the direction from the antenna to that point and which varies with range only as e^{-irk_0}/r. The region in between the reactive-near-field and the far-field is termed the *radiative-nearfield*. In this region there are no evanescent waves, but the field at any point must be described as the superposition of an infinite number of plane waves propagating to that point from all directions in the half-space behind the antenna.

3.5 Conclusions

One important point to make explicit here is that the space in which the scene exists and the space in which the measurements exist do not have to be the same, and a general imaging system transforms a signal between these spaces. In fact, the dimension of the scene space and the measurement space do not even need to be the same. A traditional lens-based imaging system with a focal-place detector array makes measurement of the spatial scene with spatially indexed detectors — both the scene and the measurements exist in physical space and are of the same dimension. In comparison, a coded-aperture imaging system with a single-detector makes measurements that are indexed by mask number, and so exist in a more abstract mask-number-space, and the dimension of the measurement space can be much less than the dimension of the scene. In Chapter 6 we will discuss a unique metamaterial imaging system that makes measurements that are indexed by frequency and so exist in temporal frequency-space. Computational imaging provides the mathematical framework needed to invert this transformation and recover an image of the scene, while compressed sensing allows the dimension of the measurement space to be smaller than the scene space.

The metamaterial imaging forward model describes the physics of a coherent imaging system in which an arbitrary aperture transforms between radiated measurement modes and some measurement space. This is the essential link that places the physics of a coherent aperture in the framework of computational imaging and allows a metamaterial aperture to be used for imaging. As such, the images produced by such a computational imaging system are limited by the accuracy of the forward model. For this reason it is important in the future to address some of the nonlinearities of this forward model that have been ignored, in particular the secularity of the reflection from scene-patches.

4

Complementary Metamaterials and Metamaterial Antennas

A metamaterial is an artificial composite material that is designed to respond to light in engineered ways. Metamaterials are composed of individual subwavelength elements that are distributed throughout the bulk of the material[60, 86]. Each of these elements has a controllable polarizability that may be designed to couple to either the electric field or magnetic field of a propagating light wave. At light frequencies below the near-IR, these elements are often created by patterning metal to make simple RLC circuits. If these elements are repeated periodically and are substantially smaller than a wavelength, then they may be homogenized such that the details of the individual elements are disregarded in favor of equivalent complex bulk material parameters. Hence, the composite material with all of its engineered structure may be thought of as a rather simpler homogeneous material.

Depending on the design of metamaterial unit cell, the way that it responds to light may be carefully controlled. By controlling the symmetries of the metamaterial elements, the field component, E or H, of light that they couple to may be controlled. They may be designed to be isotropic or anisotropic. By tuning the

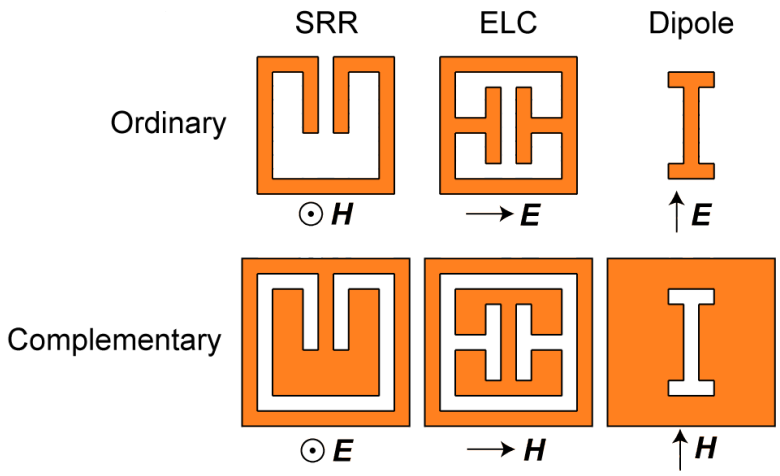

FIGURE 4.1: The basic types of metamaterials and the fields to which they couple. (Top Row) the resonant split-ring-resonator (SRR), the resonant electric-inductive-capacitive resonator (ELC), the non-resonant dipole. (Bottom Row) the resonant complementary-SRR (cSRR), the resonant complementary-ELC (cELC), and the non-resonant complementary-dipole. Orange represents a conductive metal sheet and white represents air or another dielectric.

capacitance and inductance of the elements, electric and magnetic resonances can be achieved. While few non-conducting natural materials couple to the magnetic field, metamaterials that couple to magnetic fields can be readily created providing a suite of unprecedented material properties. The ability to simultaneously control both the magnetic and electric responses of a material allows for variable-index, impedance matched materials and even negative index materials to be created. The geometry of the elements may be varied spatially to create gradient index devices, including transformation-optical devices such as cloaks[25, 10, 11]. This has immediate applications to imaging as gradient index lenses, such as Luneburg lenses, parabolic GRIN lenses, and Rotman lenses[19, 66, 45, 67, 74, 21] have the ability to surpass the performance of simple refractive lenses. Furthermore, metamaterial holograms are capable of forming complex, user-defined radiation patterns by varying the index of refraction across a thin metamaterial slab[109].

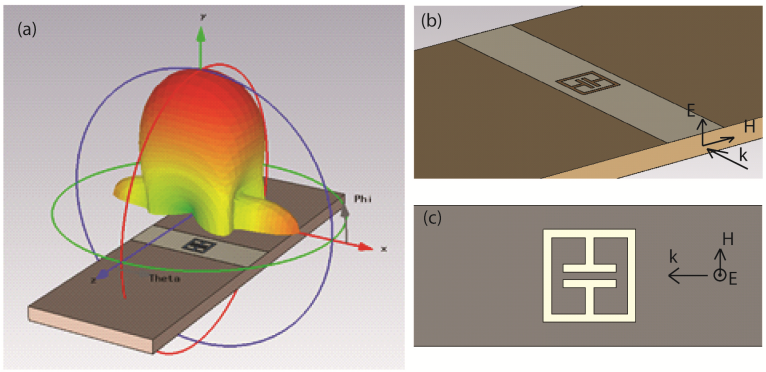

FIGURE 4.2: Unit cell of a C-ELC in a microstrip transmission line which exhibits a magnetic response for waves along the microstrip. (b)/(c) brown/white is dielectric and grey is metal. (a) shows the linear-scale far field radiation pattern for a single C-ELC excited by the microstrip mode.

4.1 Complementary metamaterials

Another class of metamaterials are so-called complementary metamaterials (CMs). CMs are created by transposing the placement of metal and dielectric in a normal metamaterial structure, as such, a complementary metamaterial is often referred to by prefixing a c in front of the abbreviation for it ordinary counterpart (Fig. 4.1). By Babinets principle, which relates the field diffracted from a thin solid metallic object to a hole in a metallic sheet of the same size, these complementary structures are expected to have the dual response of the normal metamaterial[84]. So a complementary electric dipole behaves as a magnetic dipole with the same frequency response and vice-versa. A complementary dipole etched into a conducting sheet may be considered as two dipoles on either side of the sheet which are 180^o out of phase with each other. This makes complementary metamaterials inherently two-dimensional. Instead of constructing bulk arrays of CM sheets, CMs are usually etched into one of the conductors of a transmission line. Then the dipole polarization on the inside of the transmission line interacts with the guided wave, and the transmission line behaves as if filled with a material of the same properties as the CM element[110].

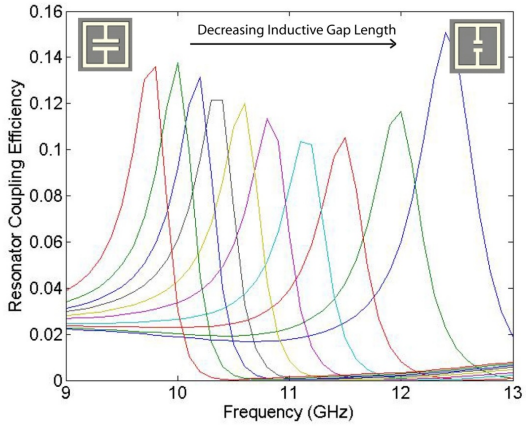

FIGURE 4.3: The resonator coupling efficiency (Power radiated / Power incident) of resonators with different geometries (colored curves) as a function of frequency. For any one resonator geometry, the percent bandwidth of the radiation efficiency is about 10 percent, comparable to the resonance bandwidth of the structure. This dispersion allows the radiation efficiency at any single frequency to be tuned continuously from on to off by varying the resonator geometry.

Meanwhile the dipole polarization on the outside of the transmission line interacts with free-space and may in fact radiate. This results in coupling between the guided wave in the transmission line and free-space radiation via the CM element.

The procedure for determining the effective medium properties of a complementary metamaterial through the use of S-parameter retrieval is similar to that used to retrieve the constitutive parameters for volumetric metamaterials, though the peculiarities of the gaps within the complementary elements introduce some complications [111]. Were the waveguide closed to free space, a specification of simple boundary conditions around the waveguide region would suffice to define the computational domain. However, because the waveguide is essentially open to free space through the gaps associated with the complementary elements, energy can leak out or radiate into the free space region. The radiation may be desirable or undesirable depending on the application, but in either case, it must be accounted for properly in order to obtain accurate retrievals.

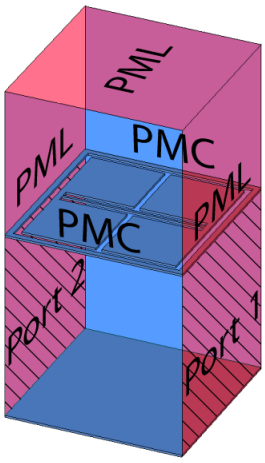

FIGURE 4.4: Diagram of the boundary conditions used to retrieve the effective constitutive parameters of a complementary metamaterial.

A typical S-parameters configuration needed to retrieve the constitutive parameters for a complementary metamaterial is shown in Fig. 4.4. Ports are introduced on either side of the waveguide such that a given port occupies the region from the lower to the upper conductor. To simplify the discussion, all of the complementary structures considered here are planar waveguide, with the mode introduced being the fundamental TEM mode polarized such that the electric field is perpendicular to the metal plates while the magnetic field is parallel to the plates and perpendicular to the direction of propagation. To account for the potential of radiation from the complementary element, the computational domain is extended beyond the top of the element, and perfectly matched layers (PMLs) are defined on the three walls transverse to the propagation direction. Perfect magnetic conducting boundary conditions (PMCs) are specified on the planes perpendicular to the direction of propagation within the waveguide region between the conductors.

As is usually the case in S-parameter retrievals, the boundary conditions effectively model a structure of infinite extent transverse to the direction of propagation, and of finite extent (one element thick) in the direction of propagation. The TEM

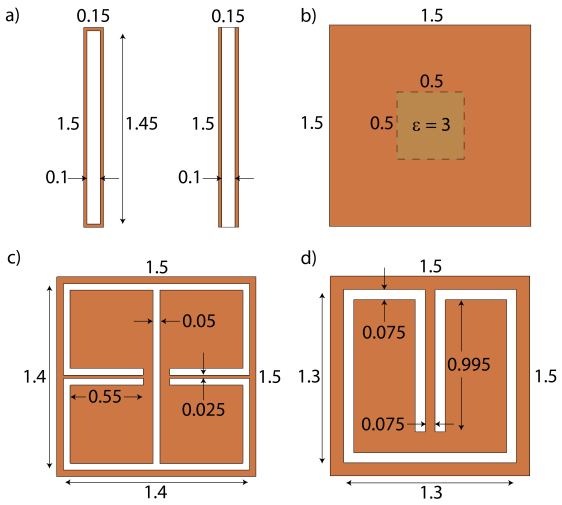

FIGURE 4.5: Diagrams of the complementary metamaterials used to retrieve the effective constitutive parameters in Figs. 4.6. All dimensions in millimeters. In all cases the substrate thickness was 1.59 mm, the metal thickness was 17 microns and the substrate was vacuum. a) shows the complementary cut wire and the complementary plasmonic wire. b) shows the dielectric loaded structure. c) shows the complementary ELC and d) shows the complementary SRR. The negative index unit cell was a combination of the metamaterials in c) and d).Diagrams of the complementary metamaterials used to retrieve the effective constitutive parameters in Figs. 5 and 6. All dimensions in millimeters. In all cases the substrate thickness was 1.59 mm, the metal thickness was 17 microns and the substrate was vacuum. a) shows the complementary cut wire and the complementary plasmonic wire. b) shows the dielectric loaded structure. c) shows the complementary ELC and d) shows the complementary SRR. The negative index unit cell was a combination of the metamaterials in c) and d).

nature of the parallel plate waveguide enables this simplified description. Because the modes of a microstrip line (as shown in Fig. 4.2, top) are nearly TEM like, it is possible to perform retrievals in a similar manner as described here, except that enough space must be introduced such that the microstrip mode is not perturbed by the boundary conditions.

The retrieved parameters from a selection of complementary elements (dimensions in Fig. 4.5) are shown in Fig. 4.6. The constitutive parameters for a finite length wire (c-cut-wire) are shown in Fig. 4.6, for the two orthogonal directions of propagation.

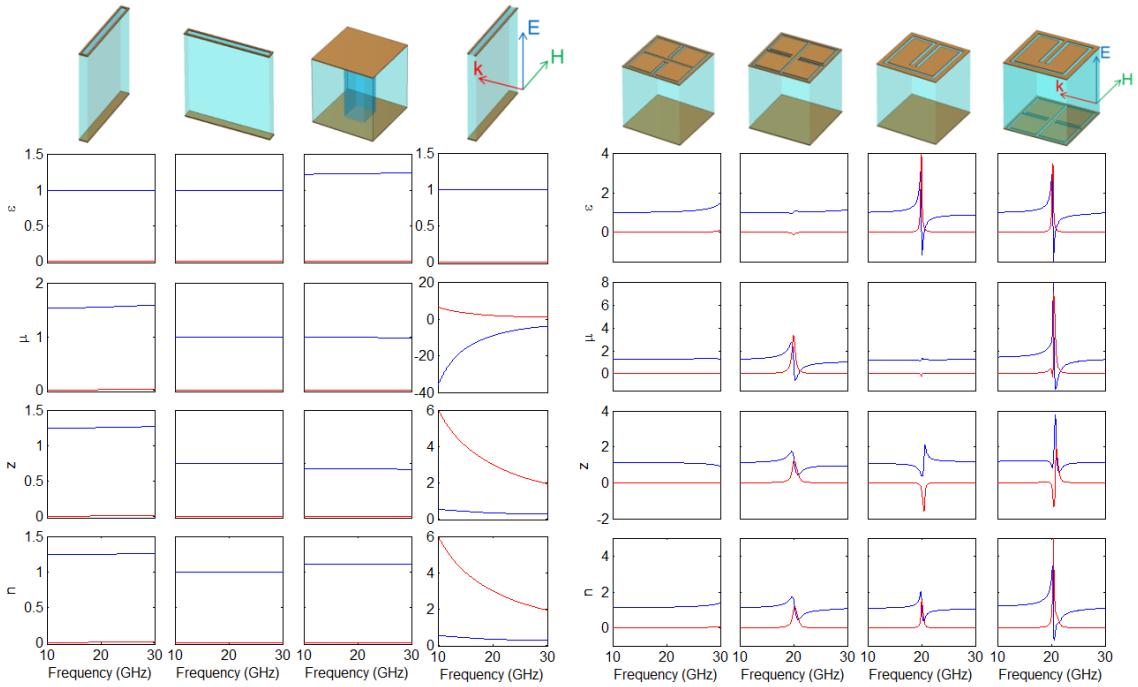

FIGURE 4.6: A selection of nonresonant (Left) and resonant (Right) complementary metamaterials and their retrieved constitutive parameters.

As described above, the c-cut-wire provides a magnetic response that, below its resonance frequency, can be nearly dispersionless. For the orientation in which the magnetic field is along the wire, the permeability has a moderate positive value that only mildly disperses with frequency. The positive magnetic response can be increased considerably by decreasing the thickness of the complementary wire, which increases the series capacitance. When the wave is oriented such that the propagation direction is perpendicular to the wire, there is virtually no response and the section of waveguide behaves as if filled with free space.

One feature of CM implemented in transmission lines is radiative loss on the outside of the transmission line structure, as shown in Fig. 4.2. The CM elements radiate on both sides of the ground plane and the energy radiated outside the transmission line is lost. This effect can be utilized to create sub-wavelength radiators which can

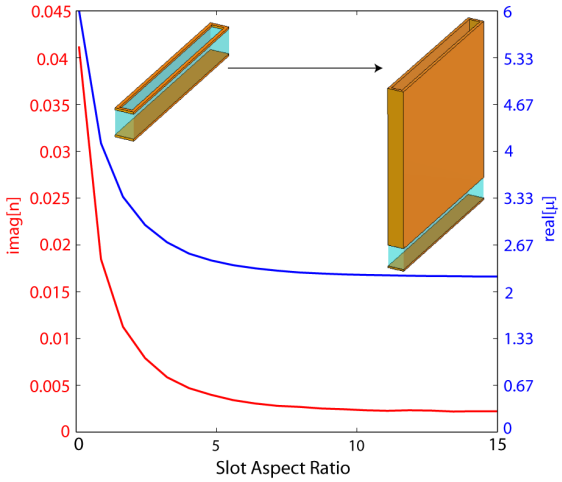

FIGURE 4.7: Simulation results for the radiation loss versus slot length of a cDipole. In the limit of an infinitely thick cDipole the imaginary component of the index of refraction goes to zero while the real part of the permeability approaches a non-zero value.

be excited by the transmission line signal[112]. By controlling the type of radiator (electric or magnetic) and its resonance frequency, the radiation mode of a single CM element and the frequency dispersion of that mode can be controlled (Fig. 4.3). A complementary ELC with Lorentzian polarizability α excited by a waveguide field $\mathbf{H}_{wg}$ has dipole moment,

$$\mathbf{m} = \alpha \mathbf{H}_{wg} = \frac{1}{\omega_0^2 - \omega^2 - i\omega\gamma} \mathbf{H}_{wg} \tag{4.1}$$

where ω_0^2 is the geometry-dependent resonance frequency of the cELC, and γ is the resonance damping rate. A dipole, when isolated, will radiate power,

$$P_{rad} \propto \omega^4 |\mathbf{m}|^2 \tag{4.2}$$

so the power radiated by a complementary metamaterial will be maximum at its resonance frequency, will vary with frequency as Lorentzian function magnitude-squared, and will be proportional to the power of the driving guided wave. This is exactly what is seen in Fig. 4.3.

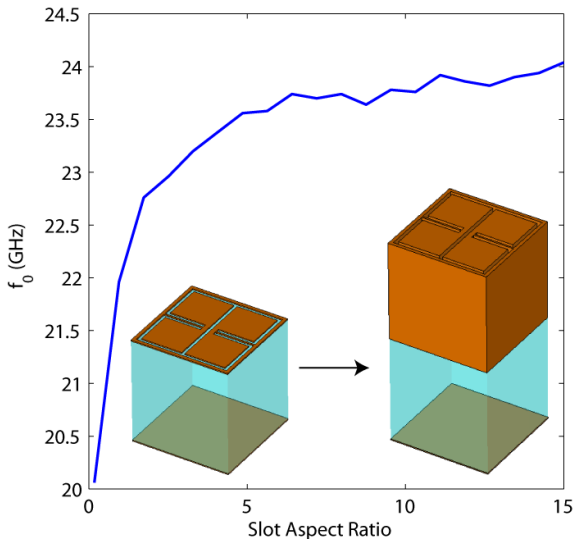

FIGURE 4.8: Simulation results for the resonance frequency versus slot aspect ratio for a resonant complementary ELC. The resonance frequency asymptotically blue-shifts with increasing slot length.

This would seem to indicate that complementary metamaterials should be very lossy due to radiation leakage and so would not be useful as effective materials. But we have already seen in Section 2.6 that complementary metamaterials can be used to provide an effective material loading without detrimental losses. To understand this apparent discrepancy, we need to understand how collections of complementary elements radiate. This will be discussed in Section 4.2.

The slots of the complementary metamaterials can be considered as waveguides that couple the guided modes of the transmission line to the free space modes above the transmission line. Depending on the modes supported by the slot, extending the length of the slot can decrease radiation losses. For example, in the simplest case of the complementary dipole the slot is just a rectangular waveguide with dimensions that put it well below the cutoff of the fundamental mode. All the modes supported in the slot are evanescent, thus increasing the length of the slot, or equivalently the thickness of the conductor through which the C-dipole is etched, decreases the field

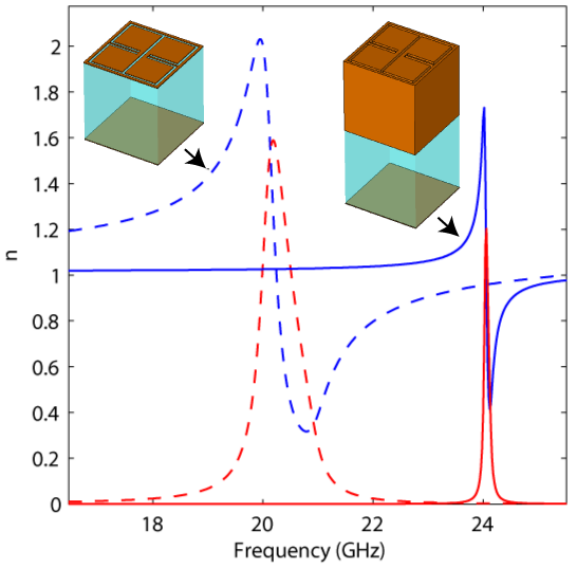

FIGURE 4.9: Dependence of resonance quality-factor on slot length. Increasing slot length reduces radiation loss and increases Q.

amplitude at the open side of the C-dipole slot and the coupling to the radiation modes is reduced. In the limit of an infinitely thick C-dipole the imaginary component of the index of refraction goes to zero while the real part of the permeability approaches a non-zero value (See Fig. 4.7).

For resonant structures, increasing the length of the slot also leads to a reduction in the radiation loss. This in turn leads to an asymptotic blue shift of the resonance frequency (Fig. 4.8) and an increase in the quality factor of the resonance (Fig. 4.9). The resonance shift and quality factor can both be explained by considering the equivalent circuit of the c-ELC a radiation resistance in series with an inductance both in parallel with a capacitance. The resonance frequency, defined as the frequency at which the impedance is purely real, of this RLC circuit is determined by,

$$Z = \frac{1}{R + j\omega L} + j\omega C = \frac{R}{R^2 + (\omega L)^2} - j\left(\frac{\omega L}{R^2 + (\omega L)^2} + \omega C\right) \tag{4.3}$$

$$Im\{Z\} = 0 = -\omega_0 \left(\frac{L}{R^2 + (\omega_0 L)^2} - C \right) \tag{4.4}$$

$$\frac{L}{C} = R^2 + (\omega_0 L)^2 \tag{4.5}$$

$$\omega_0^2 = \frac{1}{LC} - \left(\frac{R}{L} \right)^2 \tag{4.6}$$

and the Q-factor of the resonance is,

$$Q = \frac{1}{R} \sqrt{\frac{L}{C}} \tag{4.7}$$

The radiation resistance is relatively small compared to the inductance and capacitance and the blue shift in the resonance is not fully explained by the reduction in radiation resistance. The majority of the resonance shift is in fact due to the change in inductance and capacitance of the structure as the geometry changes. To a first order approximation, the radiation resistance is proportional to the coupling to the radiation modes which is in turn proportional to the field amplitude at the free-space side of the slot, so $R = R_0 e^{-\alpha l}$. The capacitance can be described by a constant fringing field component, C_f, and a parallel plate component that is linearly proportional to the slot length, l, so that $C = C_f + C_0 l$. The inductance is inversely proportional to the slot length, $L = L_0/l$. Thus the resonance frequency varies with the slot length as,

$$\omega_0^2 = \frac{1}{L_0/l(C_f + C_0 l)} - \left(\frac{R_0 e^{-\alpha l}}{L_0/l} \right)^2 = \frac{1}{\frac{C_f L_0}{l} + C_0 L_0} - \left(\frac{R_0 l}{L_0} \right)^2 e^{-2\alpha l} \tag{4.8}$$

As the slot length goes to infinity, the resonance frequency asymptotically blue shifts to the limit $1/\sqrt{L_0 C_0}$ (Fig. 4.8). For the two structures discussed above, the complementary slot divides the conducting sheet in such a way that it remains electrically connected everywhere. For complementary structures which divide the

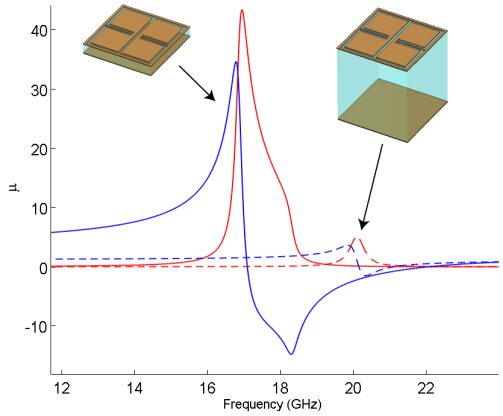

FIGURE 4.10: Controlling the oscillator strength by changing transmission line thickness. Changing the thickness of the dielectric layer separating the two conductors of the waveguide effectively changes the loading of the patterned complementary metamaterial. When the loading gets high enough, the effective index of the metamaterial becomes large. This results in the kinked Lorentzian indicative of spatial dispersion.

conducting sheet into multiple conductors there will be no cutoff to the fundamental modes supported inside the slots, such as parallel plate modes in infinite plasmonic wires or coaxial modes in some variations of the c-ELC. For these structures, the radiation loss will not limit to zero in the case of infinitely long slots.

The thickness of the transmission line substrate affects the loading density of the complementary metamaterials. The distance between the two conductors of the transmission line patterned with one- and two-dimensional complementary metamaterials is loosely analogous to the lattice constant of a bulk three-dimensional metamaterial since the top and bottom conductors act like fun-house mirrors, infinitely mirroring the patterned complementary metamaterial. Decreasing the substrate thickness decreases the effective lattice constant in that direction and increases the effective loading of the transmission line. The resulting increase in the guided mode index also increases spatial dispersion effects. By decreasing the thickness of the transmission line substrate from suitably thick to suitably thin, the dispersion

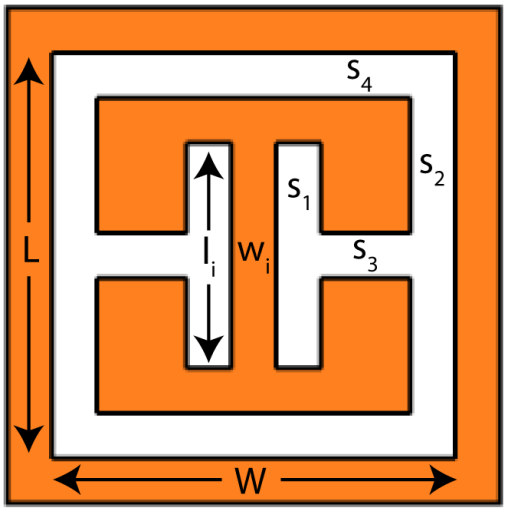

Units in mm and GHz

$$W = 1.3$$
$$L = 2.2$$
$$l_i = -0.071 \times f_0 + 2.8$$
$$w_i = -0.0023 \times f_0^2 + 0.1032 \times f_0 - 0.995$$
$$s_1 = (0.0057702 \times f_0^2 - 0.25646 \times f_0 + 3.2216)/2$$
$$s_2 = 0.075$$
$$s_3 = 0.075$$
$$s_4 = (2.2 - 2 \times 0.075 - l_i)/2$$

FIGURE 4.11: A K-band cELC design optimized for high quality factor and low coupling efficiency between the incident waveguide signal and free-space radiation. This was the cELC design used in the 2D frequency-diverse metaimager presented in Chapter 6. Guy Lipworth in Dr. David Smith's group made this design.

of the constitutive parameters of a complementary metamaterial can be continuously varied from smooth Lorentzian to the kinked Lorentzian indicative of spatial dispersion (Fig. 4.10).

For the frequency dispersive metamaterial imaging systems discussed in Chapter 6 we need to have maximum quality factor and minimal radiation. This is because we want our radiation pattern to be as dispersive as possible, maximizing the number of measurement modes for a given bandwidth. We want to minimize the radiation because we need most of the energy incident on a resonator to pass it and excite the following resonators so that we have high aperture efficiency. We did a study to find the largest ratio of (quality factor)/(radiated energy) for each resonant frequency possible, and fit our results to obtain design equations relating the cELC geometry to desired resonance frequency. The resulting design is given in Fig. 4.11. This study was done for a canonical cELC embedded in a 1D microstrip aperture. The width of the cELC was constrained to be smaller than the microstrip (4.5mm) and the

length along the propagation direction to be 2.2mm. When we transitioned to the 2D aperture we used the same design. In both the 1D and 2D apertures the cELCs were separated by 0.566mm.

4.2 Metamaterial antenna radiation

The techniques described above for determining the radiation pattern of an antenna using the plane-wave spectrum approach requires that the field at the aperture of the antenna, or the plane-wave spectrum components themselves, be known. These fields can be calculated through full-wave simulation for sufficiently small or simple antennas. For very large antennas, such as we will consider for the imaging applications discussed below, we would like to have an analytical or semi-analytical approach to calculating the radiated modes.

A traveling-wave or leaky-wave antenna consists of a wave-guiding structure, that does not intrinsically radiate, to which openings or discontinuities, that do radiate, are introduced[113, 114, 115]. The most basic example of such a structure is a rectangular waveguide with a slot running along its length. The slot allows energy to leak from the guided mode of the waveguide into a free-space radiation mode. An alternative design replaces the uniform slot with a series of periodic openings. Besides a rectangular waveguide, any other type of guiding structure may be used where the guided mode phase velocity may be either fast ($\beta < k_0$) or slow ($\beta > k_0$). By controlling the geometry and/or period of the radiative elements a beam that radiates in any direction (between broadside and end-fire only for uniform/fast configurations) can be formed.

Inspired by the work of N. Kundtz of Kymeta Corporation we extend the concept of a leaky-wave antenna by introducing Complementary Metamaterials (CMs) as the radiative elements in a travelling-wave antenna. Using CMs allows the radiation efficiency of each individual element to be independently controlled. By selecting the

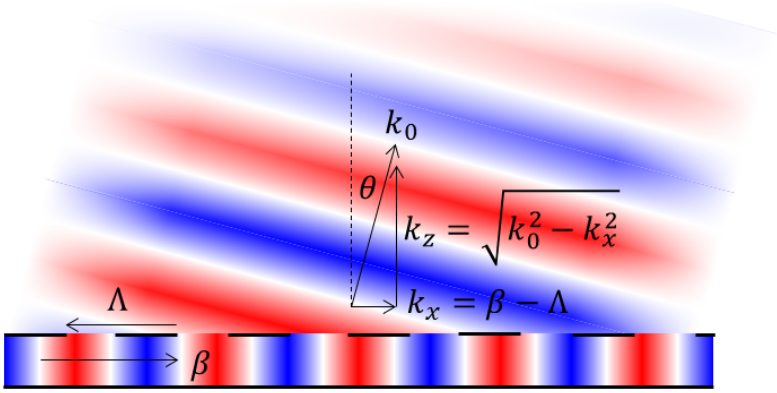

FIGURE 4.12: A cross-section view of a waveguide patterned with complementary metamaterials. The transmission line mode is a slow-wave with wavenumber $\beta > k_0$. If a modulation is introduced to the complementary metamaterials with spatial frequency Λ (represented by the dashed line in the top conductor of the transmission line), then the field just outside the transmission line waveguide has a transverse wavenumber given by the beat frequency between the waveguide mode and the complementary metamaterial modulation, $k_x = \beta - \Lambda$. This field excites a free-space plane-wave traveling with at angle $\theta = \tan^{-1}(k_x/k_z)$.

appropriate radiation efficiency of each element according to its position along the guiding structure, it is possible to create arbitrary radiation patterns in a manner similar to computer-generated holography (CGH).

To understand how complementary metamaterials can be used in leaky-wave antennas, consider a one-dimensional slow-wave transmission line with wavenumber $\beta > k_0$ that is patterned with complementary metamaterial radiators. We want to understand what happens when a modulation with spatial frequency Λ is introduced to the effective material properties, resonance frequency, or any other property of the metamaterial distribution.

The transmission line guided mode is given by $Ae^{-i\beta x}$. Then a homogeneous complementary metamaterial distribution will leak a field $Ae^{-i\beta x} \cdot B$ out of the transmission line. Introducing a sinusoidal modulation with spatial frequency Λ to the complementary metamaterial distribution results in a leaked field $Ae^{-i\beta x} \cdot (B + C\cos(\Lambda x))$.

This leakage field can be decomposed into three terms,

$$E_{leak} = AC/2e^{-i(\beta-\Lambda)x} + AC/2e^{-i(\beta+\Lambda)x} + AB/2e^{-i\beta x} \tag{4.9}$$

This is the field just outside the transmission line. This field will excite free-space planewaves that are phase matched to this field. The wavenumbers perpendicular to the transmission line of the excited planewaves are given by $k_z = \sqrt{k_0^2 - k_x^2}$, where k_x is the wavenumber of each of the terms in Eqn. 4.9. k_z is always imaginary for the last two terms in Eqn. 4.9, thus only the component of the leaked field corresponding the the first term can ever excite a propagating planewave. This planewave has transverse wavenumber $k_x = \beta - \Lambda$ and travels at an angle $\theta = \tan^1(k_x/k_z)$ from normal, as shown in Fig. 4.12. When $|\beta - \Lambda| > k_0$, k_z is imaginary, the structure does not radiate into free-space. If the modulation in the complementary metamaterials has a spectrum of spatial frequencies $S(\Lambda)$, then the radiation from the transmission line is composed of a spectrum of plane waves. The radiated field at any location is given by the superposition of all the radiated planewaves,

$$E(\mathbf{r}) = \int S(\Lambda) e^{-i\mathbf{r}\cdot(k_x(\Lambda)\hat{x} + k_z(\Lambda)\hat{z})} \tag{4.10}$$

Even homogeneous complementary metamaterials introduce some modulation to the leaked field simply by virtue of the patterning of the elements themselves. However, the lattice constant of a metamaterial needs to be at least ten times smaller than the guided-mode wavelength to be homogenizable. This means that the modulation of the complementary metamaterials themselves should be at least $\Lambda_{metamaterial} \geqslant 10\beta$ to be a true homogenizable metamaterial. In this case, $|\beta - \Lambda_{metamaterial}|$ is certainly greater than k_0. This explains how complementary metamaterials can used for transmission line loading without introducing radiative losses. The radiated planewave direction versus Λ is given in Fig. 4.13.

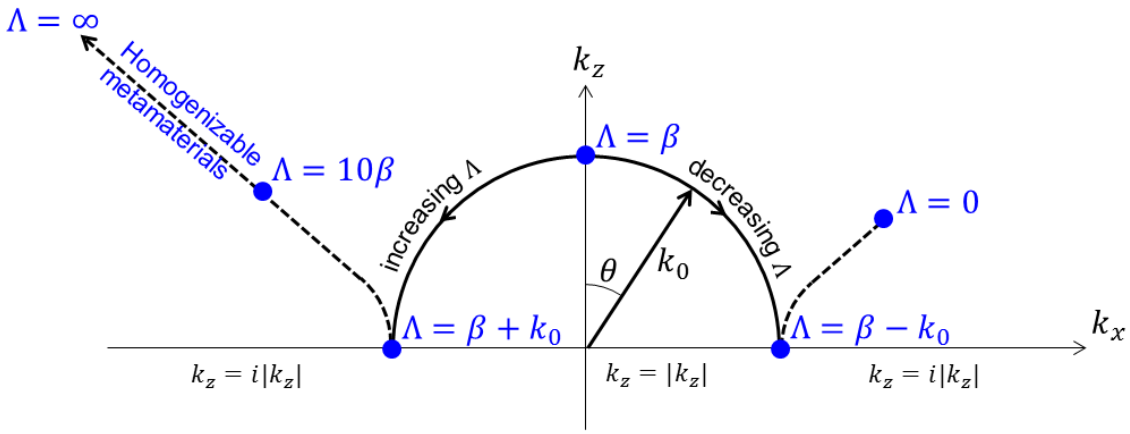

FIGURE 4.13: Diagram describing the direction of the planewave radiated by a complementary metamaterial leaky-wave antenna versus the spatial modulation frequency of the metamaterial pattern. The dashed lines indicate where k_z is imaginary and the antenna will not radiate. To make a leaky-wave antenna capable of radiating a planewave in any direction, it must be able to achieve direct back-fire ($\theta = -90^o$). At back-fire, the modulation of the leaked field must have a large spatial frequency of $\beta + k_0$. If the effective index of the guided wave is $n > 1$, this is $k_0(1 + n)$. To prevent aliasing, the modulation should be sampled at least twice per period. This means that if discrete radiators are used, they must be have a period of at least $\lambda/(2(1 + n))$. The small electrical size of metamaterial radiators makes them ideally suited to providing this rapid modulation.

A complete description of the radiation of such leaky-wave structures should consider several additional factors. For instance, the finite size of any antenna modifies the spectrum of the spatial modulation of the surface. Specifically, abruptly truncating the aperture introduces a sinc distribution to the spatial frequency spectrum. The high-order lobes of the sinc function result in the side-lobes seen in the radiation pattern of any finite aperture. Additionally, as energy is radiated along the length of the transmission line, the guided mode looses energy. In the simplest case, this energy loss is exponential and can be included in the model by modifying the guided wave to include this exponential decay as $Ae^{-i\beta x}e^{-\alpha x}$.

While the idea of varying the coupling efficiency of radiators along the length of a traveling-wave antenna is not new, using CMs is, and this approach provides several

advantages over other techniques[112]. Firstly, the substantially sub-wavelength size of CM elements allows the radiation efficiency to be relatively smoothly controlled over sub-wavelength length scales, which is essential for high-efficiency amplitude-only holographic mode forming. Secondly, some CM structures can be electrically tuned allowing for dynamic reconfiguration of the radiating mode. Thirdly, and of particular utility to our current designs, the highly dispersive nature of resonant CM structures causes the radiation mode to vary rapidly with frequency (frequency mode dispersion).

Being non-uniform, this type of traveling-wave antenna does not suffer from the limited scan range of uniform traveling-wave antennas. Being potentially non-periodic, a meta-antenna can produce arbitrary radiation modes in addition to simple beams. The strong frequency dispersion of the radiation coupling efficiency of resonant CMs also allows for stronger mode dispersion with frequency (frequency scanning in the nomenclature of travelling-wave antennas) than a traveling-wave antenna with non-resonant radiating elements.

When the frequency dispersion of metamaterial resonators is considered, radiation patterns vary with frequency, such as the random far-field pattern shown in Fig. 6.2, may be designed.

An equivalent alternative description of the radiation of a complementary metamaterial antenna can be obtained by considering the Fourier transformation of the model given above. This is an array factor calculation in which the field at any point in space is obtained by adding the contributions of each individual metamaterial radiator. We may describe the antenna as being composed of a sheet of metamaterial radiators which are excited by some mode generated by the antenna's source (or detector, depending on whether we are considering the antenna as operating in a transmit or receive modality. Due to the reciprocal nature of the forward model, the operation modality is not important in this context). These radiators then each

re-radiate the source mode with some new amplitude and phase. The radiated field at frequency f_m at position r_n in front of such an aperture is given by,

$$E(f_m, r_n) = \sum_{p=1}^{P} S(r_p, f_m) A(r_p, f_m) G(r_n - r_p, f_m) \frac{k}{4\pi |r_n - r_p|} e^{-i2\pi \frac{f_m}{c} |r_n - r_p|} \quad (4.11)$$

where r_p is the position of the p^{th} radiator on the aperture, $S(r_p, f_m)$ is the mode of the antenna source, $A(r_p, f_m)$ is the complex coupling efficiency of the metamaterial radiator, and $G(r_n, f_m)$ is the radiation pattern (gain) of the radiators.

For example, if the aperture consists of a thin slab of resonant metamaterial electric dipoles illuminated by a horn then the source mode is,

$$S(r_p, f_m) = G_{horn}(r_p, f_m) e^{-i2\pi \frac{f_m}{c} |r_p|} \quad (4.12)$$

where G_{horn} is the horns gain pattern. The coupling efficiency is,

$$A(r_p, f_m) = \left(\omega_0^2(r_p) - \omega_m^2 - i\gamma(r_p)\omega_m\right)^{-1} \quad (4.13)$$

which is the polarizability of a dipole with resonance frequency ω_0 and damping γ. Finally, the radiation pattern of the dipoles is,

$$G(r, f_m) = i\sqrt{\frac{\mu}{\epsilon}} sin(\theta)\hat{\theta} \quad (4.14)$$

The formation of these radiation modes scan be understood from a holographic perspective, where $S(r, f)$ is the reference mode, the metamaterial aperture described by $A(r_p, f_m)$ is the hologram which transforms the reference mode into the desired 'holographic image', $E(f_m, r_n)$. In the terminology of holography, the excitation signal is the reference wave and the array of metamaterial resonators is the hologram. The metamaterial hologram adds some phase and amplitude distribution to the reference wave such that the resulting radiated wave is the desired mode.

The idea of holographic imaging system can be extended to include guided-wave structures by replacing the free-space propagation between the metamaterial hologram and the detector array with a waveguiding structure, as depicted in Fig. 1.1C. This allows the device dimensions to be substantially reduced. In such a scheme, the metamaterial elements would serve two functions, to add a spatially-varying phase advance to the incident wave as well as to couple the incident radiation into (or out of, depending on whether the device is being used as a receiver, transmitter or transceiver) the waveguide. The waves would then be guided to one or more detectors embedded in the waveguiding structure.

4.3 Conclusions

The complementary metamaterials presented here have interesting applications to antenna design. Not only do they provide a method of controlling the radiation traveling through a transmission line, acting as filters and effective material loadings, but they also can control how radiation leaks out of a transmission line. This makes them interesting components for antennas with small form-factor and signal-multiplexing capabilities. By designing complementary metamaterial radiators that have different responses to different frequencies, polarizations, or other properties of radiation, then an antenna that can multiplex signals on these different channels can be formed.

The model presented here for the radiation of a metamaterial aperture gives accurate results when the coupling efficiency of the aperture and the reference mode are known. However, when the metamaterial radiators are very close together, they may couple in ways that make determining their collective response difficult and so determining the coupling efficiency of the aperture is also difficult. In addition, if the reference mode is a guided mode, as is the case for an aperture composed of complementary metamaterial radiators patterned on a transmission line, then

the metamaterial elements will scatter the guided mode making it non-linear with respect to the aperture configuration. Work by others to address these problems using discrete-dipole-approximation methods is ongoing and the solution of this problem is essential to create engineered radiation patterns.

5

Experimental Tools

An alternative to semi-analytical approaches to determining the radiation modes of an antenna is to measure the modes experimentally. Two approaches to experimental antenna characterization are described below.

5.1 Far-field antenna characterization

As described in section 3.4, the far-field radiation pattern of an antenna varies with range only with a $e^{-ik_0 r}/r$ dependence. The far-field is defined by the Fraunhofer distance which is,

$$R_{Fraunhofer} = (2A^2)/\lambda \tag{5.1}$$

where A is the largest dimension of the aperture. The only mode of an antenna that is present at a given direction in the far-field is a plane wave traveling in that direction. Thus, if two antennas are in each others far-fields, then the signal transmitted between them is proportional only to the magnitude of the product of their plane-wave spectrum components that travel in the direction between the two antennas. The antennas radiation patterns in other directions besides the direction directly

between the two does not affect the measured signal.

This means that the far-field radiation pattern, $E_{far}(r, \theta, \phi)$, of an antenna under test (AUT) can be measured by placing a receiving antenna in the far-field of the antenna under test and measuring the signal between them for every orientation (θ, ϕ) of the antenna under test, while keeping the orientation of the receiving antenna fixed. The signal measured for each orientation of the antenna under test will then be proportional to $E_{far}(r, \theta, \phi)$. Once the far-field of the antenna under test is known, the plane-wave spectrum components can be obtained from Eqn. 3.71, and the fields everywhere radiated by the antenna under test can be calculated.

Here it should be noted that the far-field radiation mode of an antenna is commonly represented in units of dBi, decibels with respect to the power per unit area that an isotropic radiator radiating the same total power would radiate. This is calculated as,

$$G_{dBi}(\theta, \phi) = 10log_{10}\left(\frac{U}{\frac{P_{radiated}}{4\pi}}\right) = 10log_{10}\left(4\pi\frac{E_{far}^2(r_0, \theta, \phi)}{\int_0^{\pi/2}\int_0^{\pi} E_{far}^2(r_0, \theta, \phi)sin(\theta)d\theta d\phi}\right) \tag{5.2}$$

The coordinate system often used to present such radiation patterns is often the elevation-over-azimuth coordinate system, which is an alternative to the more common polar spherical coordinate system. In this coordinate system, the azimuth angle (Az) is measured away from the z-axis (optical axis of the antenna) in the xz-plane, and the elevation angle (El) is measured normal to the xz-plane. This coordinate system is convenient because it corresponds to the motion of most angular gimbal positioning systems.

We have built such a system, shown in Fig. 5.1, for the purpose of characterizing metamaterial imaging antennas. The receive horn for the far-field scan was a 20dBi standard-gain WR-42 horn antenna located at 2.85 meters from the antenna under

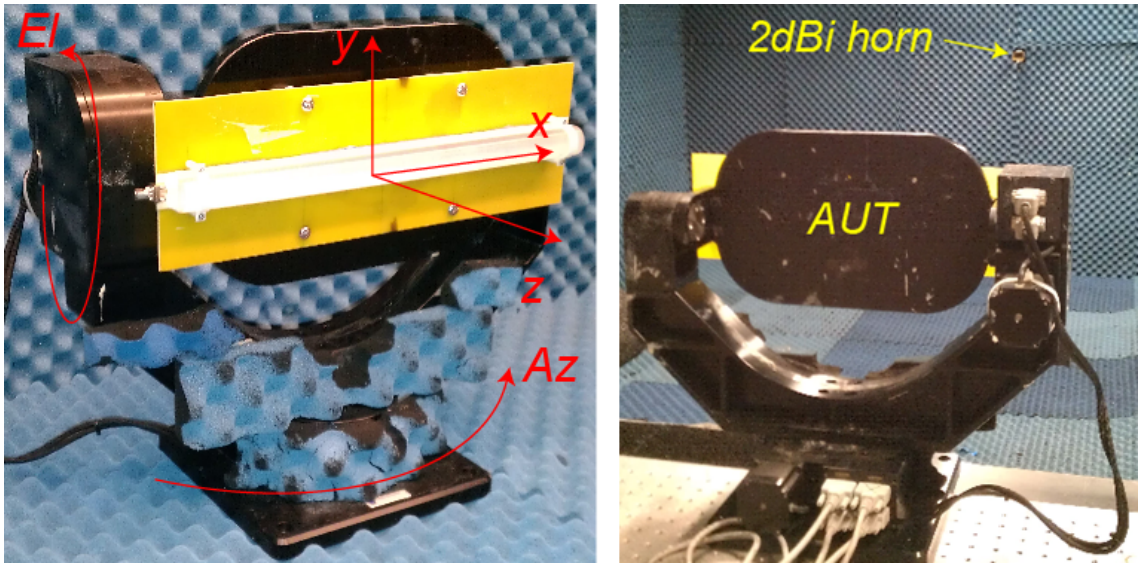

FIGURE 5.1: Far-field antenna characterization setup.

test. The antenna was mounted on a 2-axis elevation-over-azimuth gimbaled positioning stage. An Agilent E8364B vector network analyzer (VNA) was used to feed the antenna under test and to measure the scattering-parameters at the receive horn across all frequencies of interest for each antenna orientation. The stage and VNA were controlled with Matlab.

5.2 Near-field antenna characterization

For large, heavy, or fragile antennas, characterizing the antenna by far-field characterization may be impractical due to the need to rotate the antenna. An alternative approach developed in the 1960s and gaining in popularity with the increasing computational power available to researchers, is near-field characterization. In a near-field characterization setup the antenna under test remains stationary while a field probe is scanned across a planar, cylindrical, or spherical surface around the antenna. The field probe measures two orthogonal polarizations of the near field tangential to the measurement surface. These fields are then used to calculate the field radiated

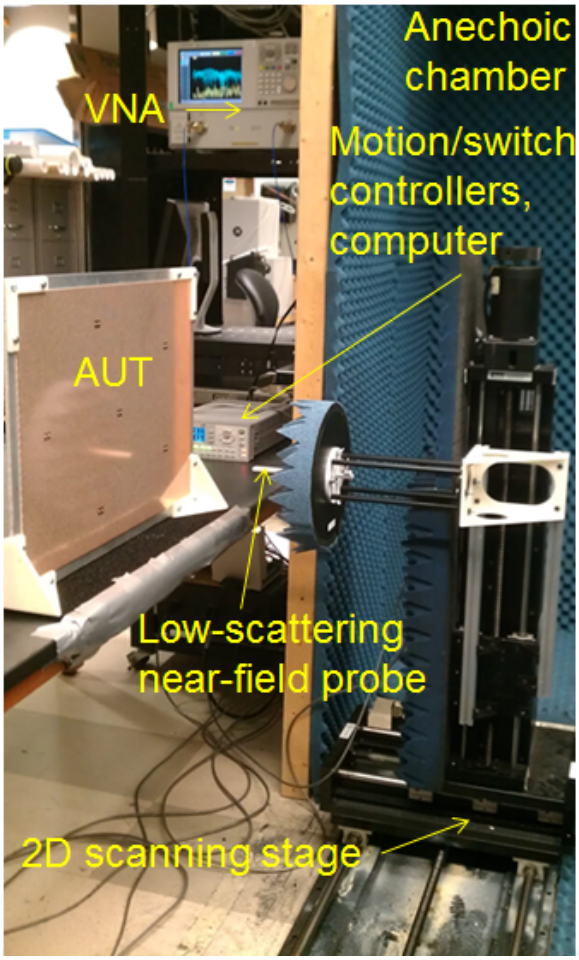

FIGURE 5.2: Near-field antenna characterization setup.

from the antenna using Fourier optics[116]. We have built such a system, shown in Fig. 5.2, for the purpose of characterizing metamaterial imaging antennas.

These probe measurements must not be in the reactive near-field where evanescent waves are present as this would allow for the probe to couple to the antenna through the evanescent waves and modify its response. For most antennas, five wavelengths is far enough for the evanescent waves to decay. Furthermore, the probe must have low scattering back toward the antenna to prevent higher-order reflections between the antenna and the probe from being measured.

In section 3.4 we showed that the scalar field radiated from a 1D aperture can be

found from the field across the aperture as,

$$E(x,z) = 1/2\pi FT^{-1}\left\{FTE_a(x)e^{-i\sqrt{k_0^2-k_x^2}z}\right\} \tag{5.3}$$

This can be easily extended to vector fields radiated from a 2D aperture by taking the 2D Fourier transforms of the aperture field. Because the Fourier transform is a linear operation, each of the vector components can be handled independently so the vector field radiated is,

$$\mathbf{E}(x,y,z) = 1/(4\pi^2)\iint_{-\infty}^{\infty}\mathbf{A}(k_x,k_y)e^{-j(k_xx+k_yy+k_zz)}dk_xdk_y \tag{5.4}$$

$$\mathbf{E}(x,y,z) = FT^{-1}\left\{\mathbf{A}(k_x,k_y)e^{-jk_zz}\right\} \tag{5.5}$$

where $\mathbf{A}(k_x,k_y) = FT\left\{\mathbf{E}(x,y,0)\right\} = FT\left\{E_x(x,y,0)\right\}\hat{\mathbf{x}} + FT\left\{E_y(x,y,0)\right\}\hat{\mathbf{y}} + FT\left\{E_z(x,y,0)\right\}\hat{\mathbf{z}}$. This expression can be efficiently evaluated using the Fast Fourier Transform (FFT).

In a near-field scan only the two orthogonal field components tangential to the measurement surface are measured. For a near-field scan made on the xy-plane with the antenna directed long the z-axis, the measured tangential field is, $\mathbf{E}_t = E_x\hat{\mathbf{x}}+E_y\hat{\mathbf{y}}$. The unmeasured z-component of the aperture field can be found from the plane wave condition that $\mathbf{k}\cdot\mathbf{E} = 0$ in freespace. This yields,

$$F_z(k_x,k_y) = -\frac{\mathbf{k}_t\cdot\mathbf{F}_t(k_x,k_y)}{k_z} \tag{5.6}$$

The accuracy of a near-field scan in predicting the radiation pattern of an antenna is related to the proportion of radiated power that passes through the scan surface. This means that a planar near-field scan is only suitable for high-directivity antennas or for large area antennas. Cylindrical and spherical near-field scan geometries are possible but are more difficult to implement mechanically. The antennas we have

characterized with this system are large-area planar antennas and so are amenable to a planar scan geometry. This power capturing requirement is often captured in the rule-of-thumb that the far-field pattern calculated from a near-field scan may be trusted only out to an angle from the center of the antenna that is equal to the angle from bore-sight that is made between the edge of the antenna and the edge of the scan region. This is especially important if determination of side-lobe levels and null-depth are important. This means that the radiation pattern calculated from a near-field scan that just covers the area of the antenna would be valid to an angle of 0^o from bore-sight, i.e. only along a single ray. Fortunately the near-field scan can be made very close to the antenna surface, so long as the probe is out of the reactive near-field of the antenna, so a planar near-field scan that extends only a few wavelengths beyond the edge of the antenna can validate a large field-of-view. The probe for the near-field scan was an open-ended WR-42 waveguide (0.42"x0.17") with a cutoff frequency of the fundamental mode of 14.051GHz and a cutoff frequency of the next higher order mode of 28.102GHz) with a 10^o beveled opening to reduce energy scattered back toward the antenna. The open-ended waveguide has a relatively low-gain radiation pattern which is ideal for a near-field characterization system so that all plane-wave components are sampled with high SNR. If the gain of the probe used is not flat across the radiations angles of interest, it is necessary to correct the amplitude of the measured plane-wave components to account for the non-uniform gain of the probe. This probe-correction was not performed for the near-field scans we have made. The probe was mounted on a 2-axis translation stage with a 0.7x0.7m maximum scan area. An Agilent N5245A vector network analyzer (VNA) was used to feed the antenna under test and to measure the scattering-parameters at the probe across all frequencies of interest for each probe position. The stage and VNA were controlled with Matlab.

5.3 Conclusions

The quality of images produced by a computational imaging system is limited by the accuracy of the forward model. For a microwave imaging system, this places a large burden on the quality of the antenna characterization. For this reason the far-field and near-field characterization systems presented here represent a quality-bottleneck for the imaging systems presented in Chapter 6. Our tests of known antennas with these systems show very good agreement.

6

Frequency-Diverse Metamaterial Imager

At this point we have given an overview of computational imaging, developed the forward model for coherent imaging from an arbitrary radiating aperture, and described the experimental techniques to characterize the radiation pattern from such an aperture. We now describe the design and testing of an actual metamaterial imaging system.

Imaging systems for radio frequency and millimeter-wave electromagnetics have generally been of two types: scanned single pixel systems, and multi-element phased-arrays (or synthetic phased arrays). The measurement modes used by classical single pixel systems are typically inefficient at collecting imaging data. A raster-scanned beam, for instance, collects information about only one point in space at a time. Multi-element phased array systems have much more flexibility in the measurement modes they can produce, but sacrifice the size, weight, power, and price advantages of single-pixel systems.

With an antenna that can either be mechanically, electrically, or frequency scanned across a scene, it is possible to perform imaging. This is of course the technique used in the radio and microwave frequency ranges for radar. An electrically tuned antenna

could do this with no moving parts. The goal of the work described in this section was to use metamaterials to design such an electrically scanned antenna that used only a single, frequency-sensitive, coherent detector to preform imaging. We refer to this device as a metaimager. As described in section 3.3, the measurement matrix of our metaimager is given by the normalized far-field squared if the antenna is used in a monostatic measurement, or the product of the metaimager far-field and a secondary antenna far-field in a bistatic measurement. The metaimagers far-field is designed to vary strongly with frequency, and thus so will the rows of the measurement matrix, creating a diversely sampled scene.

Antenna designs exist that have radiation modes that vary with frequency, however, existing implementations have focused on beam scanning with frequency and do not have sufficient diversity of modes to be useful for 2D imaging applications. Instead, we look at highly dispersive metamaterial radiators that produce radiation modes that vary rapidly with frequency. This is achieved by forming an array of resonant metamaterial elements that radiate light proportional to their excitation. All these antennas are excited with the same signal such that for any given frequency, a different sub-set of antennas is radiating and a different radiation mode is formed. Ideally, these radiation modes may be tailored to the type of scene being imaged. Rapid frequency variation and high diversity of modes reduces the bandwidth needed by the antenna to image a scene, so we seek resonators with high quality factor. Since the measurements are frequency-multiplexed, only a single detector of sufficient bandwidth is needed. This is particularity useful in the millimeter to far-IR ranges where detectors are prohibitively expensive. Because it is possible to create radiation modes that sample all parts of a scene, no mechanical scanning is needed. In this configuration, fully three-dimensional (3D) images can be collected by measuring phase and/or time of flight.

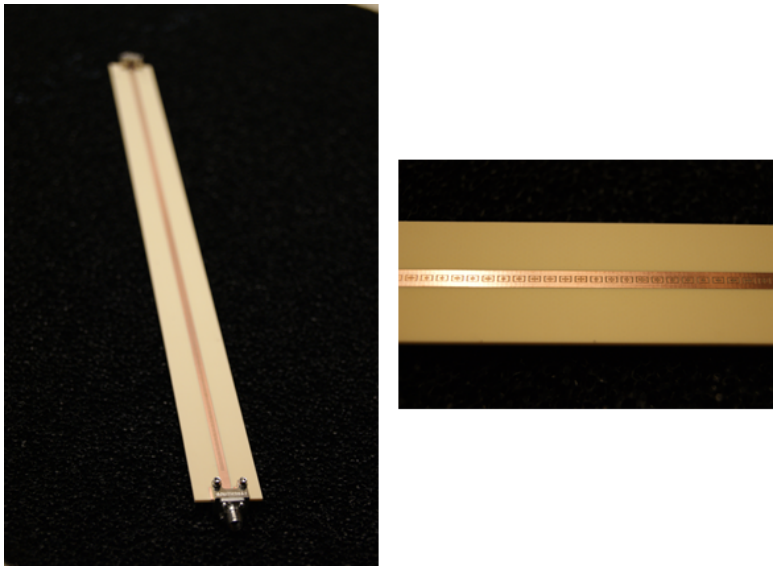

FIGURE 6.1: The fabricated 1D metaimager. The length is 40cm and the width is 2.5cm. The microstrip transmission line is patterned on top of a Rodgers 4003 hydrocarbon/ceramic microwave laminate. The microstrip has a width corresponding to an impedance of 50Ohms. The microstrip is patterned with cELCs with a period of 2.6mm. One end on the transmission line serves as the signal input and the other is terminated with a 50Ohm broadband load.

6.1 One-dimensional aperture

By leveraging metamaterials and compressive imaging, a low-profile one-dimensional aperture capable of microwave imaging without lenses, moving parts, or phase shifters has been demonstrated. This designer aperture allows image compression to be performed on the physical hardware layer rather than in post-processing, avoiding the detector, storage, and transmission costs associated with full diffraction-limited sampling of a scene. A guided wave metamaterial aperture was used to perform compressive image reconstruction at ten frames per second of a two-dimensional (range and angle) scenes at K-band (18-26 GHz) frequencies, using frequency diversity to avoid mechanical scanning. Image acquisition was accomplished with a 40:1 compression ratio[117].

We use a one-dimensional metamaterial aperture to perform compressed imaging

of various two-dimensional (one-angle plus range) canonically-sparse scenes. Our imaging device consists of a leaky waveguide, formed by patterning the top conductor of a standard microstrip line with complementary electric-inductor-capacitors (cELCs)[110, 118] metamaterial elements (Fig. 6.1). This configuration is equivalent to the schematic of the compressive imager in Fig. 1.1C except that the aperture becomes one-dimensional. Each cELC acts as a resonant element that couples energy from the waveguide mode to free space. The center frequency and spectral shape of the cELC control the amplitude and phase of the transmitted wave, such that the far-field modes can be designed by modifying the geometry of the cELCs along the microstrip. By controlling the design and distribution of the individual elements, which impact both the scattered field characteristics as well as the guided wave characteristics, nearly any desired aperture mode can be created.

For canonically sparse scenes, an efficient set of measurement modes are those that distribute energy randomly across both the amplitude and phase space of the scene. The dispersion present in resonant metamaterial elements makes frequency a natural choice for the indexing the modes, creating a mapping between the measurement modes and frequency. Thus, by sweeping the frequency of the illuminating signal across the available bandwidth, we access the aperture modes sequentially, without having to move or reconfigure the aperture. Essential to image reconstruction schemes that use an arbitrary set of measurement modes is that the modes be as orthogonal as possible to each other. This places demands on the sharpness (quality-factor) and separation of the resonances, with sharper resonances yielding less correlated modes.

We have fabricated a random-mode metamaterial aperture, 40cm in length, designed to operate in the K-band from 18.5-25 GHz. The cELC resonators that cover the aperture were optimized in full-wave simulation to have a high-quality factor and low radiation coupling efficiency. Three samples of the measurement modes for

FIGURE 6.2: Log-scale farfields radiated by a 1D metamaterial antenna. These antennas show rapid changes in the radiation pattern versus frequency over a large bandwidth.

this design are plotted in Fig. 6.2, and the complete measurement matrix is plotted in Fig. 6.3. This measurement matrix was experimentally characterized using the far-field characterization techniques in section 5.1. In our demonstration, scenes are illuminated by far-field radiation from a single source — a 20dBi standard gain horn antenna. Backscattered radiation from objects in the scene floods the metamaterial aperture, which selectively admits only one specific mode at each measured frequency. The resulting (complex) signal is measured using a vector network analyzer.

We formed several simple sparse scenes inside a 4m×4m×3m anechoic chamber. Each scene contained two or three scattering objects (retroreflectors), 10cm in diameter, located at arbitrary positions in the chamber. Fig. 6.4B shows one such scenes. All scenes were reconstructed using the TwIST[101] with the same regularization parameter for each scene. Four measured and reconstructed scenes are shown in Fig. 6.4A.

For an aperture of this size and bandwidth, the diffraction-limited angular resolution is 1.7^o and the bandwidth-limited range resolution is 4.6cm. Across a field of view of $\pm 70^o$ in angle and 1.5-4m in range, the equivalent SBP = 4475. Our measurement however, contains only 101 values representing a compression ratio of more than 40:1. We note that the acquisition of a complete dataset for the scenes in Fig. 6.4 requires only 100 milliseconds, which makes imaging moving scenes a

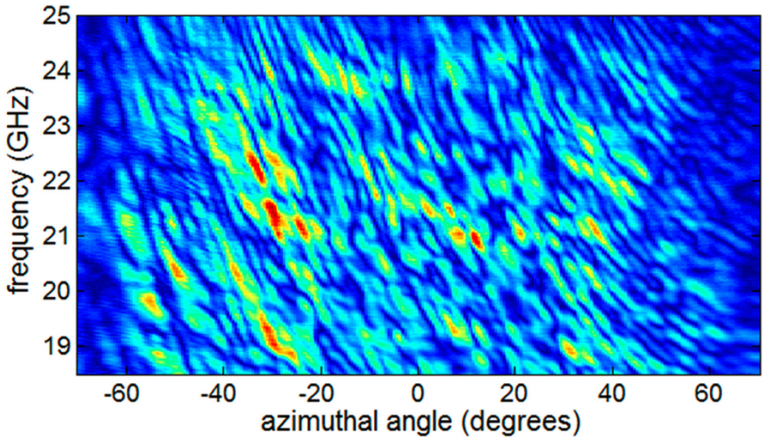

FIGURE 6.3: Experimentally measured far field radiation pattern versus frequency for a random 1D resonator array. A resonator array with random resonance frequencies will produce a far-field that is random and varies rapidly with both observation angle and frequency. A single horizontal slice of this plot corresponds to the far field amplitude measured along an arc contained in the same plane as the array. When represented in this manner, the far-fields vs frequency plot (or its square if used as a transceiver) is equivalent to the measurement matrix, $\mathbf{H}$, in the equation $\mathbf{g} = \mathbf{H}\mathbf{f}$, where $\mathbf{f}$ is the scene being measured and $\mathbf{g}$ is the measured data.

tantalizing possibility.

To demonstrate imaging of moving scenes, we performed repeated 100ms sweeps while moving an object through the scene. The acquisition speed in this experiment was limited by the signal-to-noise-ratio — primarily due to the network analyzer which is designed for operational flexibility rather than for high dynamic range or sweep speed. We image a single scattering object moving through the scene on a linear path at 0.2m/s. Fig. 6.5 depicts the reconstructed scene. The object position in angle and range, mapped as a function of time, is observed in the retrieved scene.

The imaging system we have presented combines a computational imaging approach with custom aperture hardware that allows compression to be performed on the physical layer used to do the illumination and/or recording. The use of metamaterials is a convenient tool for the creation of such apertures, as metamaterial

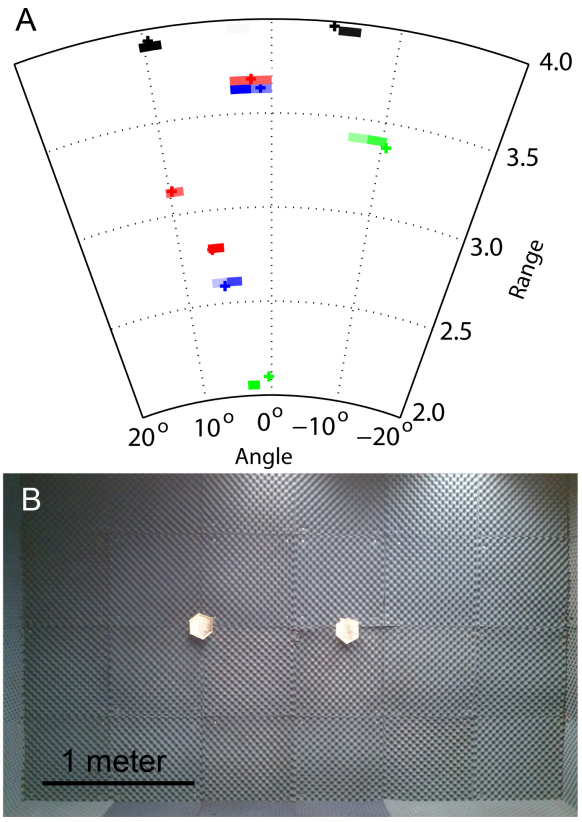

FIGURE 6.4: (A) Reconstructions of four different static scenes (differentiated by color), consisting of two (black, green, and blue) or three (red) 10cm scattering objects. The solid "+" show the actual location of objects, and the pixels show the reconstructed image. Pixel size reflects the maximum instrument resolution. The image has been cropped from the full field of view of $\pm 70^o$. (B) Photograph of a single scene corresponding to the black markers in (A).

techniques offer a well-understood design path. Leveraging the resonant nature of metamaterial elements also creates frequency-diversity of the measurement modes, giving an all-electrical way to quickly sweep through a mode-set. This metamaterial approach scales linearly with frequency through THz frequencies with correspondingly higher resolutions. Due to their small form factor and lack of moving parts, similar systems may extend microwave and mm-wave imaging capabilities. This approach to antenna design will scale effectively from microwave to far-IR (THz) frequencies where single detectors schemes are especially appealing due to the high

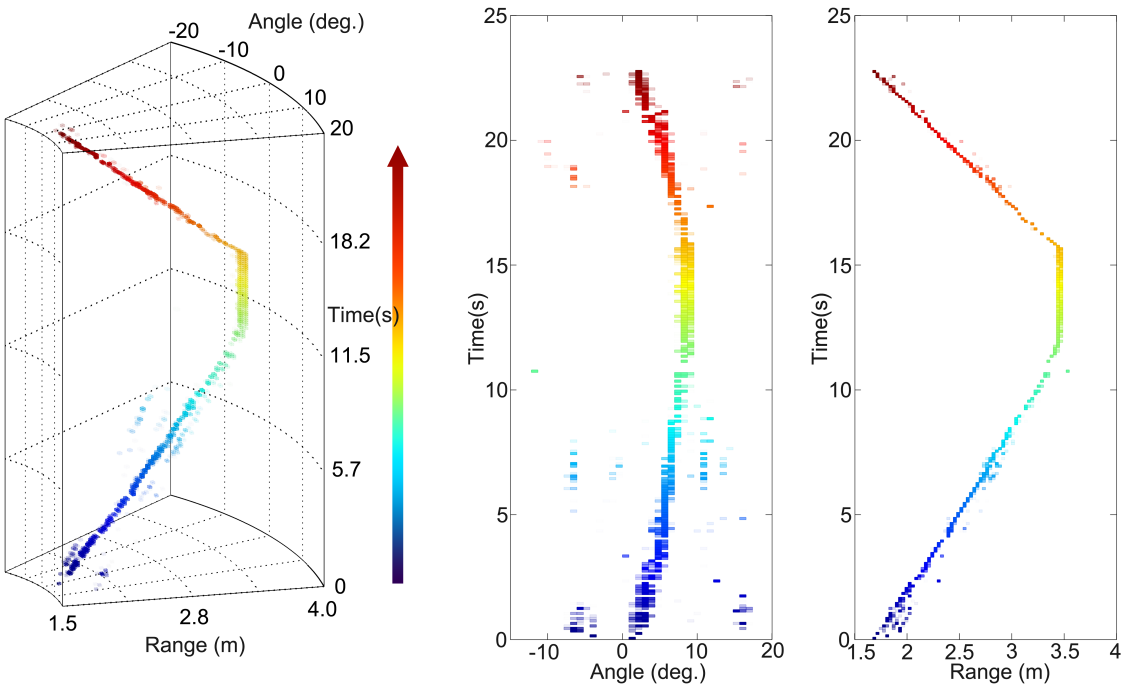

FIGURE 6.5: 10Hz imaging of a single moving object. Each voxel is sized to match the spatio-temporal resolution of the metamaterial aperture, and the amplitude of the reconstructed scattering density is mapped to the transparency of each voxel. Voxels are also color-coded in time, from blue to red. On the right are 2D projections of the data.

cost of individual sensors. By preforming imaging in a frequency region where materials of interest have distinct spectral responses, hyper-spectral imaging would be possible. By correlating this spectral information with known responses of materials, the positions and material compositions of objects in a scene could be identified.

6.2 Two-dimensional aperture

The previous work with complementary metamaterials embedded in 1D waveguides can be readily extended to 2D waveguides. While a one dimensional waveguide produces a one dimensional aperture capable of producing images in two dimensions (one dimension of cross-range and one dimensions of range), a two dimensional aperture (or an array of 1D apertures) produces a two dimensional aperture capable

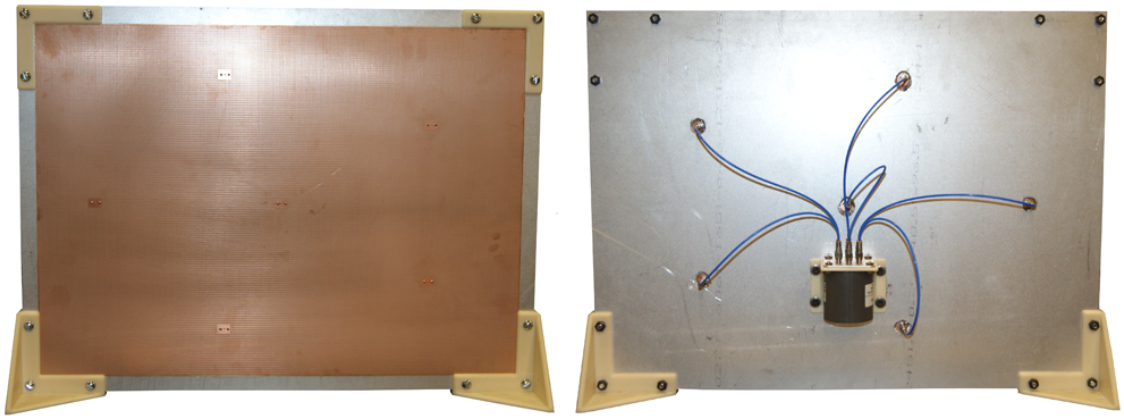

FIGURE 6.6: The front (Left) and back (Right) of the 2D metaimager aperture. The back view shows the six feed ports.

of producing fully three dimensional images. We chose to use a 2D parallel-plate waveguide over an array of 1D apertures for two reasons. Firstly, an array of one dimensional apertures would require a complex power dividing feed network, while a parallel plate can be excited from a single source. Secondly, a 2D parallel plate supports many modes which allows for an additional degree of freedom in how the aperture is excited. By placing a number of sources at different locations across the aperture, we may excite different modes in the aperture and thus generate different radiation modes. This allows us to increase the number of scene sampling modes produced by the same static aperture for the same bandwidth.

6.2.1 Aperture design

The operation bandwidth of the 2D metamaterial imaging system is the K-band, specifically 17.5GHz-26.5GHz. The 2D metamaterial aperture consisted of a copper parallel-plate waveguide, 22"x16" in area, with 1/16" between the plates. The boundaries of the parallel plates were then terminated with a via-fence to prevent radiation from leaking out of the open edges (Fig. 6.6). The top surface of the waveguide is patterned with 52,786 radiating metamaterial elements each with a Q

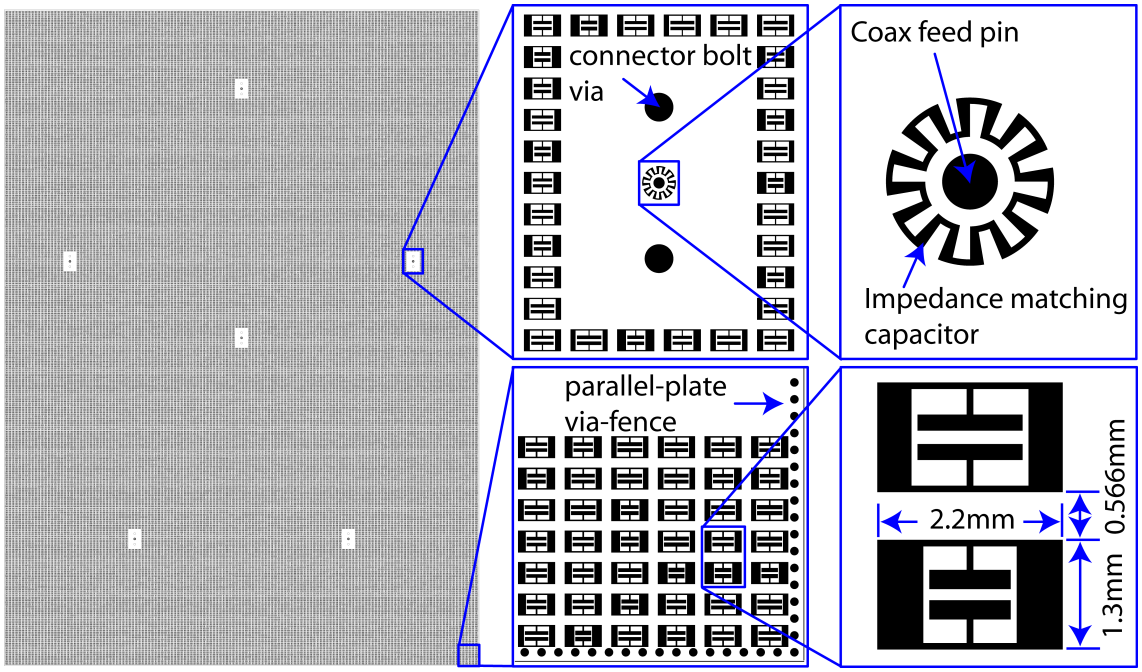

FIGURE 6.7: A schematic of the aperture used for the results presented here. The left most panel shows the full aperture and the middle and right panels show details with various features labeled. White is copper, black is dielectric (either Rodgers 4003 or air). The specific details of the cELC design used are used are given in Fig. 4.11.

of between 100 at 17.5GHZ and 130 at 26.5GHz. A parametric study was performed to optimize the Q of resonators with resonant frequencies across the operation bandwidth. Each resonator had a randomly selected resonant frequency within the operation range. As for the 1D aperture, each element is a complementary-ELC which couples to the magnetic field inside the aperture. We sample 101 frequencies across this bandwidth because the quality factor of our resonators limits the dispersion rate of the measurement modes. Thus, beyond approximately 100 frequency samples, we see diminishing returns in the scene information obtained per measurement while we accumulate noise linearly with the number of measurements.

An Agilent N5245A vector network analyzer (VNA) was used to feed the antenna under test and to measure the scattering-parameters at the probe across all

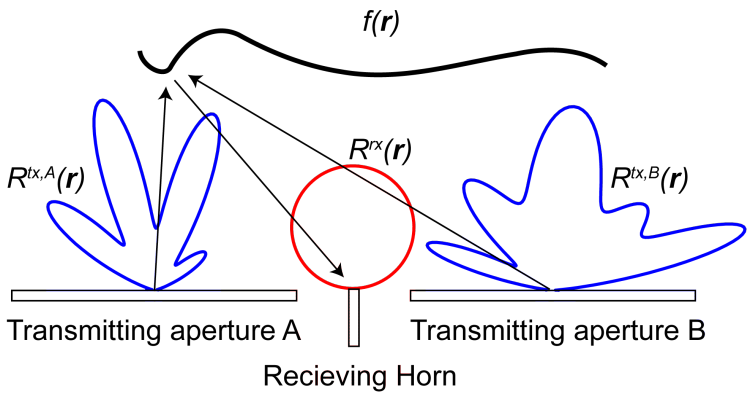

FIGURE 6.8: The aperture configuration used for the results presented here. Two metamaterial apertures (labeled A and B), side by side and co-planar, were used as the transmitters. A low gain (5dB) open-ended WR-42 waveguide was used as the receiver.

frequencies of interest. The signal generated by the VNA was sent to an Agilent L7106C electromechanical 6-port switch, and from this switch the signal was sent to ports on the metamaterial aperture. To couple the RF signal into the metamaterial-patterned parallel-plate, coaxial cables were probe-coupled into the parallel plate. These transitions required a non-standard coupling from a coax probe to a parallel-plate waveguide. Simply inserting a coax probe into the waveguide leads to an inductive impedance and thus high insertion losses. This inductive load was compensated for by etching a capacitive lumped element (designed in full-wave simulation) into the top plate of the waveguide, as shown in Fig. 6.7. The S-parameters of the input ports are all below -7.5dB for all ports and all frequencies, with an average of -14.5dB, indicating that the feeds are well matched (Fig. 6.9). The edges of the waveguide were shorted with a via fence, effectively creating a cavity. However, the large radiative losses from the metamaterial resonators leads to an extremely low Q cavity, and so lossy cylindrical waves, rather than cavity modes are expected. To increase the number of measurement modes, six individual feeds were used, with each feed being addressed by an electro-mechanical switch. To reduce the correlation between the

guided modes propagating inside the parallel plate the feed locations were placed far from each other.

6.2.2 Forward model characterization

Determining the radiation pattern of the metamaterial aperture is essential to generating a useful measurement matrix. The effects of coupling between adjacent metamaterial resonators make a simple array factor type calculation impossible, while the multiscale nature of the apertures makes full-wave simulation computationally intractable as well. Thus we chose to experimentally characterize the radiation from the apertures.

The size of this aperture and the complexity of the switching network makes far-field characterization challenging while the large and planar nature of the aperture makes it amenable to characterization by a planar near-field scan. So the radiation modes of this aperture were characterized using the near-field characterization methods of section 5.2. We have used a 5λ stand-off from the metamaterial antenna surface for our characterizations and a 5λ extent beyond the antenna edges, meaning the resulting radiation pattern is valid within $\pm 45^o$ in azimuth and elevation. This stand-off is somewhat larger than is required to mitigate evanescent field interaction, but also serves to reduce the effects of multipath scattering between the probe and the antenna. The field is sampled across a plane located at five times the lowest frequencys wavelength (8.57cm) from the metamaterial aperture. The field is sampled at just below half the maximum frequency's wavelength (5mm) and an angular spectrum decomposition is used to propagate these fields to all points in the field-of-view. These radiated fields are sampled on planes uniformly spaced by ΔR in range. On each range plane the fields are uniformly sampled in azimuth and elevation at ΔAz and ΔEl, respectively, resulting in non-uniform sampling in Cartesian coordinates transverse to the optical axis. These then are the points at which the scene scatter-

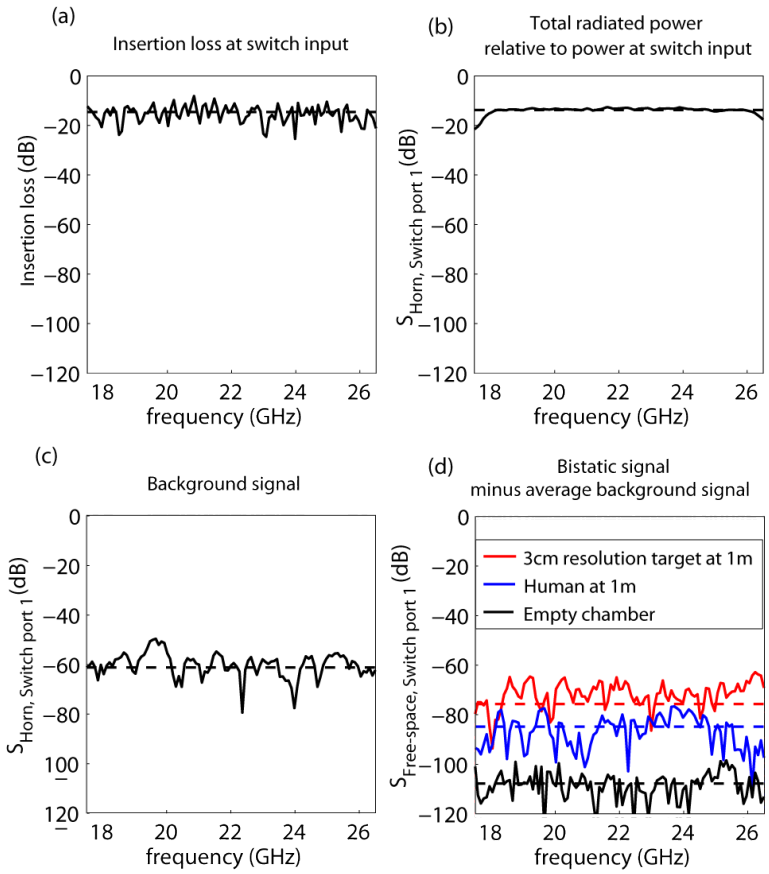

FIGURE 6.9: Various signal measurements for the 2D metamaterial aperture. Each figure shows a single trace for the central feed port of the metamaterial aperture (solid lines) as well as the mean signal power over all frequencies and feed ports (dashed line). The signal for the central port is similar in mean, variance, maximum, and minimum signal to that of other ports. (a) the insertion loss is below -7.5dB for all ports and averages -14.5dB. (b) the total radiated power of the metamaterial antenna, obtained from integrating the near-field measurements, averages -13.8dB. This power was measured relative to the input of the switch. There is a known loss of 1dB through the switch and 0.7dB through the 1ft length of cable from the switch to the feeds of the antenna. This means the total radiation efficiency is between -13.8dB and -12.1dB. (c) the average background signal, from the antenna ports to the receive horn, for an empty chamber is primarily due to direct coupling between the metamaterial antenna and the receive horn. It averages -61.2dB. (d) The measurements of all scenes have the average background signal subtracted before being used in image the reconstruction. The empty chamber signal minus the average background signal is approximately the noise floor of the system, -107.8dB. A typical metallic scene has an average signal power of -75.7dB, while the signal power from a person with no metallic objects averages -84.9dB.

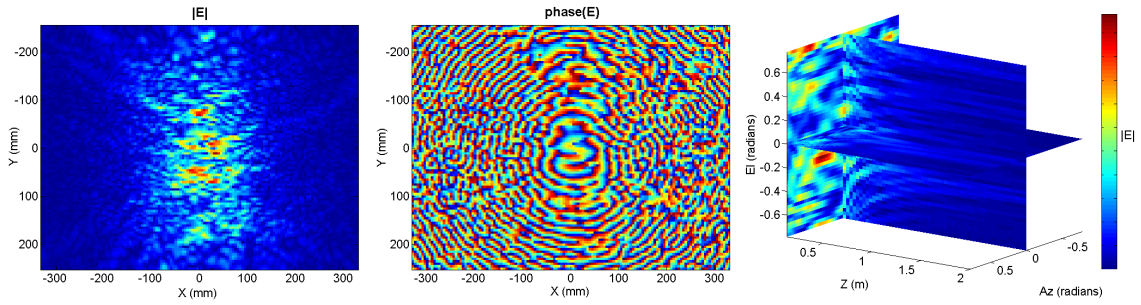

FIGURE 6.10: (Left and Middle) the electric field just in front of the 2D aperture, measured with a near-field scan, from feed port 1 at 21.9GHz. (Right) three cross-sections of the radiated field calculated from the same near-field scan.

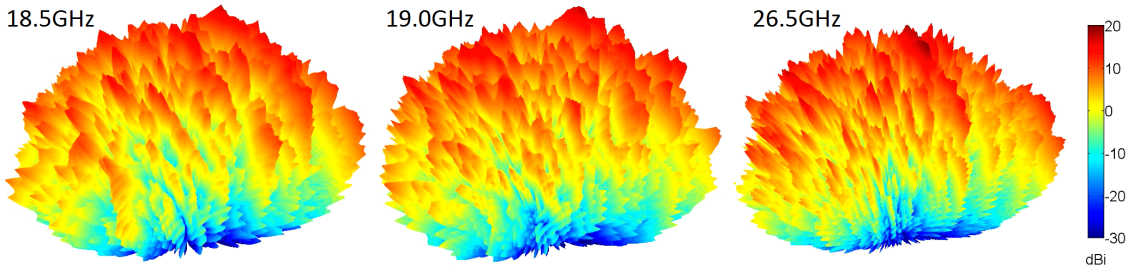

FIGURE 6.11: Experimentally measured far-field spherical plots in dBi of a 2D metaimager panel.

ing density is estimated. The metamaterial resonators are all co-polarized so that the radiated field is polarized in a single direction. The cross-polarized field is one order of magnitude smaller than the primary polarization. For this reason we only propagate the primary polarization and this is the only field component that enters into the imaging measurement matrix. The field across the near-field scan plane and the resulting radiation pattern are shown in Fig. 6.10.

These near-field scans confirmed the presence of an approximate cylindrical wave launched into the cavity by each feed, and confirmed that the cELC resonators couple to the magnetic field of this wave. The field radiated was calculated for a diffraction limited set of points in azimuth, elevation, and range for 101 frequencies and each of the 6 ports. The measurement matrix was calculated using these calculated radiation

patterns times the receiving low-gain probe.

6.2.3 Resolution

The operation bandwidth is K-band, specifically 17.5GHz-26.5GHz. This 9GHz bandwidth of the system gives a range resolution of,

$$\Delta R = \frac{c}{2BW} = 1.67cm \tag{6.1}$$

The frequency sampling rate of 90MHz determines the maximum range we can image, beyond which objects would alias in range. This is equivalent to the maximum unambiguous range in radar and is,

$$MUR = \frac{c}{2\Delta f} = 1.167m \tag{6.2}$$

The imaging system we used for the results presented here used two metamaterial apertures, side-by-side and co-planar, as the transmitters. A low gain (5dB) open-ended WR-42 waveguide located between the two metamaterial apertures was used as the receiver (Fig. 6.8). This aperture configuration gives an aperture that is 88.9cm wide and 55.9cm high. At our central frequency of $f_c = 22GHz$ we expect our horizontal (azimuthal) and vertical (elevation) angular resolution to be,

$$\Delta Az_c = \frac{\lambda_c}{A_x} = 0.88^o \quad \text{and} \quad \Delta El_c = \frac{\lambda_c}{A_y} = 1.4^o \tag{6.3}$$

where we have approximated the prefactor to be unity because our aperture is rectangular.

6.2.4 Scene measurement and estimation

The scene measurement process consisted of illuminating the scene with the metamaterial aperture and making a spectral measurement with the VNA of the signal scattered by the scene and received by the low-gain probe. Each aperture has six

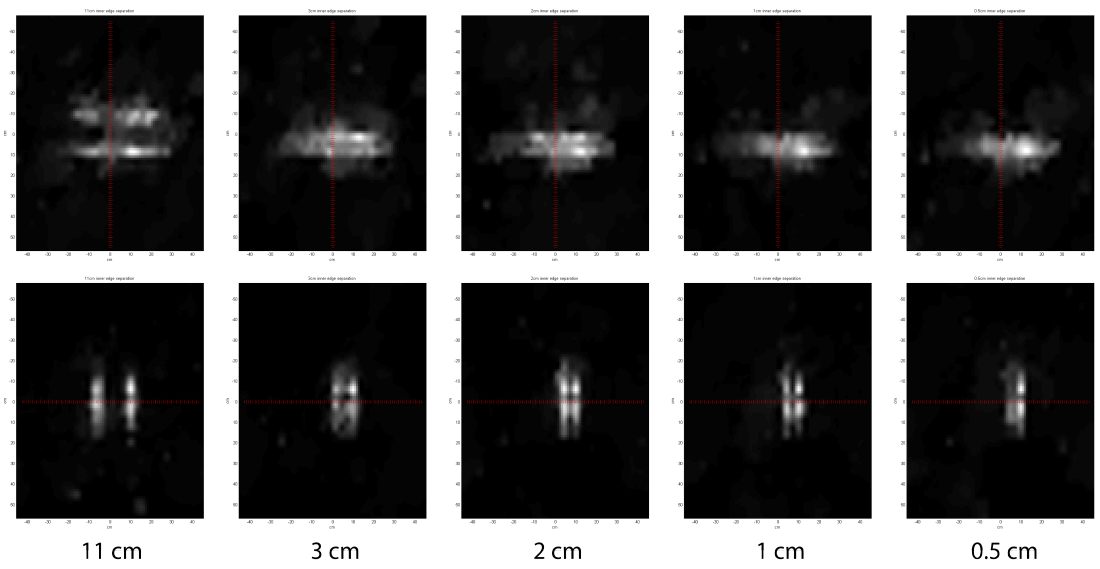

FIGURE 6.12: Reconstructed images of two parallel metal strips oriented horizontally and vertically with various separations. The fine red lines visible in the electronic copy are reference marks separated by 1cm. The inner edge to inner edge separation is given. The range to the strips is 1.15m; at this range the expected spatial resolution at the central frequency is $\Delta x = 1.76cm$ and $\Delta y = 2.8cm$. The horizontally oriented stripes are resolvable down to a separation of 2cm, while the vertically oriented stripes are resolvable down to 1cm separation.

feed ports and a spectrum was measured for each of the feed ports in sequence. For the two-panel system depicted in Fig. 6.8 there were 12 feed ports total, yielding 1212 measurements. From these measurements, a previously recorded background measurement was subtracted. This background signal contains both the signal from clutter outside the reconstruction volume as well as the direct signal from the source antenna to the receive antenna. The total background signal, $\mathbf{g}_{background}$, is shown in Fig. 6.9 c, and the clutter signal is shown in Fig. 6.9 d (empty chamber). This background subtraction is justified by the consideration that the background signals add linearly to the signal from the scene of interest and so can be linearly subtracted. This is valid as long as our linearity assumption holds, but this assumption must hold in order to reconstruct the scene itself, even in the absence of background signal. The

total signal measured is,

$$\mathbf{g}_{total} = \mathbf{H}_{scene}\mathbf{f}_{scene} + \mathbf{H}_{clutter}\mathbf{f}_{clutter} + \mathbf{g}_{direct} = \mathbf{H}_{scene}\mathbf{f}_{scene} + \mathbf{g}_{background} \tag{6.4}$$

With these measurements in hand, and the measurement matrix calculated from the near-field characterization an image of the scene scattering density was estimated using the TwIST[101] algorithm using a total-variation regularizer. The TV regularizer was applied to the real and imaginary components of the scene independently. TV was applied to the scene estimate across azimuth and elevation, but not range. In other words, only the gradients of the scene estimate in cross-range, not range, were minimized. We did not apply a penalty to the smoothness of the scene in range because we expect the scattering from targets to be primarily from their surfaces and particularly from the surfaces oriented perpendicular to the optical axis of the aperture. This plane-wise TV regularizer was implemented by Alex Mrozack in Dr. David Brady's group. All the instrument control, data processing, and image display was implemented in Matlab.

6.2.5 Scene constraint using structured-light sensors

The full field of view of the metaimager contains 2.63 million voxels. For our system configuration we measure 101 frequencies for each of our 12 sources. The resulting measurement matrix is 1212 by 2.63 million in size, and, represented as complex-valued single-precision numbers (2x4bytes/value), is then 25.5GB. This is a challenging amount of data to preform matrix computations with, but even more challenging is that the scene is undersampled to 0.046%. To reduce this we would like to constrain the reconstruction volume to only encompass regions where RF scattering objects may reside. Of course this amounts to a very strong prior that is generally unavailable to an imaging system. However we are able to obtain this prior information by making the assumption that any mm-wave scatterers will be visible

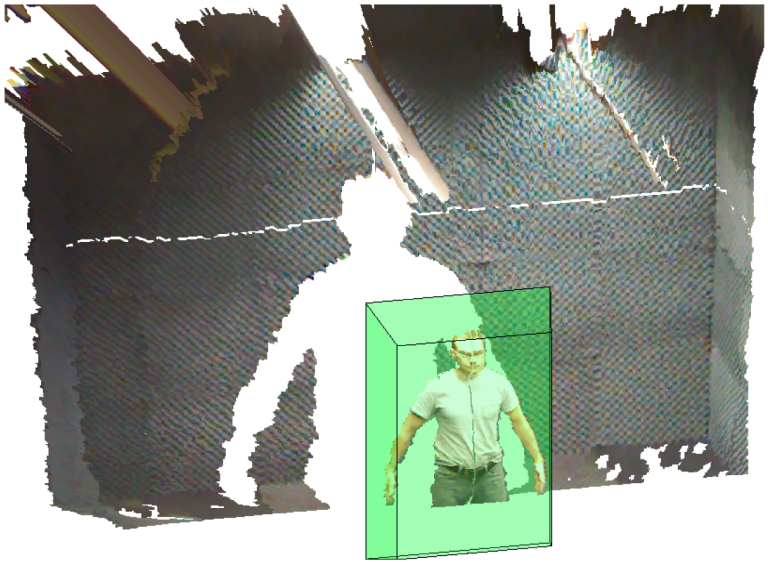

FIGURE 6.13: A three-dimensional surface and optical image of a person collected with a Kinect structured-light sensor. The green box around the person is the identified constraining volume in which the mm-wave signal is reconstructed. Note that the three-dimensional optical image has been rendered from a perspective different from the Kinects. Thus the region of the background occluded by the person is visible and appears as a white shadow.

to, or will be within objects that are visible to, optical and infra-red sensors. This allows us to use low-cost structured-light sensors and optical cameras to determine which regions in the scene are entirely empty. We then constrain our reconstruction to the complement of this space.

To this end we have integrated an infrared structured light sensor, the Microsoft Kinect, into the metaimager imaging system. Using the Kinect data, we calculate the three-dimensional coordinates of objects in front of the sensor, excluding the boundaries of our imaging chamber which is covered in mm-wave absorber. The Kinect sensor is capable of providing the user with very high-level information such as skeletal tracking, but at a lower level the Kinect determines an estimate of the range from the Kinect to each of the 640x480 pixels in its field of view. This can be translated to cartesian x-y-z coordinates of each of the 640x480 pixels points. We

perform contiguous-blob detection by first discarding all points with positions outside a box just within the known boundaries of our imaging chamber. This removes points the floor, walls, and ceiling. We then count the number of pixels closer than a distance z, $N(z)$ and find the z values where the first derivative of N(z) goes to zero. These are the front and back edges of objects within the imaging chamber. A similar search for zero-derivatives is then performed in the x- and y-directions, finding the horizontal and vertical extents of objects. This gives a trapazoidial volume with parallel front and back faces within which we may constrain the reconstruction. One we have determined the desired reconstruction volume, we can simply delete the columns of the measurement matrix that correspond to voxels located outside this region.

Of course a more sophisticated constraints would also be possible, such as a tight-fitting volume that conforms to the surface of the objects observed by the Kinect, or, for human targets, using the kinect's higher order skeletal tracking to estimate the body surface beneath clothing may be useful. Additionally, a soft - rather than a hard - boundary that penalizes voxels farther from the observed objects could be used. Alternatively, the Kinect data could be used as additional measurements to inform the non-linear scene estimation algorithm, but this would require developing an appropriate forward model corresponding to the Kinect measurements.

This yields an enormous reduction in the size of the image reconstruction problem. For instance, a person at 1.5 meters from the aperture is easily contained within a bounding box that is, 0.4m in range, 25^o in azimuth, and 60^o in elevation, giving 29.2 thousand voxels. The resulting measurement matrix is 283MB and the scene is undersampled to 4.15%, which is quite reasonable for compressive imaging reconstruction techniques. The images of people provided below used a slightly smaller volume of 0.3m in range, 20^o in azimuth, and 40^o in elevation, giving 11.7 thousand voxels for a measurement matrix size of 113MB and an undersampling to 10.4%.

The Kinect sensor also returns an optical image of the scene in front of it. This

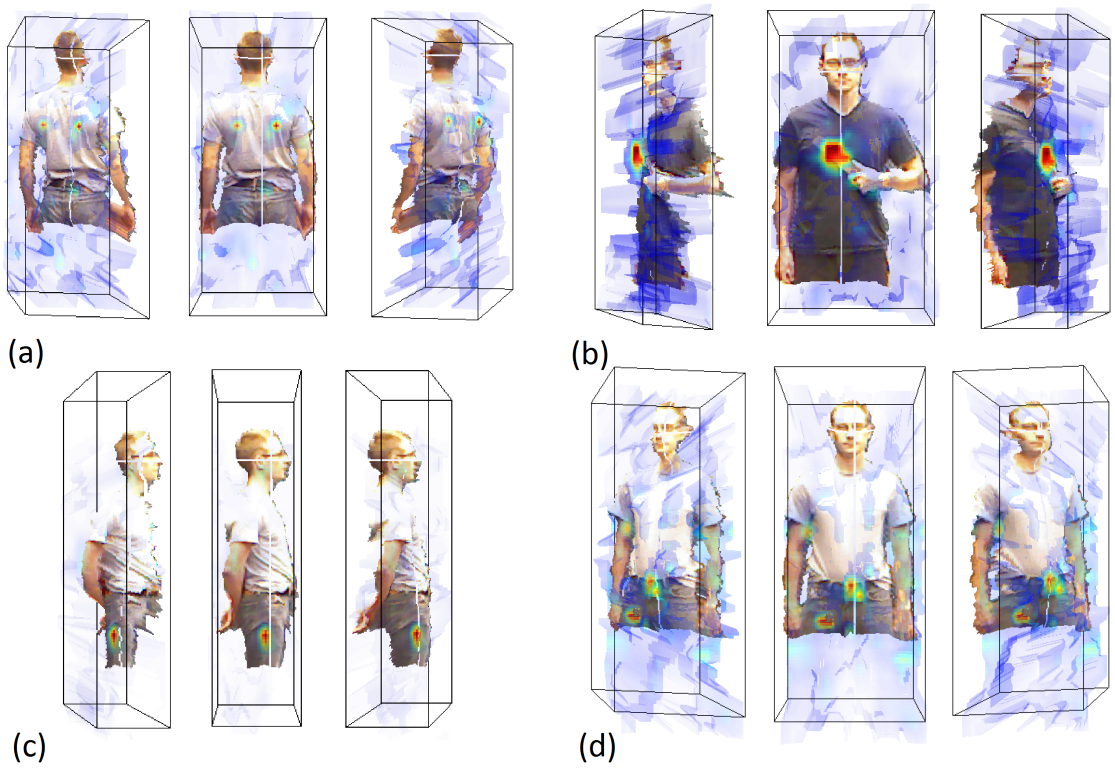

FIGURE 6.14: A person imaged with the metaimaging system, rendered from three perspectives. The false-color maximum-value surface of the reconstructed mm-Wave scattering density distribution is overlaid on the three-dimensional optical image. The mm-wave scattering density clearly picks metallic scatters on the person. The images show a person with different objects on them including (a) nothing, (b) a knife, (c) keys in their pocket, and (d) belt buckle and keys in their right pocket.

optical image can be registered to the 3D surface and overlaid on it, allowing for an approximation of a 3D optical image of the scene. The reconstructed mm-wave image is itself a 3D image and can then be overlaid on the 3D optical image from the Kinect, yielding a multispectral, 3D image. This image presentation format is very useful for image display and interpretation while largely circumventing privacy concerns. In addition, this registered multispectral 3D information may be extremely valuable for automated threat detection and other artificial intelligence image processing tasks.

6.2.6 Imaging performance

To display the reconstructed 3D scattering density, we use a maximum-value surface. Along each azimuth elevation ray the maximum value is selected. The range of this maximum value determines the range of the surface at that azimuth/elevation coordinate. The resulting surface is colored according to the maximum values.

Based on our aperture size and frequency of operation, we expect the horizontal resolution to be $\Delta Az = 0.88^o$ and the vertical resolution to be, $\Delta El = 1.4^o$. As shown in Fig. 6.12, we actually surpass this resolution in both the vertical and horizontal directions, with the actual minimum resolvable separation being approximately 0.5^o in the horizontal direction and 1^o in the vertical direction. This is because we estimated our angular resolution for the far-field, but we are in the radiative near-field of the aperture where focusing of the beam is possible allowing for slightly better resolution. Fig. 6.15 shows reconstructions of a 3cm resolution target which consisted of three vertical and three horizontal thin reflective stripes, oriented perpendicular to the optical axis. The stripes were 3cm wide, 15cm long, and separated by 3cm. In this figure we also see that vertical stripes, which measure horizontal resolution, are somewhat better resolved then the horizontal bars, which measure vertical resolution.

We varied the signal SNR of the measurements by changing the integration time which is inversely related to the IF bandwidth (IFBW) of the VNA. We measured the signal SNR at each IF bandwidth by making many measurements of the scene and calculating the signal variance and signal mean. Comparing the IFBW to the SNR allows us to determine the image quality versus SNR. A qualitative depiction of this relationship is shown in Fig. 6.15. We may estimate the reflectivity of this object as being one on the stripes and zero outside the stripes. This allows us to calculate the mean squared error of the reconstructed image, which is plotted versus

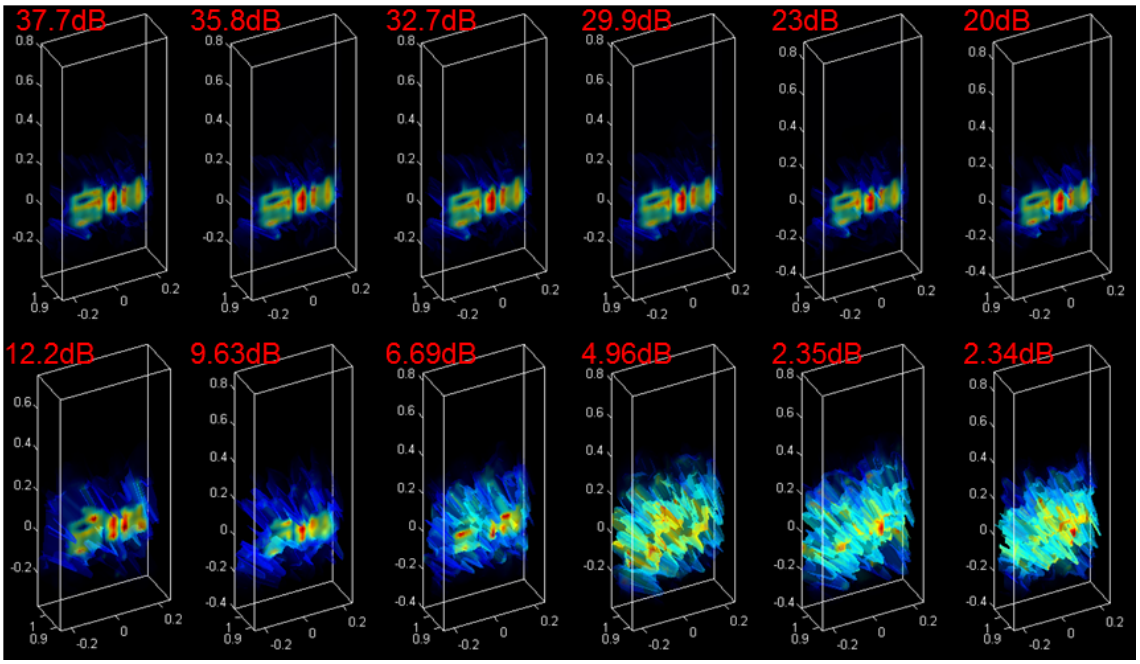

FIGURE 6.15: Maximum-value surface reconstruction of a 3cm resolution target imaged with different time integration. The SNR of the collected data for each image is labeled in red. The axis coordiantes are meters measured relative to the center of the imaging aperture.

signal SNR in Fig. 6.16. From Figs. 6.15 and 6.16 we see that the image quality improves with increasing SNR until approximately 20dB SNR at which point the image quality plateaus. This is explained by the poor singular value spectrum of our imaging system which shows a rapid fall-off in singular value versus singular vector for singular values at about -20dB. This means that the effective-rank of our measurement matrix increases very slowly as the noise level decreases (increasing the SNR) below -20dB.

The scene acquisition time at 100kHz IFBW was 2.7 seconds, limited mainly by the sweep overhead time. The total sweep time is given by,

$$t_{sweep} = N_{frequencies} * N_{sweeps} * (t_{settle} + 1/IFBW) + N_{sweeps} (t_{switch} + t_{overhead}) \quad (6.5)$$

where $N_{frequencies} = 101$ is the number of frequencies we sample, $N_{sweeps} = 12$ is the

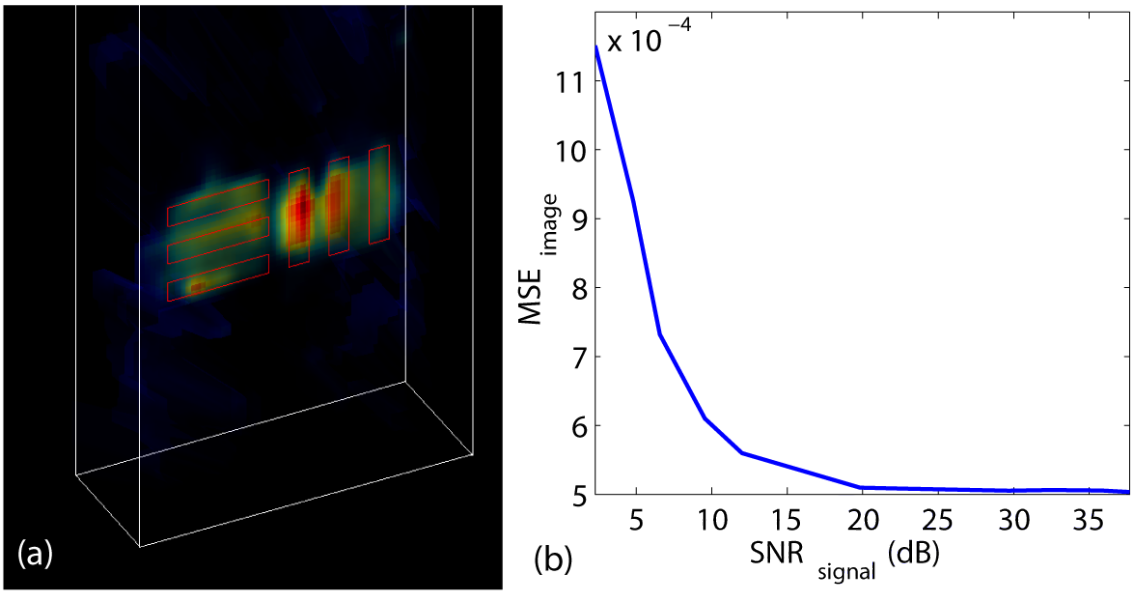

FIGURE 6.16: (a) A reconstruction of a 3cm resolution target with the true target location outlined in red. (b) the Mean Squared Error of reconstructed RF images versus the SNR of the measured signal. The SNR of the measured signal was varied by changing the integration time.

number of sources/recievers we switch between, $t_{settle} = 50\mu$s is the VNA settling time, $t_{switch} = 15$ms is the time to switch between sources, and $t_{overhead} \approx 200$ms is the sweep setup overhead time (instrument communication, sweep initialization, VNA sweep post-processing, data transfer etc.). The image reconstruction time averaged 5 seconds. The short image acquisition time makes imaging of slowly moving scenes possible. We looked at many scenes of people carrying various metallic objects. An example scene is shown in Fig. 6.14.

6.3 Conclusions

The metamaterial guided-wave frequency diverse imaging systems described here represent an entirely new method of radio-frequency imaging. The use of guided wave structures means these systems have minimal form-factor for a given aperture size. The use of complementary metamaterial radiators to make frequency-diverse mea-

surement modes means these systems have no moving parts, fast image acquisition times, and utilize only a single emitter/detector which reduces cost.

However, the metamaterial imaging systems presented here were largely proof-of-concept devices. Little work went into optimizing the overall radiation efficiency of these systems. Improving the efficiency of these systems would improve signal SNR, in turn improving image quality and reducing acquisition time.

The measurement modes radiated by the metaimagers presented here were simply pseudo-random. From the standpoint of compressed sensing this is a reasonable basis to use, but is by no means ideal. In order to further optimize these imaging systems, work should continue on explicit mode generation. This requires a very complete semi-analytical model of the metamaterial aperture. While a great deal of work has been done in developing such a model using discrete-dipole-approximations which predicts the radiated modes from a known metamaterial aperture, this model has yet to be applied to the reverse problem of determining what metamaterial aperture would generate a desired mode. In the case of a frequency-diverse aperture, this problem needs to be solved including dispersion such that at each measurement frequency a different desired measurement mode is radiated.

It also remains to determine the optimal regularizer for undersampled microwave scenes. The regularizers used here, l_1-sparsity and total-variation, are out-of-the-box regularizing solutions which are likely non-optimal for the types of scenes we consider below. For example, at RF frequencies we expect objects to scatter mainly form their surfaces and so to be similar to a 2D manifold in the 3D scene-space. This is partly why the planar-total-variation regularizer used here works well, but this prior could perhaps be more explicitly enforced. In addition, a better sparsifying-basis in which to apply l_1-sparsity regulariation could be developed, perhaps using dictionary-based methods.

7

Tuning Metamaterial Apertures

A major advantage of metamaterial radiators in this application is the ability to incorporate tuning[119]. The exceptional control of the radiation pattern of the antenna provided by the application of metamaterial radiators will allow radiation modes, which are directly related to the measurement matrix, to be tailored to different types of scenes. Dynamically varying the resonance of the metamaterial elements would enable reconfigurable measurement modes. In addition, the ability to electrically tune the metamaterial radiators will allow the measurement matrix to be dynamically adapted to changes in, or our knowledge of, the scene. Dynamic tuning also frees the frequency bandwidth — effectively enabling hyperspectral imaging[120]. Alternately, single-frequency 3D imaging could be done in the nearfield where the radiation mode could be focused to various points in space. This would also allow for 3D imaging with amplitude measurements alone.

Tuning spans a wide-range of possibilities, from detailed element control utilizing methods such as semiconductor integration to broad group and/or system level tuning based on lumped electro-optical feed elements. Each choice has tradeoffs in terms of price, complexity, functionality, and speed. For instance, while individual

element control may be critical for detailed hyperspectral imaging — allowing for identification of resonant or dispersive objects in a scene — a systems-level phase-distortion/shift incorporated to the feeding mechanism may allow enough reconfiguration to perform a few unique space-bandwidth-product datasets, thus gaining coarse hyper-spectral information.

Such hybrid approaches span a range of tuning possibilities. An incomplete list of general approaches to tuning is:

Waveguide mode tuning — by modification of the source or feed structures and/or leveraging the relative phase-shift between resonator elements. Possible methods include variable waveguide termination impedance, load waveguide with tunable dielectric, and mechanical deformation. We are currently using this approach by switching through our feeding locations on the 2D metamaterial apertures.

Intra-array tuning — using phase shifters between element-groups or waveguide groups, allowing mode shaping in a phased-array modality, though with far fewer phase-shifting elements.

Individual resonator and/or resonator-group tuning — by modifying the radiation of the metamaterial resonators themselves arbitrary holograms could be 'written' on the aperture. This approach is likely the most useful in terms of flexibility and control of the modes radiated by an antenna because it gives the finest control over the aperture fields. Below we consider two approaches to achieving this type of control using integrated semiconductor devices for individual element tuning.

We have focused on semiconductor tuning methods due to their high speed. Because our imaging system utilizes only a single detector measurements must be collected sequentially. This means that if we rely only on aperture reconfiguration to collect our measurements, the aperture would need to be reconfigured approximately $N = 50,000$ times per frame (based on the number of voxels needed to image a person-sized scene with no compression) or, for 10 frames-per-second, about once

every 2μs. Of course one of the principal goals of having a reconfigurable aperture is to be able to produce optimal measurement modes, which may even be dynamically chosen based on information obtained from previous measurements. This means that many fewer than N modes would need to be produced. At a reasonable measurement compression of 10% the aperture would need to be reconfigured about once every 20μs to achieve 10 frames-per-second imaging. Other methods not discussed here for individual element tuning include liquid crystal tuning[121], MEMS-based mechanical tuning[122], temperature[123] and photo-doped semiconductors[124].

7.1 Schottky junction tuning

One approach to element tuning is to shift the resonance frequency of a metamaterial resonator. If a resonator is excited by a single frequency, then it will radiate strongly only if the resonance frequency is near the excitation frequency. Thus if the resonance frequency of the element can be shifted far enough, then the radiation from that element can be switched on and off. One way of changing the resonance frequency of a resonator is to vary the capacitance in the resonator. This could be achieved by incorporating a Schottky diode or PN-junction into the resonator and reverse biasing it [125],[126].

A Schottky diode is the simpler of the two options because it only requires a single uniformly doped semiconductor and a single Schottky-type metal contact. To get the most tuning from this approach, the electric fields of the metamaterial resonator should be concentrated in the semiconductor region. For this reason, a multi-layer complementary metamaterial structure has been considered. This structure allows the semiconductor to be sandwiched in the capacitive region of the cELC, thus concentrating the fields in the Schottky junction. When reverse biased, the depletion region of the Schottky junction grows, varying the capacitance of the junction and shifting the resonance frequency of the resonator in which it is incorporated.

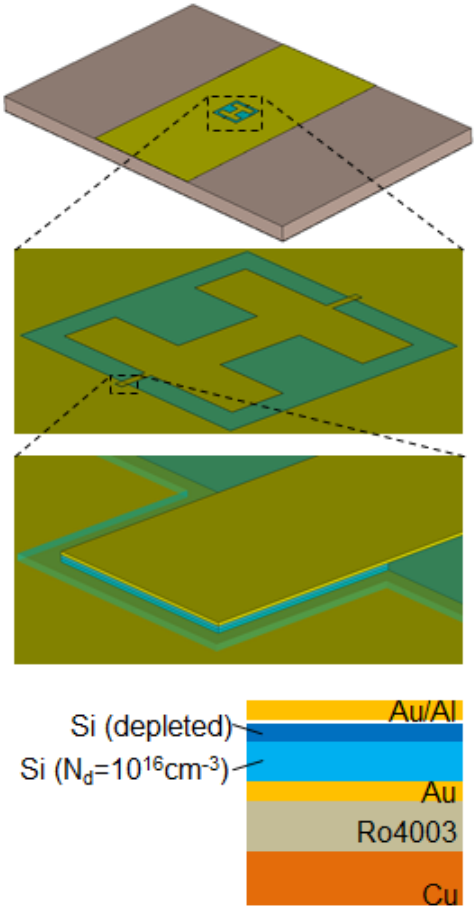

FIGURE 7.1: (Top) A series of insets of the designed and simulated Schottky-tuned cELC structure. The cELC is patterned in a microstrip. To reverse bias the Schottky junction a DC bias would be applied between the cELC and the microstrip signal trace. The biasing line is not drawn. (Bottom) the device cross-section through the Schottky junction. The Schottky junction is between the Si and the Al of the cELC.

We have designed and simulated such a complementary-ELC structure patterned in a microstrip waveguide, shown in Fig. 7.1. The silicon had a doping concentration of 1016cm-3 and the Schottky junction was formed at the interface of the silicon and an aluminum layer on the bottom of the cELC layer. The depletion thickness for this junction at zero bias was 300nm. Because the cELC layer is electrically isolated at DC from the signal trace of the microstrip, the junction could be reverse biased by a DC bias applied between the cELC and the microstrip signal trace. The maximum

achievable reverse bias before breakdown was -7VDC, corresponding to a depletion thickness of 1um.

If the resonance frequency of the cELC under zero bias is $f_{0,0}$ and the full-width-half-max of the resonance frequency at zero bias is Δf then the quality factor at zero bias is,

$$Q_0 = \frac{f_{0,0}}{\Delta f_0} \tag{7.1}$$

Then we can define the resonance frequency shift when reverse biased in units of Δf_0 so the resonance frequency when reverse biased is $f_{0,biased} = f_{0,0} - n\Delta f_0$. This is a useful measure of the shift in the resonance frequency because the degree to which the radiation from the resonator is reduced is related not just to how far the resonance frequency has moved but also to the width of the resonance. The fractional shift in the resonance frequency is then,

$$f_{0,biased}/f_{0,0} = \frac{f_{0,0} - n\Delta f_0}{f_{0,0}} = 1 - \frac{n}{Q_0} \tag{7.2}$$

Since the resonance frequency of a series RLC resonator is $2\pi f_0 = 1/\sqrt{LC}$, the fractional change in the capacitance of the Schottky junction, which is inversely proportional to the depletion depth of the junction, required to shift the resonance frequency by n times Δf_0 is then,

$$\frac{d_n}{d_0} = \frac{C_0}{C_n} = \left(\frac{f_{0,n}}{f_{0,0}}\right)^2 = \left(1 - \frac{n}{Q_0}\right)^2 \tag{7.3}$$

So as expected, for a lower Q (wider) resonance, the change in capacitance required to shift the resonance the same number of full-width-half-maxes increases.

The silicon layer is not extremely low resistivity and so the depletion layer plus the undepleted silicon can be thought of as a voltage variable capacitor in series with a voltage variable resistor. Since the quality factor of a series RLC resonator is

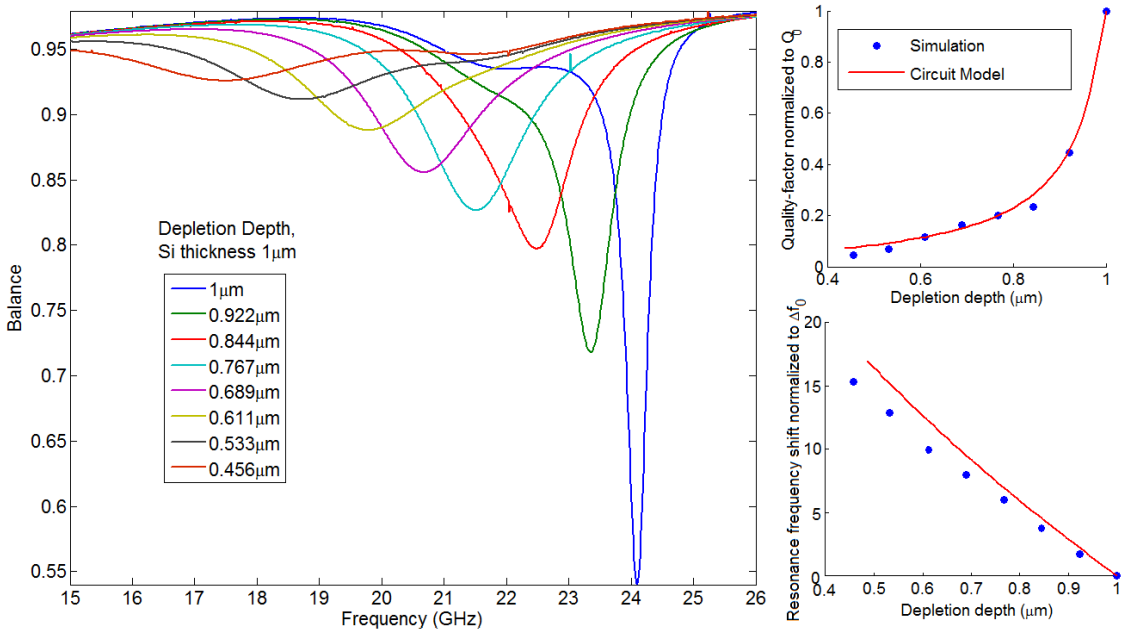

FIGURE 7.2: (Left) Full-wave simulation of the signal through a microstrip patterned with a single Schottky-tuned cELC. Each color curve corresponds to a different depletion region thickness (corresponding to reverse bias of the Schottky junction). (Right) comparison of the simulation results to the simple circuit model for the quality factor and resonance frequency shift.

$Q = 1/R\sqrt{L/C}$, the quality-factor of the resonance also depend on the reverse bias of the Schottky junction. The quality factor of the of the biased resonator normalized to the quality factor at zero bias is then simply the ratio of the series resistance at zero bias to the resistance when biased,

$$\frac{Q_{biased}}{Q_0} = \frac{R_{cELC} + R_{Schottky}(0)}{R_{cELC} + R_{Schottky}(V_b)} \tag{7.4}$$

The resistance in the cELC , R_{cELC} , can be calculated from the geometry of the cELC and the metal resistivity, while the resistance in the Schottky junction at V_b volts reverse bias, $R_{Schottky}(V_b)$ can be calculated from the Drude model (presented below) and the thickness of the Schottky junction depletion region at this reverse bias. These two simple circuit models are compared to simulation results in Fig. 7.2.

7.2 MOSFET tuning

An alternative approach to tuning the resonance of a metamaterial resonator is to change a resistance in the resonator rather than a capacitance. A change in resistance may be achieved with either a two-terminal or three-terminal device. The resistance of two-terminal devices, such as PIN diodes or the Schottky diode discussed above, is controlled by the forward voltage across the two terminals. Because the control voltage is applied across the two terminals for which the resistance is being changed, the control voltage must induce a current and so these are often called current-controlled devices. On the other hand, Field-Effect-Transisor (FETs), such as a Metal-Oxide-Semiconductor Field-Effect-Transistor (MOSFET), are three terminal, voltage-controlled devices. In a FET device applying a bias to the gate electrode changes the resistance between two separate electrodes, the source and drain. Such a device is appealing because the gate electrode in a FET device has very low leakage current. This means that if a small charge can be accumulated on the gate electrode and then the electrode can be electrically isolated, this charge will continue to bias the gate and the FET will stay in conducting state until the charge is removed from the gate. This makes FET devices useful for row-column addressing where single rows of FETs are switched at time, then ignored, while other rows are switched, reducing the needed number of control lines.

The high frequency conductivity of silicon is of paramount importance for this type of application. At some high frequency, the limited mobility of electrons and holes in silicon will result in a fall off in conductivity. The high frequency behavior of silicon can be well modeled with the Drude model, which may be used to calculate the complex permittivity and conductivity versus frequency of materials with free

charges. Drude model:

$$\epsilon_r(\omega) = \epsilon_b - \frac{\omega_p^2}{\omega(\omega + i\Gamma)} = \epsilon_b - \frac{\omega_p^2}{\omega^2 + \Gamma^2}\left(1 - i\frac{\Gamma}{\omega}\right) \tag{7.5}$$

$$\epsilon(\omega) = \epsilon' + i\frac{\sigma}{\omega} \tag{7.6}$$

$$\sigma(\omega) = \epsilon_0 \frac{\omega_p^2 \Gamma}{\omega^2 + \Gamma^2} \tag{7.7}$$

The plasma frequency, ω_p, collision frequency, Γ, and DC conductivity, σ_0, for a semiconductor are given by,

$$\omega_p = \left(\frac{e^2 N}{\epsilon_0 m^*}\right)^{1/2} \tag{7.8}$$

$$\Gamma = 1/\tau = \frac{e}{\mu m*} \tag{7.9}$$

$$\sigma_0 = \frac{N e^2 \tau}{m*} = Ne\mu \tag{7.10}$$

where $m*$ is the effective mass, e is the elementary charge, N is the carrier concentration, and μ is the mobility of the charge carriers being considered. The effective masses of electrons and holes at 300K are approximately [Hisham Z. Massoud, ECE216 lecture notes],

$$m_{e,Si} = 1.09 \cdot 9.109 \cdot 10^{-31} kg \tag{7.11}$$

$$m_{h,Si} = 1.15 \cdot 9.109 \cdot 10^{-31} kg \tag{7.12}$$

The carrier mobilities ($[\mu] = cm2/V \cdot s, [N] = cm - 3$) are, empirically,

Majority carriers:

$$\mu_{p,P} = 49.7 + \frac{418.3}{1 + \left(\frac{N_a}{1.6 \cdot 10^{17}}\right)^{0.70}} \tag{7.13}$$

$$\mu_{n,N} = 92 + \frac{1268}{1 + \left(\frac{N_d}{1.3 \cdot 10^{17}}\right)^{0.91}} \tag{7.14}$$

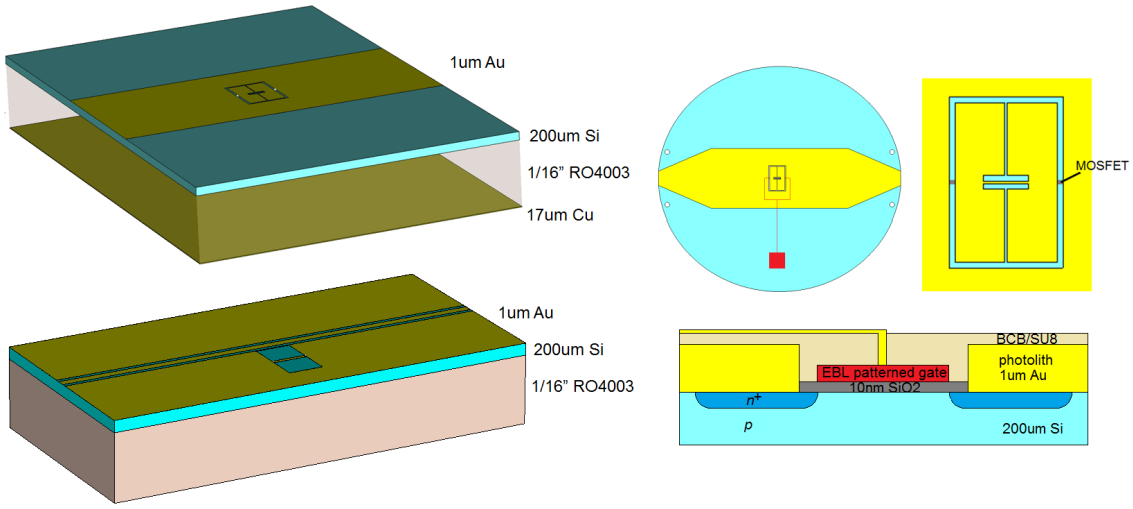

FIGURE 7.3: Design of a MOSFET-tuned cELC device. (Left) cELCs with integrated MOSFETs. In the top design, the cELC is embedded in a section of microstrip patterned on a high-resistivity silicon wafer. In the bottom design, the cELC is embedded in the ground trace of a section of coplanar waveguide (CPW) also patterned on a high-resistivity silicon wafer. The advantage of the CPW transmission line is its lower losses since the fields are less confined to the lossy silicon substrate. CPW is also simpler to test using standard RF wafer probing, in which signals are coupled to the device using actuated CPW probes rather than a mounted connector.

Minority carriers:

$$\mu_{n,P} = 232 + \frac{1180}{1 + \left(\frac{N_a}{8.0 \cdot 10^{16}}\right)^{0.90}} \tag{7.15}$$

$$\mu_{p,N} = 130 + \frac{370}{1 + \left(\frac{N_d}{8.0 \cdot 10^{17}}\right)^{1.25}} \tag{7.16}$$

We have designed and simulated several such a MOSFET-tuned devices, two of which are shown in Fig. 7.3. The devices consist of a complementary-ELC structure patterned on multi-conductor transmission line waveguides which are themselves patterned on a single 2inch diameter, 275um thick, high-resistivity ($> 5000\Omega \cdot cm, or < 10^12 carriers/cm^{-3}$) n-type silicon wafer. Two MOSFETs are incorporated into the cELCs such that the electrically isolated portion of the cELC is connected to the

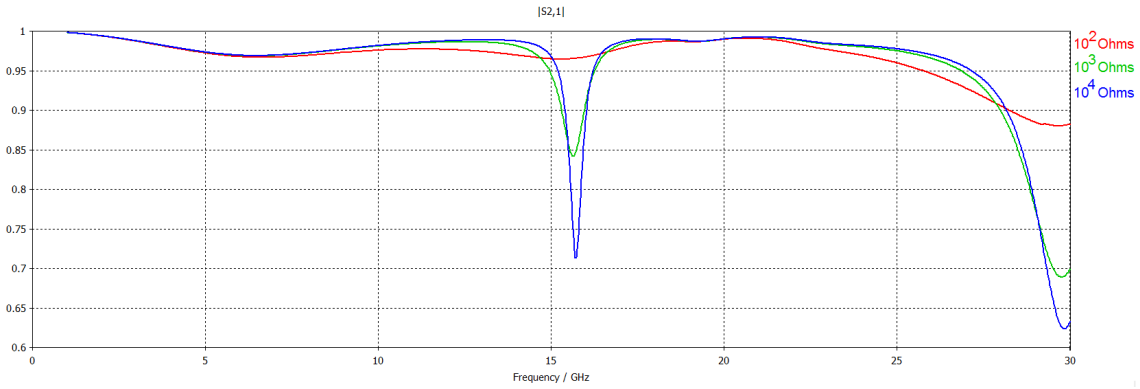

FIGURE 7.4: Full-wave simulation results for the signal transmitted through a microstrip patterned with a single MOSFET-tuned cELC. Each colored curve corresponds to a different source-drain resistance (corresponding to gate voltage).

Table 7.1: Drude model parameters for a MOSFET channel under different gate biases

	Bulk $\mu(cm^2/Vs)$	Interface $\mu(cm^2/Vs)$	Bulk $\Gamma(THz)$	Interface $\Gamma(THz)$	Bulk $\omega_p(THz)$
Holes ($V_g = 0$)	448.8	270	3.41	5.66	1.66
Electrons ($V_g = 8$)	1369	540	1.19	3.02	32.3

MOSFET source and the surrounding trace is connected to the MOSFET drain. The silicon wafer is compensation doped with p-type dopant to make a p-type channel MOSFET.

The doping concentration in the channel has a maximum concentration of $N_{p,max} = 2 \cdot 10^{15} cm^{-3}$ at the surface and then decreases with depth into the wafer as a complementary-error function. Because the inversion layer depth of the MOSFET is very thin only on the order of 100nm only the doping concentration and carrier mobility at the surface of the channel need to be considered. However, the effects of the gate field and surface defects near the surface cause the carrier mobilities to be reduced by a factor of 2-5. We can calculate the mobilities, collision frequencies, and plasma frequencies near the surface. These are given in Table 7.1. These parameters

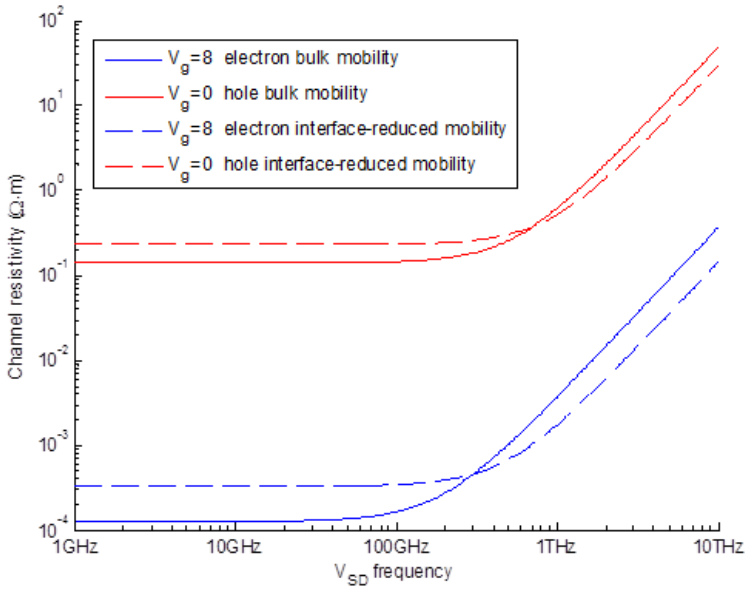

FIGURE 7.5: The resistivity of the MOSFET channel predicted by the drude model versus frequency.

can be used in the Drude model to calculate the best (no reduction in carrier mobility due to interface effects) and worse (reduced mobility due to interface effects) case channel resistivity, shown in Fig. 7.5. This shows that the expected fall off in channel conductivity occurs at approximately 100GHz and there is nearly a 3 order of magnitude change in the channel resistance, even for the reduced mobility case, for gate voltages of 0V to 8V. It is important to note that this operating frequency is the frequency of the signal conducted through the MOSFET, not the switching frequency which would be substantially lower. Fabrication of a test device with a single cELC resonator is ongoing.

7.3 Conclusions

The ability to tune metamaterials in many ways has been recognized as one of their most useful characteristics. In this chapter we have discussed some of the general concepts of metamaterial tuning and presented two semiconductor-based tuning ap-

proaches. By incorporating tuning into a guided-wave metamaterial imaging system, radically new imaging devices with minimal form-factor and optimal measurement mode formation could be developed.

8

Conclusion

In chapter 2 we presented work done by the author in the area of metamaterial lenses. We first introduced the concept of a metamaterial lens by demonstrating a simple gradient-index lens, then discussed more novel transformation-optical lenses. We showed that metamaterials enable many novel types of lenses. This flexibility of metamaterials makes them useful in creating many types of imaging systems with unprecedented form-factors and performance.

In particular, the complementary metamaterials presented in Chapter 4 have interesting applications to image system design. Not only do they provide a method of controlling the radiation traveling through a transmission line, acting as filters and effective material loadings, but they also can control how radiation leaks out of a transmission line. This makes them useful components for antennas with small form-factor and signal-multiplexing capabilities. By designing complementary metamaterial radiators that have different responses to different frequencies, polarizations, or other properties of radiation, then an antenna that can multiplex signals on these different channels can be formed.

This ability of metamaterial apertures to multiplex radiation patterns is demon-

strated by the metamaterial guided-wave frequency-diverse imaging systems — metaimagers — presented in Chapter 6. These unique metaimager systems make measurements that are indexed by frequency; each frequency sent into the metaimager aperture generates a different measurement mode. The use of guided wave structures means these systems have minimal form-factor for a given aperture size. The use of complementary metamaterial radiators to make frequency-diverse measurement modes means these systems have no moving parts, fast image acquisition times, and utilize only a single emitter/detector which further reduces size, weight, and cost.

Computational imaging provides the mathematical framework needed to invert these frequency-indexed measurements and recover an image of the scene. Compressed sensing allows these metaimagers to obtain the best images possible given the physical limitations of bandwidth and resonator quality-factor. The metamaterial imaging forward model presented in chapter 3 describes how a metaimager transforms between the scattering density of the scene that we want to estimate, and the frequency spectrum that we actually measure. This is the essential link that places the physics of a metaimager in the framework of computational imaging and allows it to be used for imaging. The forward models of these metaimagers were characterized using the far-field and near-field characterization systems presented in Chapter 5.

8.1 Areas for future research

The images produced by a computational imaging system are limited by the accuracy of the forward model. For this reason it is important in the future to address some of the non-linearities that exist in the metaimager forward model that have been ignored. In particular the specularity of the reflection from scene-patches. In addition, forward models that apply to other scenes that are likely to be encountered, such as resonate dielectric slabs, need to be developed.

The model presented here for the radiation of a metamaterial aperture gives accurate results when the coupling efficiency of the aperture and the reference mode are known. However, when the metamaterial radiators are very close together, they may couple in ways that make determining their collective response difficult and so determining the coupling efficiency of the aperture is also difficult. In addition, if the reference mode is a guided mode, as is the case for an aperture composed of complementary metamaterial radiators patterned on a transmission line, then the metamaterial elements will scatter the guided mode making it non-linear with respect to the aperture configuration. Work by others to address these problems using discrete-dipole-approximation methods is ongoing and the solution of this problem is essential to create engineered radiation patterns.

The measurement modes radiated by the metaimagers presented here were simply pseudo-random. From the standpoint of compressed sensing this is a reasonable basis to use, but is by no means ideal. In order to further optimize these imaging systems, work should continue on explicit mode generation. This requires a very complete semi-analytical model of the metamaterial aperture. While a great deal of work has been done in developing such a model using discrete-dipole-approximations which predicts the radiated modes from a known metamaterial aperture, this model has yet to be applied to the reverse problem of determining what metamaterial aperture would generate a desired mode. In the case of a frequency-diverse aperture, this problem needs to be solved including dispersion such that at each measurement frequency a different desired measurement mode is radiated.

The metamaterial imaging systems presented here were largely proof-of-concept devices. Little work went into optimizing the overall radiation efficiency of these systems. Improving the efficiency of these systems would improve signal SNR, in turn improving image quality and reducing acquisition time.

The ability to tune metamaterials has been recognized as one of their most useful

characteristics. In chapter 7, we have discussed some of the general concepts of metamaterial tuning and presented two semiconductor-based tuning approaches. By incorporating tuning into a metaimager system, radically new imaging devices with minimal form-factor and optimal measurement mode formation could be developed. Much work remains on incorporating tuning methods into complete imaging systems.

It also remains to determine the optimal regularizers for undersampled microwave scenes. The regularizers used here, l_1-sparsity and total-variation, are essentially out-of-the-box regularizing solutions which are likely non-optimal for the RF scenes we want to image. For example, at RF frequencies we expect objects to scatter mainly form their surfaces and so to be similar to a 2D manifold in the 3D scene-space. This is partly why the planar-total-variation regularizer used here works well, but this strong prior could perhaps be more explicitly enforced. In addition, a better sparsifying-basis in which to apply l_1-sparsity regularization could be developed, perhaps using dictionary-based methods.

Appendix A

A method of generating distributions of uniformly sized holes for GRIN metamaterials

Previous implementations of holey dielectric metamaterials rely on characteristics unique to each design to generate the inclusion distribution. The distribution may be generated by applying a transformation to a regular grid and placing an inclusion at each grid point,[12] however, this method requires you start with a known grid and can find a transformation that will yield the desired lattice constant at each location which is not possible in general. Alternatively, inclusions may be evenly spaced along lines of constant lattice constant,[20] however this relies on symmetries in the design to achieve crystallinity. For GRIN designs, it is possible to vary the size of inclusions at each grid point on a regular grid to achieve the desired index, [53] but for IR applications this significantly complicates processing and the range of realizable hole diameters may be limited, limiting the range of achievable indices. Here we propose a method to generate a hexagonal semi-crystalline distribution of uniformly sized inclusions with an arbitrarily varying lattice constant (Fig. 2.1).

In this method, the inclusions are treated as an analogous system of attractive

particles of finite size, where the size, or interaction length, of each particle is dependent on its position. The system of particles is allowed to dynamically relax from some initial configuration according to interaction rules defined such that the equilibrium arrangement will have the desired lattice constant distribution. This approach similar to variable size vortex-blob modeling of turbulent fluid flow in which the sizes of the vortices vary with position,[127, 128] and to non-uniform mesh generation techniques.

If the potential energy of two particles has a minimum at a separation of the desired lattice constant, then the particles will automatically arrange themselves with as close to hexagonal packing as possible. The potential energy of two particles with position dependent lattice constants $a_i(\vec{r}_i)$ and $a_j(\vec{r}_j)$, separated by $R_{ij} = |\vec{r}_i - \vec{r}_j|$ is given by,

$$U_{ij} = R_{ij}^{-\alpha} - C_{ij} R_{ij}^{-\beta} \quad , \quad \alpha > \beta \tag{A.1}$$

where,

$$C_{ij} = \frac{\alpha}{\beta} \left(\frac{a_i(\vec{r}_i) + a_j(\vec{r}_j)}{2} \right)^{(\beta-\alpha)} ,$$

such that the potential energy is minimized at a separation equal to the average of $a_i(\vec{r}_i)$ and $a_j(\vec{r}_j)$. If the potential well is large (more than $2a$) then the attraction from distant particles will cause the local lattice constant to be less than the ideal. This can be prevented by making the interaction range short by increasing β in Eq. A.1 and/or setting U_{ij} to a constant for $R_{ij} > \gamma(a_i + a_j)/2$ where $1 < \gamma < 2$. To reach a static equilibrium state, loss must be added to the particles' equation of motion. The equation of motion for particle p_i can then be given by,

$$\frac{d^2\vec{r}_i}{dt^2} = \frac{1}{m}\vec{F}_i - k\frac{d\vec{r}_i}{dt} \tag{A.2}$$

$$\vec{F_i} = (1 - \delta_{ij}) \sum_{j=1}^{N} -\partial U_{ij} \tag{A.3}$$

where m is the mass of a particle, k is a drag coefficient and N is the number of particles in the system. The requirement for equilibrium is that the gradient of a over a unit cell should never be greater than one, as no equilibrium state will exist.

The relaxation of the lattice can be quantified by calculating the average energy per particle from Eq. A.1 for each time step. This energy decreases until some non-zero local minimum is reached at which point the particles have reached an arrangement close to the ideal lattice constant distribution.

The system is initialized with a uniform hexagonal distribution of particles, as this reduces the time-to-equilibrium and the number of defects in the final lattice. Calculating the separation and resulting force between all particles every iteration requires a large amount of computation time, much of which is unnecessary because we require the force between distant particles to be negligible or zero. This computational overhead can be decreased by maintaining a list of each particle's nearest neighbors and only calculating the interaction between these particles. As the particles move or leave the domain, this list must be re-sorted. However, if the list of nearest neighbors is sufficiently large, then the list can be re-sorted infrequently, or every τ iterations. It can be shown that the for the infrequently sorted method, the factor decrease in computational time from the naive method approaches $1/\tau$ for even modest numbers of particles.

$$\alpha = \frac{N + \tau + 1}{N\tau} \tag{A.4}$$

So, for even modest numbers of particles, α approaches $1/\tau$. In addition, these re-sorts can be front-loaded since the degree of particle rearrangement decreases as the system reaches equilibrium. As $1/\tau \to 0$ the computation requirement approaches

$O(N)$.

To create an inclusion distribution with a desired index of refraction profile, we must first generate a lattice constant distribution that will produce the desired index profile. This is done by using an appropriate effective medium approximation to convert our index profile to a lattice constant profile. For instance, for a transverse electric (TE) wave where the electric field is parallel to the inclusion axes, the effective permittivity is determined by the volume average of the matrix permittivity and the inclusion permittivity. The volume fraction of inclusions, f_{TE}, needed to achieve an effective permittivity of ϵ_{eff} is then given by,

$$f_{TE} = \frac{\epsilon_{eff} - \epsilon_{matrix}}{\epsilon_{inc} - \epsilon_{matrix}} \tag{A.5}$$

For transverse magnetic (TM) waves where the electric field is transverse to the inclusion axes and the height of the inclusions is much greater than their diameter, the Maxwell-Garrnet equation is a better approximation of the effective permittivity. The volume fraction, f_{TM}, is then given by, [46]

$$f_{TM} = \frac{(\epsilon_{inc} + \epsilon_{matrix})(\epsilon_{eff} - \epsilon_{matrix})}{(\epsilon_{inc} - \epsilon_{matrix})(\epsilon_{eff} + \epsilon_{matrix})} \tag{A.6}$$

When the height of the inclusions is comparable to their diameter, then a modification of Eq. A.6 accounting for depolarization is required.[46]

The lattice constant, a, of a hexagonal lattice with volume fraction, f, of inclusions with diameter d, is,

$$\frac{a}{d} = \left(\frac{\pi}{2\sqrt{3}f}\right)^{\frac{1}{2}} \quad , \quad f \leqslant \frac{\pi}{2\sqrt{3}} \tag{A.7}$$

The restriction on the domain of f is due to inclusion percolation. Using Eq. A.5 or Eq. A.6 and Eq. A.7 gives an index profile which will have the desired effective

index.

The effective medium approximation puts a restriction on the maximum size of the inclusions that can be used. To remain in the homogenizable limit, the maximum lattice constant should be less than or equal to the minimum wavelength of operation divided by ten. For TE operation with hole type inclusions this gives the condition,

$$d \leqslant \frac{\lambda}{10}\left(\frac{\pi}{2\sqrt{3}}\frac{\epsilon_{hole}-\epsilon_{matrix}}{\epsilon_{max}-\epsilon_{matrix}}\right)^{-1/2} \tag{A.8}$$

where ϵ_{max} is the maximum permittivity required by the design. For column type inclusions the result is the same except that the maximum column size corresponds to the minimum required permittivity.

Bibliography

[1] G. N. Hounsfield. Computerized transverse axial scanning (tomography): Part i. description of the system. *British Journal of Radiology*, 46:1016–1022, 1973.

[2] P. Lauterbur. Magnetic resonance zeugmatography. *Pure and Applied Chemistry*, 40:149–157, 1974.

[3] S. Kaczmarz. Angenherte auflsung von systemen linearer gleichungen (approximate resolution of systems of linear equations). *Bulletin International de l'Acadmie Polonaise des Sciences et des Lettres*, 35:355–357, 1937.

[4] R. Gordon, R. Bender, and G. T. Herman. Algebraic reconstruction techniques (art) for three-dimensional electron microscopy and x-ray photography. *Journal of Theoretical Biology*, 29:471–481, 1970.

[5] G. Breit and M. A. Tuve. A radio method of estimating the height of the conducting layer. *Nature*, 116:357, 1925.

[6] R. M. Page. The early history of radar. *Proceedings of the IRE*, 50:1232–1236, 1962.

[7] S. Lasswell. History of sar at lockheed martin (previously goodyear aerospace). *Proc. SPIE, Radar Sensor Technology IX*, 5788:1–12, 2005.

[8] D. L. McMakin D. M. Sheen and T. E. Hall. Three-dimensional millimeter-wave imaging for concealed weapon detection. *IEEE Transactions on microwave theory and techniques*, 49:1518–1592, 2001.

[9] J. B. Pendry, D. Schurig, and D. R. Smith. Controlling electromagnetic fields. *Science*, 312:1780, 2006.

[10] D. Schurig, J. J. Mock, B. J. Justice, S. A. Cummer, J. B. Pendry, A. F. Starr, and D. R. Smith. Metamaterial electromagnetic cloak at microwave frequencies. *Physical Review Letters*, 314:977, 2006.

[11] J. Li and J. B. Pendry. Hiding under the carpet: a new strategy for cloaking. *Physical Review Letters*, 101:203901, 2008.

[12] J. Valentine, J. Li, T. Zentgraf, G. Bartal, and X. Zhang. An optical cloak made of dielectrics. *Nature Materials*, 8:568, 2009.

[13] L. H. Gabriell, J. Cardenas, C. B. Poitras, and M. Lipson. Silicon nanostructure cloak operating at optical frequencies. *Nature Photonics*, 117:461, 2009.

[14] Y. Urzhumov, F. Ghezzo, J. Hunt, and D. R. Smith. Acoustic cloaking transformations from attainable material properties. *New Journal of Physics*, 12:1–22, 2010.

[15] Y. Urzhumov, N. Landy, T. Driscoll, D. Basov, and D. R. Smith. Thin low-loss dielectric coatings for free-space cloaking. *Optics Letters*, 38:1606–1608, 2013.

[16] B. J. Justice, V. N. Nguyen, S. H. Ynak, J. Kim, and D. R. Smith. Electric-field-coupled metamaterials for microwave beam formation. *IEEE Antennas and Propagation Society International Symposium*, pages 2566–2569, 2007.

[17] V. N. Nguyen and D. R. Smith S. H. Ynak. Millimeter-wave artificial dielectric gradient index lenses. *3rd European Conference on Antennas and Propagation*, pages 1886–1890, 2009.

[18] D. Schurig. An aberration-free lens with zero f-number. *New J. Phys.*, 10:115034, 2008.

[19] N. Kundtz and D. R. Smith. Extreme-angle broadband metamaterial lens. *Nature Materials*, 92:129, 2009.

[20] L. Xue and V. F. Fusco. 24 ghz automotive radar planar luneburg lens. *IET Microw. Antennas Propag.*, 1:624, 2007.

[21] J. Hunt, T. Tyler, S. Dhar, Y. Tsai, P. Bowen, S. Larouche, N. M. Jokerst, and D. R. Smith. Planar, flattened Luneburg lens at infrared wavelengths. *Optics express*, 20(2):1706–13, 2012.

[22] T. Driscoll, G. Lipworth, J. Hunt, N. Landy, N. Kundtz, D. N. Basov, and D. R. Smith. Performance of a three dimensional transformation-optical-flattened lneburg lens. *Optics Express*, 20:13262–13273, 2012.

[23] N. Fang, H. Lee, C. Sun, and X. Zhang. Subdiffraction-limited optical imaging with a silver superlens. *Science*, 308:534–537, 2005.

[24] Z. Liu, H. Lee, Y. Xiong, C. Sun, and X. Zhang. Far-field optical hyperlens magnifying sub-diffraction-limited objects. *Science*, 315:1686, 2007.

[25] J. B. Pendry, D. Schurig, and D. R. Smith. Controlling electromagnetic fields. *Science*, 312(5781):1780–2, 2006.

[26] T. Driscoll, D. N. Basov, A. F. Starr, P. M. Rye, S. Nemat-Nasser, D. Schurig, and D. R. Smith. Free-space microwave focusing by a negative-index gradient lens. *Applied Physics Letters*, 081101, 2006.

[27] N. Kundtz and D. R. Smith. Extreme-angle broadband metamaterial lens. *Nature Materials*, 92:129, 2009.

[28] Y. Urzhumov and D. R. Smith. Metamaterial-enhanced coupling between magnetic dipoles for efficient wireless power transfer. *Physical Review B*, 83:31–33, 2011.

[29] E. Narimanov. Metamaterials to beat the static. *Nature Materials*, 7, 2008.

[30] Z. Jacob, L. V Alekseyev, and E. Narimanov. Optical hyperlens: Far-field imaging beyond the diffraction limit. *Optics express*, 7:8247–56, 2006.

[31] D. Takhar, J. N. Laska, M. B. Wakin, M. F. Duarte, D. Baron, S. Sarvotham, K. F. Kelly, and R. G. Baraniuk. A new compressive imaging camera architecture using optical-domain compression. *Proceedings of IST and SPIE Computational Imaging*, 4:1, 2006.

[32] M. F. Duarte, M. A. Davenport, D. Takhar, J. N. Laska, T. Sun, K. F. Kelly, and R. G. Baraniuk. Single-pixel imaging via compressive sampling. *Signal Processing Magazine, IEEE*, 25:83–91, 2008.

[33] B. M. Kaylor, A. Ashok, E. M. Seger, C. J. Keith, and R. R. Reibel. Dynamically programmable , dual-band computational imaging system. *Computational Optical Sensing and Imaging*, pages 3–5, 2012.

[34] X. Zhao, Z. Fang, J. Cui, X. Zhang, and G Mu. Illumination system using led sources for pocket-size projectors. *Applied optics*, 46:522–526, 2007.

[35] M. Florescu, S. Torquato, and P. J. Steinhardt. Designer disordered materials with large, complete photonic band gaps. *Proceedings of the National Academy of Sciences of the United States of America*, 106:20658–20663, 2009.

[36] H. Arguello, H. Rueda, Y. Wu, D. Prather, and G. Arce. Higher-order computational model for coded aperture spectral imaging. *Applied optics*, 2013.

[37] I. Noor and E. Jacobs. Adaptive compressive sensing algorithm for video acquisition using a single pixel camera. In *SPIE Proceedings*, 2012.

[38] P. K. Baheti and M. A. Neifeld. Feature-specic structured imaging. *Applied optics*, 45:73827391, 2006.

[39] P. K. Baheti and M. A. Neifeld. Aandom projections based feature-specific structured imaging. *Optics express*, 16:1764–1776, 2008.

[40] W. L. Chan, K. Charan, D. Takhar, K. F. Kelly, R. G. Baraniuk, and D. M. Mittleman. A single-pixel terahertz imaging system based on compressed sensing. *Applied Physics Letters*, 93:121105, 2008.

[41] M. B. Wakin, J. N. Laska, M. F. Duarte, D. Baron, S. Sarvotham, D. Takhar, K. F. Kelly, and R. G. Baraniuk. An architecture for compressive imaging. *Computational Imaging*, IV:606509, 2006.

[42] W. L. Chan, H. Chen, A. J. Taylor, I. Brener, M. J. Cich, and D. M. Mittleman. A spatial light modulator for terahertz beams. *Applied Physics Letters*, 94:213551, 2009.

[43] D. J. Brady, K. Choi, D. L. Marks, R. Horisaki, and S. Lim. Compressive holography. *Optics Express*, 17(15):13040–13049, 2009.

[44] C. F. Cull, D. A. Wikner, J. N. Mait, M. Mattheiss, and D. J. Brady. Millimeter-wave compressive holography. *Applied optics*, 49(19):E67–82, 2010.

[45] J. Hunt, N. Kundtz, N. Landy, and D. R. Smith. Relaxation approach for the generation of inhomogeneous distributions of uniformly sized particles. *Applied Physics Letters*, 97:1–3, 2010.

[46] S. Luryi and A. V. Subashiev. Waveguides with uniaxially patterned layers. *Proc. of SPIE*, 6127, 2006.

[47] N. Grigoropoulos and P. R. Young. Low cost non radiative perforated dielectric waveguides. *33rd European Microwave Conference*, page 439, 2003.

[48] T. Baba, D. Mori, K. Inoshita, and Y. Kuroki. Light localizations in photonic crystal line defect waveguides. *IEEE Journal of selected topics in quantum electronics*, 10:484, 2004.

[49] J. Li, L. Xue, Z. Wang, and Y. Han. Colloidal photonic crystals with a graded lattice-constant distribution. *Optics Express*, 285:1037, 2007.

[50] H. Kurt and D. S. Citrin. Graded index photonic crystals. *Optics Express*, 15:1240, 2007.

[51] A. Talneau, M. Agio, C. M. Soukoulis, M. Mulot, S. Anand, and P. Lalanne. High-bandwidth transmission of an efficient photonic-crystal mode converter. *Optics Letters*, 29:1745, 2004.

[52] Y. Wakayama, A. Tandaechanurat, S. Iwamoto, and Y. Arakawa. Design of high-q photonic crystal microcavities with a graded square lattice for application to quantum cascade lasers. *Optics Express*, 16:21321, 2008.

[53] Z. L. Mei, J. Bai, and T.J. Cui. Gradient index metamaterials realized by drilling hole arrays. *J. Phys. D: Appl. Phys*, 43:055404, 2010.

[54] J. Hunt, G. Jang, and D. R. Smith. Perfect relay lens at microwave frequencies based on flattening a Maxwell lens. *Journal of the Optical Society of America B*, 28(8):2025, 2011.

[55] E. W. Marchland. *Gradient Index Optics*. Academic Press, New York, NY, 1978.

[56] J. E. Eaton. An extension of the luneburg-type lenses. *Naval Res. Lab.*, 4110:1, 1953.

[57] Y. G. Ma, C. K. Ong, T. Tyc, and U. Leonhardt. An omnidirectional retroreflector based on the transmutation of dielectric singularities. *Nature Materials*, 8:639–642, 2009.

[58] C. R. Simovski. Bloch material parameters of magneto-dielectric metamaterials and the concept of bloch lattices. *Metamaterials*, 1:62, 2007.

[59] D. R. Smith. Analytic expressions for the constitutive parameters of magnetoelectric metamaterials. *Physical Review*, 81:1, 2009.

[60] J. B. Pendry, A. J. Holden, D. J. Robbins, and W. J. Stewart. Magnetism from Conductors and Enhanced Nonlinear Phenomena. *IEEE Transactions on Microwave Theory and Techniques*, 47:2075, 1999.

[61] D. Schurig, J. J. Mock, and D. R. Smith. Electric-field-coupled resonators for negative permittivity metamaterials. *APL*, 88:1, 2006.

[62] U. Leonhardt. Optical conformal mapping. *Science*, 312:1777–1780, 2006.

[63] J. Li and J. B. Pendry. Hiding under the carpet: a new strategy for cloaking. *Physical Review Letters*, 101:203901, 2008.

[64] N. Landy, Y. Urzhumov, and D. R. Smith. *Quasi-Conformal Approaches for Two and Three-Dimensional Transformation Optical Media. Transformation Electromagnetics and Metamaterials*. Springer, London, 2014.

[65] N. I. Landy and W. J. Padilla. Guiding light with conformal transformations. *Optics Express*, 17:14872, 2009.

[66] D. R. Smith, Y. Urzhumov, N. B. Kundtz, and N. I. Landy. Enhancing imaging systems using transformation optics. *Optics Express*, 18:21238–21251, 2010.

[67] J. Hunt, N. Kundtz, N. Landy, V. Nguyen, T. Perram, A. Starr, and D. R. Smith. Broadband wide angle lens implemented with dielectric metamaterials. *Sensors*, 11:7982–7991, 2011.

[68] R. Luneburg. *Mathematical Theory of Optics*. Brown Univ., Providence, RI, 1944.

[69] H. Ko, M. Stoykovich, J. Song, V. Malyarchuk, W. Choi, C.-J. Yu, J. Geddes, J. Xiao, S. Wang, Y. Huang, and J. Rogers. A hemispherical electronic eye camera based on compressible silicon optoelectronics. *Nature*, 454:748–753, 2008.

[70] S. P. Morgan. General solution of the luneberg lens problem. *Journal of Applied Physics*, 29:1358, 1959.

[71] B. J. Justice, J. J. Mock, L. Guo, A. Degiron, D. Schurig, and D. R. Smith. Spatial mapping of the internal and external electromagnetic fields of negative index metamaterials. *Optics Express*, 14:8694–8705, 2006.

[72] A. D. Falco, S. C. Kehr, and U. Leonhardt. Luneburg lens in silicon photonics. *Optics Express*, 19:5156–5162, 2011.

[73] D. R. Smith, D. C. Vier, T. Koschny, and C. M. Soukoulis. Electromagnetic parameter retrieval from inhomogeneous metamaterials. *Physical Review E*, 71:1, 2005.

[74] J. Hunt, N. Kundtz, B. Sun, and D. R. Smith. Transformation optics compressed rotman lens implemented with complementary metamaterials. *Proc. SPIE 8021, Radar Sensor Technology XV*, 8021:1–7, 2011.

[75] W. Rotman and R F Turner. Wide-angle microwave lens for line source applications. *IEEE Transactions on anttenas and propagation*, page 623, 1963.

[76] L. Halla, H. Hansenb, and D. Abbotta. Rotman lens for mm-wavelengths. *Proc. of SPIE*, 4935:215, 2002.

[77] P. K. Singhal, P. C. Sharma, and R. D. Gupta. Rotman lens with equal height of array and feed contours. *Proc. of SPIE*, 51(8):2048–2056, 2003.

[78] A. Zaghloul, O. Kilic, S. Weiss, and E. D. Adler. Realization of rotman's concepts of beamformer lenses and artificial dielectric materials. *IEEE International Conference on Microwaves, Communications, Antennas and Electronics Systems*, page 1, 2009.

[79] L. Musa and M. S. Smith. Microstrip port design and sidewall absorption for printed Rotman lenses. *IEEE Proceedings*, 136:53, 1989.

[80] D. Roberts, N. Kundtz, and D. R. Smith. Optical lens compression via transformation optics. *Optics Express*, 17:16535, 2009.

[81] L. Schulwitz and A. Mortazawi. A new low loss rotman lens design using a graded dielectric substrate. *IEEE Transactions on Microwave Theory and Techniques*, 56(12):2734–2741, 2008.

[82] E. Sbarra, L. Marcaccioli, R. Gatti, and R. Sorrentino. A Novel Rotman Lens in SIW Technology. *European Microwave Conference*, page 1515, 2007.

[83] D. Schurig, J. B. Pendry, and D. R. Smith. Transformation-designed optical elements. *Optics Express*, 15:14772, 2007.

[84] F. Falcone, T. Lopetegi, M. Laso, J. Baena, J. Bonache, M. Beruete, R. Marques, F. Martyn, and M. Sorolla. Babinet principle applied to the design of metasurfaces and metamaterials. *Physical Review Letters*, 93:1, 2004.

[85] Q. Cheng, H. Feng, and T. J. Cui. Broadband planar Luneburg lens based on complementary metamaterials. *Physical Review Letters*, 95:1, 2009.

[86] D. R. Smith, W. Padilla, D. Vier, S. Nemat-Nasser, and S. Schultz. Composite medium with simultaneously negative permeability and permittivity. *Physical review letters*, 84(18):4184–7, 2000.

[87] V. G. Veselago. The electrodynamics of substances with simultaneously negative values of epsilon and mu. *Soviet Physics USPEKHI*, 10:509–514, 1968.

[88] A. Grbic and G. V. Eleftheriades. Overcoming the diffraction limit with a planar left-handed transmission-line lens. *Physical Review Letters*, 92:1–4, 2004.

[89] T. Xu, A. Agrawal, M. Abashin, K. J. Chau, and H. J. Lezec. All-angle negative refraction and active flat lensing of ultraviolet light. *Nature*, 497:470–474, 2013.

[90] David J. Brady. *Optical Imaging and Spectroscopy*. John Wiley & Sons, Inc., Hoboken, NJ, USA, March 2009.

[91] A. W. Lohmann. The space-bandwidth product, applied to spatial filtering and holography. *Research Paper RJ-438 (IBM San Jose Research Laboratory, San Jose, Calif.)*, pages 1–23, 1967.

[92] E. J. Candes. Compressive sampling. *Proceedings on the International Congress of Mathematics*, 98:1433–1452, 2006.

[93] D L Donoho. Compressed sensing. *Information Theory, IEEE Transactions on*, 52(4):1289–1306, 2006.

[94] R. M. Willett, R. F. Marcia, and J. M. Nichols. Compressed sensing for practical optical imaging systems: a tutorial. *Optical Engineering*, 50(7):072601, 2011.

[95] E. J. Candes. The restricted isometry property and its implications for compressed sensing. *Comptes Rendus Mathematique*, 346:589–592, 2008.

[96] L. Potter, E. Ertin, J. Parker, and M. Cetin. Sparsity and compressed sensing in radar imaging. *Proceedings of the IEEE*, 98:589–592, 2010.

[97] L. I. Rudin, S. Osher, and E. Fatemi. Nonlinear total variation based noise removal algorithms. *Physica D: Nonlinear Phenomena*, 60:259–268, 1992.

[98] S. Boyd and L. Vandenberghe. *Convex Optimization*. Cambridge University Press, Cambridge, 2004.

[99] C. De Mol I. Daubechies, M. Defrise. An iterative thresholding algorithm for linear inverse problems with a sparsity constraint. *Communicaitons on Pure and Applied Mathematics*, 57:1413–1457, 2004.

[100] I. W. Selesnick. Sparse signal restoration majorization-minimization. *Polytechnic Uni.*, pages 1–16, 2010.

[101] J. M. Bioucas-Dias and M. Figueiredo. A new twist: Two-step iterative shrinkage/thresholding algorithms for image restoration. *IEEE Transactions on Image Processing*, 16(12):2992–3004, 2007.

[102] K. Pearson. On lines and planes of closest fit to systems of points in space. *Philosophical Magazine*, 2:559–572, 1901.

[103] I. Jolliffe. *Principal Component Analysis*. John Wiley & Sons, Inc., 2005.

[104] M. Neifeld and P. Shankar. Feature-specific imaging. *Applied optics*, 42(17):3379–89, 2003.

[105] R. A. Fisher. The use of multiple measurements in taxonomic problems. *Annals of Eugenics*, 7:179–188, 1936.

[106] H. Yu and J. Yang. A direct lda algorithm for high-dimensional data with application to face recognition. *Pattern Recognition*, 34:2067–2070, 2001.

[107] J. Goodman. *Introduction to Fourier Optics*. Roberts & Company Publishers, 3 edition, 2005.

[108] Eugene Hecht. *Optics*. Pearson Education, 4 edition, 2001.

[109] S. Larouche, Y. Tsai, T. Tyler, N. M Jokerst, and D. R Smith. Infrared metamaterial phase holograms. *Nature materials*, 11(5):450–4, 2012.

[110] R. Liu, X. Yang, J. G. Gollub, J. Mock, T. J. Cui, and D. R. Smith. Gradient index circuit by waveguided metamaterials. *Applied Physics Letters*, 94(7):073506, 2009.

[111] N. Landy, J. Hunt, and D. R. Smith. Homogenization analysis of complementary waveguide metamaterials. *Photonics and Nanostructures - Fundamentals and Applications*, pages 1–15, 2013.

[112] S. Eggermont, R. Platteborze, and I. Huynen. Investigation of metamaterial leaky wave antenna based on complementary split ring resonators. *European Microwave Conference*, 11:209–212, 2009.

[113] J. L. Volakis, A. A. Oliner, and D. R. Jackson. *Antenna Engineering Handbook Fourth Edition*. McGraw-Hill, 2007.

[114] A. A. Oliner. Scannable millimeter wave arrays. *RADC-TR-89-8, Vol II, Final Technical Report*, page 285, 1989.

[115] Oliner A. A. A new class of scannable millimeter-wave antennas. *Microwave Conference, 20th European*, 346:95–104, 1990.

[116] S. Gregson, J. McCormick, and C. Parini. *Principals of Planar Near-Field Antenna Measurements*. The Institution of Engineering and Technology, London, 2007.

[117] J. Hunt, Tom Driscoll, Alex Mrozack, Guy Lipworth, Matthew Reynolds, David Brady, and David R Smith. Metamaterial apertures for computational imaging. *Science*, 339(6117):310–3, 2013.

[118] J. Bonache, F. Martin, R.M. Sillero, F. Falcone, T. Lopetegi, M. Laso, J. Garcia-Garcia, I. Gil, M.F. Portillo, and M. Sorolla. Equivalent-circuit models for split-ring resonators and complementary split-ring resonators coupled to planar transmission lines. *Microwave Theory and Techniques, IEEE Transactions on*, 53(4):1451–1461, 2005.

[119] W. J. Padilla, A. J. Taylor, C. Highstrete, M. Lee, and R. D Averitt. Dynamical Electric and Magnetic Metamaterial Response at Terahertz Frequencies. *Phys. Rev. Lett.*, 96107401, 2006.

[120] Zhimin Xu and Edmund Y Lam. Image reconstruction using spectroscopic and hyperspectral information for compressive terahertz imaging. *Journal of the Optical Society of America. A*, 27(7):1638–46, 2010.

[121] D. Shrekenhamer, W. Chen, and W. J. Padilla. Liquid crystal tunable metamaterial perfect absorber. *Physical Review Letters*, 110:1–5, 2013.

[122] H. Tao, A. C. Strikwerda, K. Fan, W. J. Padilla, X. Zhang, and R. D. Averitt. Mems based structurally tunable metamaterials at terahertz frequencies. *Journal of Infrared, Millimeter, and Terahertz Waves*, 32(5):580–595, 2010.

[123] T. Driscoll, H. Kim, B. Chae, B. Kim, Y. Lee, N. M. Jokerst, S. Palit, D. R. Smith, M. Di Ventra, and D. N. Basov. Memory metamaterials. *Science*, 325(5947):1518–21, 2009.

[124] D. Chowdhury, R. Singh, J. F. OHara, H. Chen, A. J. Taylor, and A. K. Azad. Dynamically reconfigurable terahertz metamaterial through photo-doped semiconductor. *Applied Physics Letters*, 99(23):231101, 2011.

[125] Y. Urzhumov, J. S. Lee, T. Tyler, S. Dhar, V. Nguyen, N. M. Jokerst, P. Schmalenberg, and D. R. Smith. Electronically reconfigurable metal-on-silicon metamaterial. *Physical Review B*, 86(7):075112, 2012.

[126] H. Chen, J. F. O'Hara, A. K. Azad, A. J. Taylor, R. D. Averitt, D. B. Shrekenhamer, and W. J. Padilla. Experimental demonstration of frequency-agile terahertz metamaterials. *Nature Photonics*, 2(5):295–298, 2008.

[127] G. H. Cottet, P. Koumoutsakos, and M. L. Ould Salihi. Vortex methods with spatially varying cores. *Journal of Computational Physics*, 162:164, 2000.

[128] T. Y. Hou. Convergence of a variable blob vortex method for the euler and navier-stokes equations. *SIAM Journal on Numerical Analysis*, 27:1387, 1990.

Biography

John Desmond Hunt was born in Baltimore, Maryland, on February 27^{th}, 1986. He moved to Knoxville, Tennessee, when he was five years old. He attended The University of Tennessee, Knoxville where he obtained a bachelor's degree in *Engineering Physics* with a minor in *Materials Science and Engineering* in 2009. He often goes by the name 'Jack'.